Development of an Experimental Permanent-Magnet Motor Drive

Joachim Lindström

Technical Report No. 312L

Submitted to the School of Electrical and Computer Engineering
Chalmers University of Technology
in partial fulfilment for the degree of
Licentiate of Engineering

Department of Electric Power Engineering
Göteborg, Sweden
April, 1999

CHALMERS UNIVERSITY OF TECHNOLOGY
Department of Electric Power Engineering
SE-412 96 Göteborg
ISBN: 91-7197-803-8
Chalmers Bibliotek, Reproservice
Göteborg, 1999

Abstract

The report describes the development and preliminary investigation of an experimental drive system, of which the central component is a permanent-magnet synchronous motor optimized for a hybrid electric vehicle. The maximum output power of the motor is 50 kW in continuous operation and 100 kW in intermittent operation. The synthesis of the motor was based on numerical calculations of the motor properties and losses by means of a finite-element method. Simulations according to standardized driving-cycles were used to predict the energy consumption of the drive line. A thermal model was developed and implemented as a thermal network and the numerically calculated losses were applied for evaluation of the temperature distribution in the motor. Experimental results have shown discrepancies less than 5 K between the measured and the calculated temperature rises in the stator windings. Control of the drive was done with a control computer based on a digital signal processor. A simple comparison of two different control strategies indicates that the motor efficiency is affected by the chosen strategy. A calorimetric method was implemented to improve the accuracy of the loss measurements, since the traditional input-output method is useless for high-efficiency motors. The maximum relative error in the measurement of the total motor losses was estimated to be ± 2.3 % at the nominal operating point and less than ± 3.5 % at any operating point in the investigated region. The measured maximum efficiency of the motor was 95.5 %, obtained at the nominal operating point. The motor concept chosen for the vehicle application can be designed for high efficiency in a wide range of speeds and loads.

Keywords: electric drivetrain, permanent-magnet motor, permanent-magnet drive, efficiency, calorimetric measurement, thermal network, thermal model.

Preface

This thesis is the outcome of a project titled 'Electrical Motors for Hybrid Electric Vehicles.' It is one of several projects within the Electric and Hybrid Electric Vehicle programme initialized by the Swedish National Board for Industrial and Technical Development (NUTEK). The programme involves research on electric drives, system management and control, and battery technology. I would like to express my gratitude to NUTEK for financial support.

There are a number of persons who have contributed to the work presented in this report. Some of them are worth mentioning explicitly:

Professor Jorma Luomi, who initiated the project, accepted me as a student and revealed some interesting topics within the field of electric machinery. Thereby, I was given the opportunity to devote a lot of attention to a subject, not only of technical interest to me, but also of importance to the global environment, I hope. Thank you!

Mr. Johan Hellsing, who was my associate during the first three years of the project. Many thanks for the companionship and the memorable moments involving liquid nitrogen and an expensive piece of plastic. Thanks also for gluing all those magnets ;-).

Dr. Jan Svensson, for being the link between theory and practice, which was necessary to put the numerous pieces of equipment together in the laboratory. Even the tedious work with the control system and the development of the control software became a thrilling challenge thanks to his positive attitude, experienced skills and exceptionally stubborn mind. Great thanks!

Dr. Torbjörn Thiringer and Dr. Anders Grauers both deserve a portion of gratitude. They have shown remarkable endurance by patiently helping out with good advice and interesting discussions. I am most grateful!

Mr. Torbjörn Larsson assisted me in the laboratory during many long hours, waiting for thermal equilibrium. He also contributed to the progress with the calorimetric method. Warm thanks!

The development of the rotor position decoder interface for the control computer caused me a lot of trouble. Mr. Anders Carlsson, IEA, Lund Institute of Technol-

ogy helped me uncover some essential information about the DSP-link extension bus, which solved the problems. Many unsigned, 32-bit thanks!

Thanks also to Mr. Tommy Leijonberg, ELMO Motors, Flen, for the test object I so badly needed for tuning and debugging the control system.

Finally, I would like to thank the staff of the department for support, good companionship and human(e) behavior.

List of Papers

The following papers constitute part II of this thesis:

Paper A: J. Luomi, J. Lindström and J. Hellsing, "Design and Analysis of Electrical Motors for a Hybrid Electric Vehicle", in *IEEE/Stockholm Power Tech Conference Proceedings*, Stockholm, Sweden, vol. Electrical Machines and Drives, pp. 274-279, June 18-22, 1995.

Paper B: J. Lindström, J. Hellsing and J. Luomi, "Design of High-Efficiency Electrical Motors for a Hybrid Electric Vehicle", in *The 13:th International Electric Vehicle Symposium, EVS-13, Conference Proceedings*, Osaka, Japan, vol. II, pp. 64-69, October 13-16, 1996.

Paper C: J. Lindström, J. Luomi and J. Hellsing, "Permanent-Magnet Motor for a Hybrid Electric Vehicle", in *NORPIE/98 IEEE Nordic Workshop on Power and Industrial Electronics Proceedings*, Espoo, Finland, pp. 200-205, August 26-27, 1998.

Paper D: J. Lindström, "Thermal Model of a Permanent-Magnet Motor for a Hybrid Electric Vehicle", Report No. 11R, ISSN: 1401-6176, Department of Electric Power Engineering, Chalmers University of Technology, Göteborg, Sweden, April 1999.

Paper E: J. Lindström, "An Experimental Permanent-Magnet Motor Drive – System Description and Preliminary Measurements", Report No. 12R, ISSN: 1401-6176, Department of Electric Power Engineering, Chalmers University of Technology, Göteborg, Sweden, April 1999.

Contents

Part I

Introduction

Chapter 1

Introduction

Personal transportation is, and will be, an expanding field due to a growing population and increasing demands on availability and fast, convenient travel. At the same time, issues of environmental awareness and global energy consumption are in a state of continuous development. Subjects like green house gases, oil prospectation, fossile fuels, ozone layers and environment friendly alternatives will probably characterize political discussions and daily life for many years to come. In addition, considering that a large amount of the population does not yet have access to the highly technological society of the western world, solutions to environmental problems should develop and mature quickly if the rates of energy consumption and pollution are to be kept at reasonable levels. One important term arising from the energy consumption issue is energy efficiency. The impact of energy efficiency is great on numerous fields of technical interest, vehicle propulsion being one of them.

From a historical perspective, it is easy to realize that there is a problem with new environmental aspects impacting on different interests in an expanding technological society. It takes a lot of effort to inhibit or influence an ongoing process of great magnitude. The present infrastructure of the industrial world is well established, and the cost for changing any major part of it can be hard to justify, economically. Concerning personal transportation, there are today service establishments providing fuel, spare parts and whatever is necessary to keep the transports running, all being supplied by large industries [**?**].

Social structures involving habits and customs also make it difficult to release new concepts on the market, if they yield constraints in comparison with the old, well established systems. One aspect to account for, if new concepts for personal transportation are imposed on people's daily life, is that the combustion engine powered car is a vehicle that can provide both short and long-range transportation in a convenient way. Suggestions about using 'city-cars', adapted to the requirements for short-range traveling, have been given attention before, but without any real success.

In contrast to the ordinary combustion engine powered car, which people are used to, an electric vehicle (EV) is dependent on the possibility of recharging quickly at charging stations which today do not exist. Long-range capacity is not yet possible if the term 'long-range' refers to the capacity of an ordinary car. Most people are likely to perceive and refer to the differences as unwanted restrictions since the concept is unfamiliar, but it may only be the inertia of the mind that prevents a more positive response to the electric vehicle alternative from evolving. A key to liberate obstructed thinking is to uncover obscure facts by providing comprehensible information and education. There are many technical solutions under development, which make it possible, and indeed favorable, to further compel the issue of emission-free transportation.

In order to establish public confidence in an EV, one approach would be to combine the features of the combustion engine and the electrical motor. In inner city regions with high vehicle density or in other areas sensitive to pollution, it is possible to propel the car in a pure electric mode, yielding zero-emission operation. For long-range transportation on highways, the combustion engine would be used for on-board power generation. The concept of combining the two motor types establishes a new type of vehicle topology called hybrid electric vehicles (HEV), which can be implemented in, for instance, cars, buses, trucks and scooters. There are two major subsets of the HEV; the parallel hybrid system and the series hybrid system. Comparative investigations have been made [**?**] [**?**], which in itself is a subject for discussion and further scientific work. A series hybrid system was selected as the basis for the study in this project.

Electrical machines for vehicle propulsion is hardly a new idea [1]. However, the fast developing research in material science makes it possible to find new approaches to refining and developing electrical drive systems. Low-loss materials, low density composites with high mechanical strength and the rapid development of power semiconductors and computers are all very important for the future evolution of energy efficient drives.

In a vehicle application, important properties of the drive system are low weight, small volume and low production cost. Because of the battery's limited energy storage capacity, the efficiency of the electrical drive is an additional property that becomes utterly important if a competitive solution is to be created [**?**]. An electric drive in a vehicle application operates in a wide range of speeds and loads. In order to achieve high overall energy efficiency, it is essential to optimize the drive for the conditions encountered in a vehicle application [**?**].

[1] According to the book 'The Green Car Guide', the first known electric car was a small model built by Professor Stratingh in the Dutch town of Groningen in 1835. But the first practical electric road vehicle was probably made either by Thomas Davenport in the United States or by Robert Davidson in Edinburgh in 1842. (http://www.energy.ca.gov/afvs/ev/evhistory.html)

Chapter 2

The Project

The aim of the project was to investigate different types of electrical motors suitable for an HEV, and further develop one selected machine type. Improvement of energy efficiency in order to extend the operating range of the vehicle was considered to be important. Hence, the development of methods for analysis of the electric drive line in a vehicle application was necessary and was regarded as a part of the main objective. Construction of a full-scale experimental motor and validation with respect to the specified characteristics was also a primary goal.

Preliminary Study

An introductory part of the work was to identify the requirements which are important for an electric drive in an HEV application. Keywords for the study were weight, volume, power density, transmission complexity and overall efficiency. The purpose of the initial study and system analysis was to determine the required combination of motor specification and transmission most suitable for the HEV. The vehicle specification, used as a basis for the investigation, corresponds to an ordinary mid-sized car, except for the overall mass which is higher because of the battery (Paper A). As a result, it was decided to use a two-speed automatic transmission [**?**] and a motor designed for a constant power speed ratio (CPSR) of at least 2:1 (Paper A). At the time, the output power required was chosen to be 40 kW in continuous operation and 80 kW in intermittent operation. Later on, new information on the subject led to an upgrade of the required power to yield 50 kW in continuous operation and 100 kW in intermittent operation (Paper B).

Analysis

Development of methods for the analysis and design of the electrical motor as a part of the whole drive system was an important task. Computer-based tools for

simulations and computations were regarded as necessary for accurate prediction of the properties of a motor design.

To obtain a motor with low losses, relatively new materials have been chosen, which augments the difficulties in the calculations. Hence, the modeling and calculations of the iron losses were interesting challenges associated with a number of uncertainties. In the design procedure, measures were taken to reduce losses according to the theoretical models, but the additional losses arising from neglected phenomena and manufacturing processes were unknown.

A two-dimensional, time-stepping finite element method was used for the prediction of the motor properties and losses (Paper A). The end regions of the motor were, thus, not included in the numerical solution of the magnetic field. The prediction of the stator currents takes the end regions into account by using constant end-winding impedances in the circuit equations. The iron losses were calculated based on the Fourier analysis of the flux density variation [**?**] [**?**]. Furthermore, the terminal voltage of the motor was assumed to be sinusoidal, neglecting the influence of the voltage harmonics. The finite-element calculations were done by Johan Hellsing [**?**].

A dynamic model of the vehicle was used for simulations according to standardized driving-cycles. Calculations of the total energy consumed by the drive, given a specified distance traveled, is a measure of the energy efficiency. Improvement of the overall efficiency requires comparisons including the whole drive line and for this reason, loss models of the transmission and power electronics were included (Paper A). Regenerative breaking was not accounted for in the simulations, since it was not regarded as a limiting factor in the motor design work.

A thermal model was developed for the design and optimization procedure of the permanent-magnet motor. The model is a thermal network with lumped parameters represented by equivalent thermal resistances and equivalent thermal capacitances. Steady-state calculations and transient simulations with the thermal network were performed using a constant reference temperature. Special focus was put on the temperatures of the permanent magnets and the end windings (Paper D).

A Comparative Study

A comparison of a state-of-the-art induction motor (IM) design and a permanent-magnet synchronous motor (PMSM) design of the inset-magnet type was made. The IM design was specially made for low losses using thin laminations in the iron core and a copper cage winding in the rotor. Results have shown that both the IM and PMSM are good alternatives for the HEV. However, in terms of efficiency, improvements could be made by optimizing the PMSM (Paper A).

Motor Optimization

A univariant optimization procedure was applied to refine the inset magnet design chosen for further development. The constraints used in the procedure were:

- The ability to deliver required output torque
- The ability to withstand permanent demagnetization
- The maximum allowed temperature of the permanent magnets and the windings

Finite-element calculations were used to determine the output torque and the flux density in the permanent magnets at a three-phase short circuit. Steady-state calculations and transient simulations with the thermal model provided the additional information necessary to determine the feasibility of a motor design (Paper D).

The comparison of motor designs were based on driving-cycle simulations and an objective function including (Paper B) [**?**]:

- The cost of the active materials of the motor
- The cost of the power electronic converter
- The cost of weight
- The cost of energy losses
- The cost of extra batteries required for a specified distance traveled in pure-electric mode

An experimental motor was constructed according to the design which emanated from the optimization. The optimized motor design had a 10 % loss reduction and a 14 % weight reduction compared with the preliminary design [**?**].

Power Electronics and Control System

A compact power electronic converter suitable for a vehicle application was built for the PMSM. It is a water-cooled voltage source converter (VSC) equipped with integrated power modules based on IGBT-technology. A reduction of electromagnetic interference with the control system was achieved by using optical links for the signal transfer between the power circuit and the control system.

Control of the VSC was conducted with a single-board control computer developed by Anders Carlsson [**?**]; the IEA-MIMO, based on the Texas Instruments

TMS320C30 floating point digital signal processor. The control computer was equipped with a resolver decoding interface, an optical interface for the transfer of signals to the power circuit and additional signal conditioning devices to enable the assembly of a complete drive system (Paper E).

The Experimental Drive System

A laboratory set-up was built for experiments with the drive system. The PMSM was connected to a thyristor converter fed dc-machine, via a torque transducer and a reduction gear box. Power was supplied to the VSC by a grid-connected thyristor rectifier via a smoothing inductance and a dc-link capacitor bank (Paper C) (Paper E).

The set-up included equipment for measurements of the motor shaft torque, the electrical quantities of the motor, the motor temperature, the cooling water temperatures and the flow rate of the cooling water (Paper C) (Paper D) (Paper E) [**?**].

Methods for Loss Measurements

Motors with high efficiency, η, involve problems with measurements of the total losses. The use of the traditional input-output method is associated with inherent difficulties if a high accuracy is to be obtained. The maximum relative error of the total losses is $\frac{1}{1-\eta}$ times the errors of the measurements of the input and output power (Paper E). Therefore, high efficiency suggests that attention should be given to other possible methods.

By considering the test object to be a water cooled, high-efficiency motor with low rotor losses, the thermal aspects become interesting since most of the dissipated losses will be transferred to the cooling water. Studies of a calorimetric method were conducted and results have indicated that considerable improvement of the loss measurement accuracy could be made. Equipment for the implementation of the method was constructed and calibration with respect to actual conditions was carried out (Paper C) (Paper E) [**?**].

Motor Tests

The preliminary test results of the PMSM were based on three basic experiments:

Tests with open stator circuit provided information on the emf induced in the stator windings and, hence, the flux linkage due to the permanent magnets. Measurements of the shaft torque at different rotational speeds give

the sum of the friction losses and iron losses with zero current in the stator windings.

Tests in generator operation with resistive load were the first steps in the investigation of the machine characteristics under load conditions. Preliminary tests of the calorimetric method were also made for verification of the performance of the measurement system.

Tests in motor operation using two different control strategies were the final test sequences made. Approximately 50 tests in steady-state operation at various operation points were made. Each test involved around two hours of running in order to obtain thermal equilibrium. The operating region investigated comprised speeds up to 6000 rpm and load torque up to 80 Nm, which corresponds to the constant torque region.

The measurements have shown that the motor has a high efficiency: 95.5 % at the nominal operating point. An error analysis determined the lower efficiency limit to be 95.3 % and the upper to be 95.6 % (Paper E).

A preliminary analysis of the loss measurements has shown differences compared with the calculated losses, which indicate that the additional losses are relatively high. Subtraction of the winding losses and friction losses from the measured total losses, leaves a residual comprised of iron losses, eddy-current losses in the magnets and additional losses. The sum of loss components, calculated with the numerical method, was about half of the separated residual. The winding losses are also larger than expected, mainly due to the skin effect and proximity effects in the stator windings (Paper E). Measurements of the experimental motor have shown that the winding resistance increases by approximately 84 % at 200 Hz and 172 % at 400 Hz, compared with the dc-resistance [**?**].

Chapter 3

Summaries of the Included Papers

Paper A: Design and Analysis of Electrical Motors for a Hybrid Electric Vehicle

In this paper, the predicted performances of a high-efficiency cage induction motor and a permanent-magnet synchronous motor are compared with each other, based on the data and drive requirements of a hybrid electric vehicle.

The design of the permanent-magnet motor is of the inset-magnet type. A time-stepping finite-element method was used for the analysis of machine behavior and losses. As a result, loss charts of the machines were obtained for control strategies that minimize the losses. The energy efficiency of the machines was compared by using driving-cycle simulations.

A specially designed cage induction motor can reach a very high efficiency in a hybrid electric vehicle application. Results from the simulations have shown that the energy efficiency of the induction motor is 94.8 % which should be compared with 95.3 % for the non-optimized permanent-magnet motor. A conclusion is that further improvement of the efficiency can be achieved by using an optimized permanent-magnet synchronous motor.

Paper B:
Design of High-Efficiency Electrical Motors for a Hybrid Electric Vehicle

The paper deals with the design and optimization of a permanent-magnet synchronous motor for a hybrid electric vehicle. Finite element analysis and a thermal network have been used to evaluate the electromagnetic properties, losses and temperature distribution of the motor.

The losses of the motor, mechanical transmission and power electronics are presented as loss charts, and used in the simulation of the vehicle dynamics over standardized driving cycles. In this way, the total energy consumption of the drive line can be evaluated. The variation in the manufacturing costs, weight and losses of the drive line, as well as the variation in the battery cost and weight have been used to evaluate an objective function for the optimization of the motor.

The calculated results have shown that the motor design and properties were influenced by the definition of the objective function, which was expected. The predicted energy efficiency of the optimized inset-magnet motor increased from 95.7 % to 96.3 % during the optimization.

Paper C:
Permanent-Magnet Motor for a Hybrid Electric Vehicle

The paper deals with the constructed permanent-magnet synchronous machine of the inset-magnet type for a hybrid electric vehicle. The machine characteristics have been evaluated by finite element analysis and driving simulations. The optimization of the machine was based on an objective function including the energy losses, weights and production costs of the electric drivetrain, as well as the amount of batteries required in a pure-electric operation.

The experimental machine has high efficiency in a wide operating region. Preliminary tests of the machine operating as a generator against a resistive load indicate that there are discrepancies between the predicted and measured losses. The measurements of the machine losses were made with a calorimetric method.

Paper D:
Thermal Model of a Permanent-Magnet Motor for a Hybrid Electric Vehicle

The report describes a thermal model of a water cooled permanent-magnet motor intended for use in a hybrid electric vehicle. Studies of previously published work on thermal modeling of small induction motors were used as a basis for the model.

A lumped-parameter model of the motor was implemented as a thermal network, using a constant reference temperature both for steady-state calculations and transient simulations. Temperature measurements of a full-scale experimental motor showed good agreement with the calculated temperatures, using the measured losses applied to the thermal model. The relative error of the temperature rise was less than 12 %.

A sensitivity analysis of the model showed a maximum temperature deviation of ± 12 K, when the thermal resistances were changed from 200 % down to 50 % of the nominal value. Especially important components in the modeling are the thermal contact resistance between the stator yoke and frame and the heat transfer from coil sides to stator teeth.

Paper E:
An Experimental Permanent-Magnet Motor Drive – System Description and Preliminary Measurements

The report presents a drive system built for experimental use in a laboratory. An experimental permanent-magnet motor of the inset-magnet design, optimized for a hybrid electric vehicle was the test object. A power electronic converter suitable for the experimental motor was built and equipped with a digital control system .

Control methods suitable for the motor design were studied and implemented for the experimental drive. Results from the tests show that the motor performance depends on what control strategy is chosen. Below the base speed, the commonly used current minimization strategy works well and utilizes the motor capacity better than the quadrature axis current control.

The total losses of the PMSM were measured with a calorimetric method for improved accuracy. Accuracy estimations show that the total losses can be determined within ± 3.5 % of the measured value in the whole operating region investigated. At the nominal operating point, the error was less than ± 2.3 %.

The predicted torque characteristics agree well with the ones experienced in the laboratory. In addition, the induced emf corresponds well to the expected performance, which indicates that the calculated flux linkage agrees well with the real one. The maximum efficiency measured is 95.5 %. Analysis and estimation of the errors show that the true efficiency is between 95.3 % and 95.6 %.

Further investigation associated with the control aspects should be made in order to validate the experimental PMSM to its full extent. An investigation of the friction losses can simplify the loss separation and improve the analysis of measured results.

Chapter 4

Conclusion

This thesis describes the development of an electrical drive system based on a full-scale experimental motor. The drive was constructed for experimental investigation in a laboratory. The central component of the drive is a permanent-magnet synchronous motor, optimized for a hybrid electric vehicle application.

Methods for analysis and design of the electrical motor were developed based on finite-element calculations and driving-cycle simulations. A comparison of an induction motor and a non-optimized permanent-magnet synchronous motor has shown that both alternatives are suitable for the application. The permanent-magnet motor was chosen for further development and improvement of efficiency.

The experimental motor was constructed according to the results from a univariant optimization procedure. Water-cooling of the stator frame was chosen and a pre-tensed carbon-fiber composite sleeve was used for sufficient strength of the rotor construction.

A thermal model was developed and implemented as a thermal network. The numerically calculated losses of the motor design were applied for evaluation of the temperature distribution in the motor. A validation of the model using measured losses has shown discrepancies less than 5 K between the measured and the calculated temperature rises in the stator windings. A sensitivity analysis of the model has shown a maximum temperature deviation of ± 12 K, when the thermal resistances were changed from 200 % down to 50 % of the nominal value.

Various control methods suitable for the motor design were studied. Results from the tests show that there are deviations in the motor performance depending on the control strategy chosen. Below the base speed, the commonly used current minimization strategy works well, but at speeds in the vicinity of the base speed, the harmonic content of the armature current become high, due to an insufficient dc-link voltage. The chosen control strategy did not include the required flux control at high speeds, yielding current controller saturation and overmodulation. Hence, the maximum efficiency achieved may possibly be improved further by the

implementation of a refined control.

A calorimetric method was adopted to improve the accuracy of the loss measurements, since the traditional input-output method is useless for high-efficiency motors. Approximately 50 tests were conducted in steady-state operation at various operating points up to 6000 rpm and 80 Nm. An estimation of heat leakage was made by measuring the temperatures of the motor surface and the supporting mechanical structure. The estimated total leakage was less than 17 W at the worst case during the tests. The maximum relative error in the measurement of the total motor losses was estimated to be ± 2.3 % at the nominal operating point and less than ± 3.5 % at any operating point. The measured maximum efficiency of the motor is 95.5 %. Error estimations show that the limits of the efficiency are 95.6 % and 95.3 %.

A preliminary analysis of the obtained test results indicates that the additional losses are significant. The observed discrepancies between measured and predicted losses are related to the additional losses since the predicted loss components do not include three-dimensional effects or increased losses due to harmonics in the load current. Furthermore, the model used for the friction losses has not been verified, which introduces some uncertainties in the analysis of the measurements. A subtraction of the winding losses and friction losses from the measured total losses, leaves a residual comprised of iron losses, eddy-current losses in the magnets and additional losses. The sum of loss components, calculated with the numerical method, was about half of the separated residual. A suspicion is that the manufacturing process may influence the iron losses, perhaps due to little experience with thin laminations. Degradation of the current control at high speeds may also slightly contribute to an increase in losses due to a high harmonic content in the stator current.

Further investigations associated with the control aspects should be carried out in order to validate the experimental motor to its full extent. The performance in flux weakening operation is of special interest and should be brought to the fore. Experimental investigation of friction losses is required for accurate loss separation and to improve the analysis of measured results. Reduction of the skin effect and proximity effects in the stator windings can possibly be done by using litz-wire.

The motor concept chosen for the vehicle application can be designed for high efficiency in a wide rage of speeds and loads. Numerical computation of iron losses is time-consuming and associated with difficult issues concerning loss models. The fast development of computer capacity and the potential of combining rapid computation with accurate measurements indicate promising opportunities for future work.

Part II

Included Papers

Paper A:
Design and Analysis of Electrical Motors for a Hybrid Electric Vehicle

Published in the conference proceedings of IEEE/Stockholm Power Tech,
International Symposium on Electric Power Engineering
June 18 - 22, Stockholm, Sweden, 1995

Paper B:
Design of High-Efficiency Electrical Motors
for a Hybrid Electric Vehicle

Published in the conference proceedings of EVS-13,
The 13:th International Electric Vehicle Symposium
October 13 - 16, Osaka, Japan, 1996

Paper C:
Permanent-Magnet Motor for a Hybrid Electric Vehicle

Published in the conference proceedings of NORPIE/98,
IEEE Nordic Workshop on Power and Industrial Electronics
August 26 - 27, Helsinki, Finland, 1998

Paper D:
Thermal Model of a Permanent-Magnet Motor for a Hybrid Electric Vehicle

Report No. 11R, ISSN: 1401-6176
Published by the Department of Electric Power Engineering
Chalmers University of Technology, Göteborg, Sweden, 1999

Paper E:
An Experimental Permanent-Magnet Drive – System Configuration and Measurements

Report No. 12R, ISSN: 1401-6176
Published by the Department of Electric Power Engineering
Chalmers University of Technology, Göteborg, Sweden, 1999

Design and Analysis of Electrical Motors for a Hybrid Electric Vehicle

J. Luomi, J. Hellsing, J. Lindström
Department of Electrical Machines and Power Electronics
Chalmers University of Technology
S-412 96 Göteborg, Sweden

A. Arkkio
Laboratory of Electromechanics
Helsinki University of Technology
FIN-02150 Espoo, Finland

1995

Abstract

The predicted performances of a high-efficiency cage induction motor and a permanent-magnet synchronous motor are compared with each other, based on the data and drive requirements of a hybrid electric vehicle. The permanent-magnet motor is of the inset-magnet type. A time-stepping finite-element method is used for the analysis of machine behaviour and losses. As a result, loss charts of the machines are obtained for control strategies that minimize the losses. The energy efficiency of the machines is compared by using driving-cycle simulations. A specially designed cage induction motor can reach a very high efficiency in a hybrid electric vehicle application. A further improvement of the efficiency can be achieved by using a permanent-magnet synchronous motor.

1 Introduction

The development of electric and hybrid electric vehicles has gained increasing attention in recent years. In these vehicles, important requirements for the electric drive are low weight, small volume, high efficiency and low cost. The classical cage induction motor (IM) is an obvious alternative when choosing the motor for the vehicle drive, but a permanent-magnet synchronous motor (PMSM) can offer advantages in terms of higher efficiency and specific power [1] [2].

The maximum torque of a PMSM is limited by the stator current rating. The speed that can be attained by this torque is limited by the available supply voltage. This base speed, the maximum torque and the power factor thus determine the VA rating of the power electronics feeding the motor.

An electric vehicle is operated at an approximately constant power output in a wide speed range, and the constant-torque region covers only the lowest speeds. The base speed is usually about 25% of the total speed range. The constant-power operation of an electrical machine is achieved by weakening the flux of the machine. The operation of a PMSM above the base speed is possible by weakening the permanent-magnet excitation by a demagnetizing field component supplied by the stator winding [3] [4] [5].

An electric-vehicle drive operates in a wide speed range and frequently at partial load. Therefore, the drive should have a good efficiency also at low speeds and small loads. It is thus important to reduce the motor losses under light load conditions by using an appropriate control strategy [4].

In this paper, the predicted performances of a high-efficiency IM and a PMSM are compared with each other, based on the data and drive requirements of a hybrid electric vehicle. The PMSM is of the inset-magnet type. The finite element method is used for the analysis of machine behaviour, and special attention is given to the evaluation of the losses by time-domain computation. The effects of eddy currents, magnetic saturation, the motion of the rotor and the non-sinusoidal supply are taken into account. As a result, loss charts of the machines are obtained for control strategies that minimize the losses. The energy efficiency of the machines is compared using the results from driving-cycle simulations.

2 Specification of the drive

The vehicle data shown in Table 1 were used for the dimensioning and comparison of the motors. As the first step of this investigation, preliminary design of the mechanical transmission with one and two speeds was carried out, and the total volume, weight and cost of the two systems were compared. The two-speed design was regarded as a good compromise between the size of the electrical motor and the complexity of the transmission. The specification of the electrical motor is shown in Table 2 for the two-speed transmission alternative, and the corresponding torque-speed characteristics are illustrated in Fig. 1.

Table 1: Vehicle data assumed

Vehicle mass	1700 kg
Drag coefficient	0.30
Projected front area	2.1 m^2
Top speed	150 km/h
Acceleration time 0-100 km/h	12 s

Table 2: Motor specification

Maximum intermittent power	80 kW
Maximum continuous power	40 kW
Maximum speed	12000 rpm
Base speed	6000 rpm
Maximum torque	127 Nm

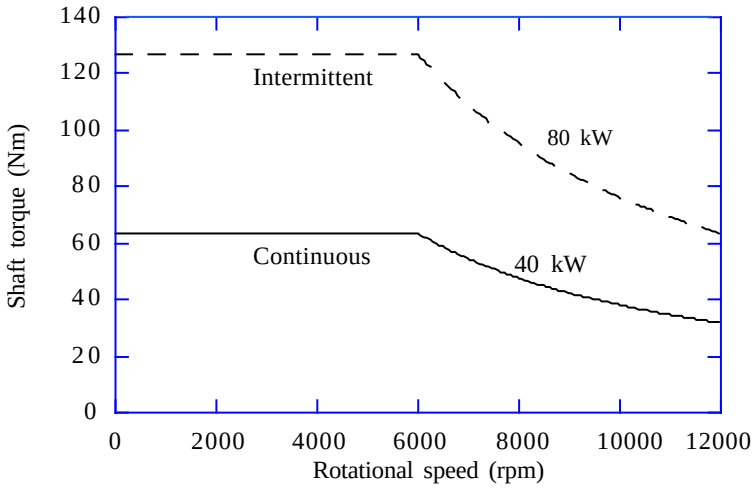

Figure 1: Torque-speed characteristics of the motor according to the specification

3 Time-stepping finite-element analysis

The calculation of the operational characteristics of the motors is based on the time-stepping finite-element analysis of the magnetic field and eddy currents [6]. The circuit equations of the windings are solved together with the field equations, and the rotor is rotated at each time step by changing the finite element mesh in the air gap.

The magnetic field is assumed to be two-dimensional, but the three-dimensional end-region fields are modelled approximately by constant end-winding impedances in the circuit equations of the windings. The non-sinusoidal voltage supplied by an inverter is imposed on the formulation through the circuit equations of the stator winding. The skin effect in the stator winding is neglected. The resistive losses of the windings and solid conducting parts, such as permanent magnets, are computed directly from the current densities solved in the finite-element analysis. It is assumed that the resistance between the permanent magnets is high and practically no induced currents flow from magnet to magnet.

The laminated iron is treated as a non-conducting, magnetically non-linear medium, and the non-linearity is modelled by a single-valued magnetization curve. The iron losses in the laminated parts are thus excluded from the model, but they are computed afterwards from the time-harmonic components of the flux-density distribution evaluated during the time-stepping process [7]. Finally, the iron losses are added to the electrical input power of the machine, and the friction and windage losses are subtracted from the mechanical output power.

The time-stepping method used consumes plenty of computer time. In order to model the motion of the rotor properly, the period of line frequency has to be divided into 200-800 time steps. For an inverter supply, the step size should be short enough to model the higher harmonic components in the supply voltage. In order to save computing time, the line-to-line voltage was assumed to consist of one square pulse per half-period, except for the lowest rotational speeds. This results in an overestimation of hysteresis and eddy-current losses as compared with a modern inverter with a high switching frequency.

4 Cage induction motor

An IM was designed for the drive in order to compare the PMSM with a reference machine. The goal of the design was to achieve low losses in converter-fed operation. The cross-section of the IM is shown in Fig. 2 and its main dimensions are given in Table 3.

For obtaining high efficiency, the iron core is made of low-loss steel sheet of 0.2 mm thickness and the cage winding is made of copper. The geometry is specially

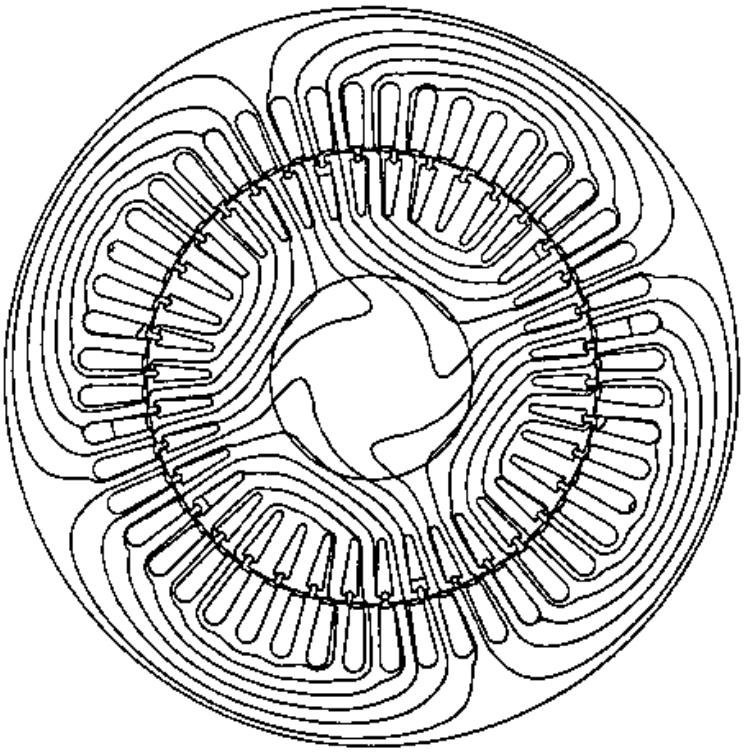

Figure 2: Cross-section of the IM

Table 3: Main dimensions of the induction motor

Number of pole pairs	2
Number of phases	3
Number of stator slots	48
Number of rotor slots	38
Outer diameter of the stator core	210.0 mm
Inner diameter of the stator core	130.0 mm
Core length	175.0 mm
Air gap	0.6 mm

adapted to the voltage wave form of a power-electronic converter, so that the harmonic losses are reduced.

The part-load efficiency of an IM can be maximized by controlling the stator voltage. If the friction losses and the influence of magnetic saturation are neglected, the efficiency, at a given frequency, is independent of output power when the slip is kept constant by reducing the voltage approximately as the square root of the load torque [8]. In order to take the influence of magnetic saturation and harmonics into account, the finite-element method was used to evaluate the losses at various loads and voltages. The results at the frequency of 200 Hz are shown in Fig. 3.

At light loads, the minimum losses are obtained at a constant slip of 0.75% , which is in accordance with the theory for linear machines. At high loads, the higher voltage causes saturation in the machine, and the minimum losses become larger than predicted by the linear model. The maximum voltage, of course, restricts the possibilities of loss reduction at the highest loads.

The optimal voltage-control strategy for the induction machine fed by an inverter was obtained by minimizing the losses at a large number of frequencies and loads. In this way, the constant-efficiency curves shown in Fig. 4 were obtained.

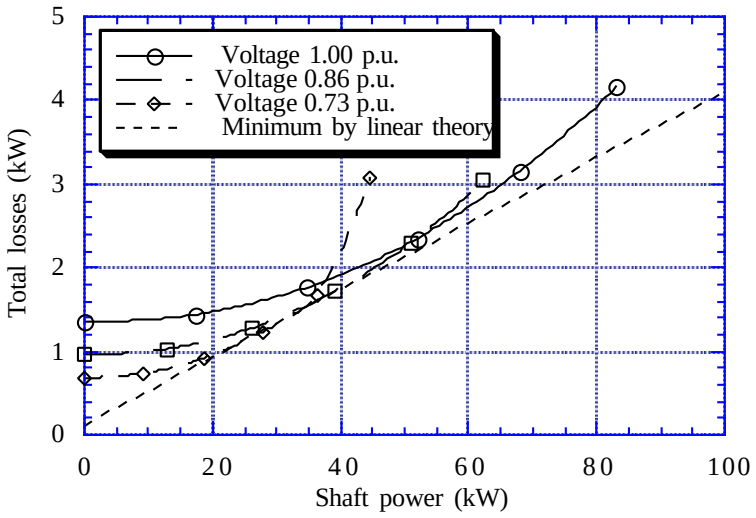

Figure 3: Predicted total losses of the IM at 200 Hz (about 6000 rpm)

5 Permanent-magnet synchronous motor

Neodymium-iron-boron magnets make it possible to achieve a high fundamental air-gap flux density by placing the magnets on the rotor surface. Flux-weakening operation above the base speed is realized by adding a demagnetizing component to the stator current, i.e. by advancing the current excitation angle. However, a

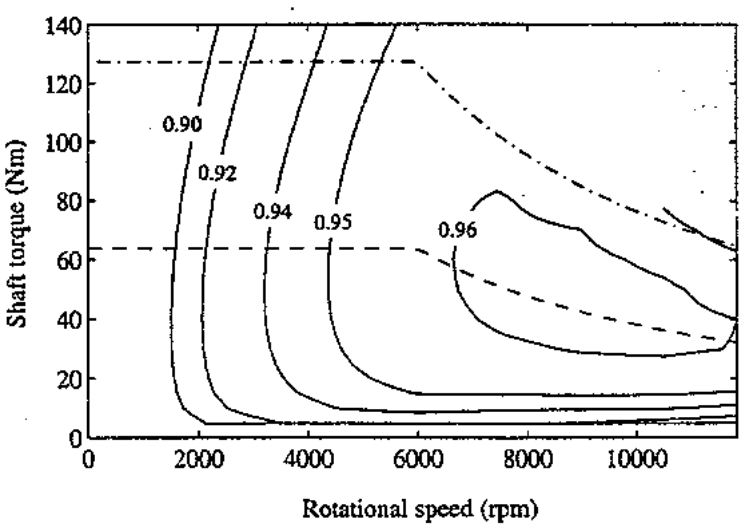

Figure 4: Predicted constant-efficiency curves of the IM

large direct-axis inductance Ld is required for efficient flux-weakening operation. The flux-weakening characteristics of a surface-magnet machine can be improved by using the inset-magnet design [3]. The magnets are placed in slots on the rotor surface so that the outer surface of the rotor is cylindrical as shown in Fig. 5. The quadrature-axis inductance L_q is

increased, and $L_q > L_d$. The open-circuit voltage E_0 and the saliency ratio $\xi = \frac{L_q}{L_d}$ define the flux-weakening characteristics of the machine. An infinite constant-power speed range can be achieved at all saliency ratios if the open-circuit voltage is properly chosen [5]. However, the maximum low-speed torque of the motor decreases with increasing flux-weakening speed range [4].

The properties of the permanent magnet material used for the calculations are given in Table 4. For comparison purposes, the stator of the IM was also used in the analysis of the PMSM, and the rotor core was assumed to be made of the same steel sheet. After this restriction, only three variables are to be chosen: the air gap, the magnet thickness and the covering angle of the magnets. The circumferential space between the magnets and the protruding iron parts should be about twice the air gap in order to avoid additional flux leakage [8].

An air gap of about 1 mm is required if a binding is used to hold the rotor magnets for high-speed operation. On the other hand, the air gap should be minimized in order to obtain good flux-weakening properties. Preliminary calculations showed, however, that the stator slot harmonics caused high eddy-current losses in the magnets. Therefore, the air gap was slightly increased from the minimum value. A lower limit for the magnet thickness is set by the fact that the magnets must withstand the maximum current in the negative direct-axis direction or a short-circuit current without any irreversible loss of permanent magnetization [9]. The

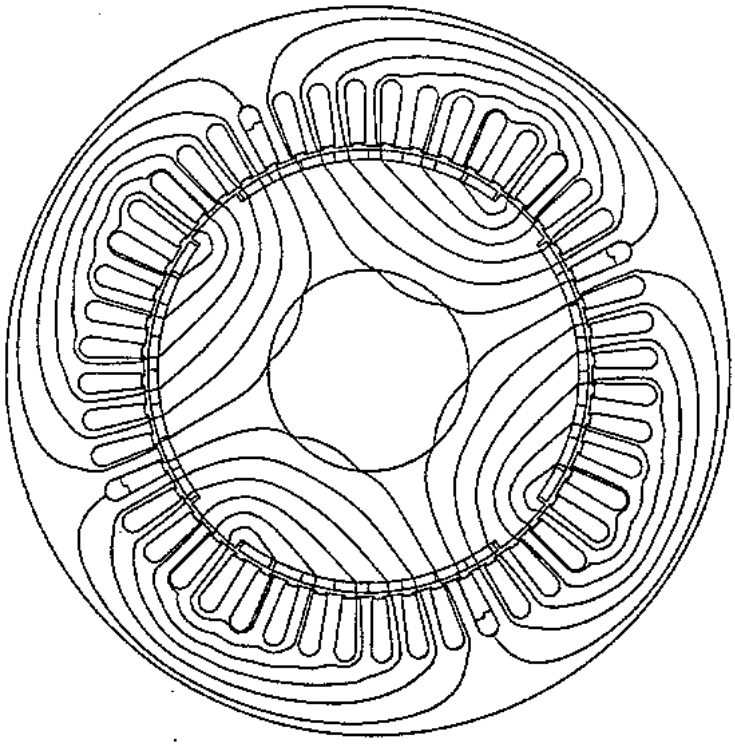

Figure 5: Cross-section of the PMSM (inset-magnet design)

Table 4: Properties of the permanent-magnet material

Remanence	1.07 T
Coercivity	812 kA/m
Resistivity	1.40 $\mu\Omega$m

Table 5: Main dimensions of the permanent-magnet rotor

Number of permanent magnets	32
Height of permanent magnets	2.8 mm
Width of permanent magnets	9.5 mm
Air gap	1.2 mm

covering angle of the magnets influences the magnetic flux and torque produced by the permanent magnets as well as the reluctance torque of the machine.

The dimensions of the permanent magnet rotor are given in Table 5. Based on the finite-element analysis, the inductances and open-circuit voltage were calculated corresponding to the base speed and maximum intermittent power. The per-unit values are shown in Table 4. These values correspond well to the theoretical values for obtaining an optimal flux-weakening range of 2:1 [5].

The optimal voltage-control strategy for the PMSM fed by an inverter was obtained by varying the voltage and load angle and minimizing the predicted losses at various frequencies and loads. The results at the frequency of 200 Hz are shown in Fig. 7, and the predicted constant-efficiency curves are shown in Fig. 7.

6 Driving-cycle simulations

In order to compare the performance of the motors, the energy consumption during a driving cycle of the hybrid electric vehicle was evaluated. The driving cycle consists of a combination of two urban driving cycles and a highway driving cycle as illustrated in Fig. 6. In a driving cycle, the vehicle speed is prescribed as a

Table 6: Parameters of the PMSM

Direct-axis inductance	Ld = 0.70 p.u.
Quadrature-axis inductance	L_q = 1.05 p.u.
Saliency ratio	$\xi = \frac{L_q}{L_d} = 1.51$
Open-circuit voltage	E_0 = 0.86 p.u.

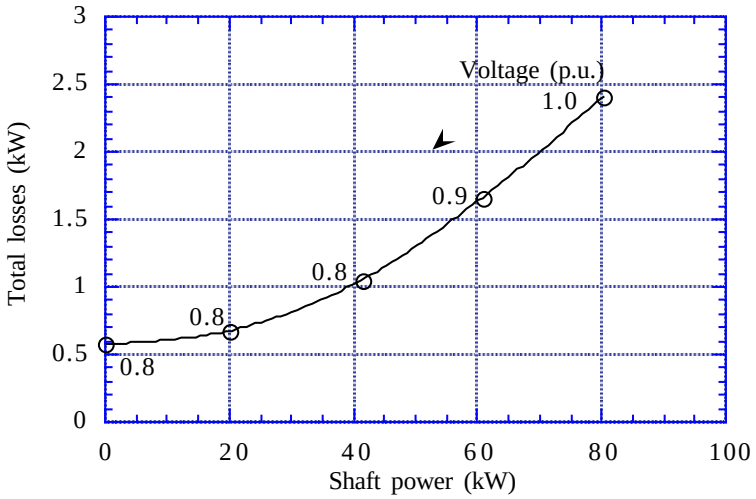

Figure 6: Predicted total losses of the PMSMat 200 Hz (6000 rpm)

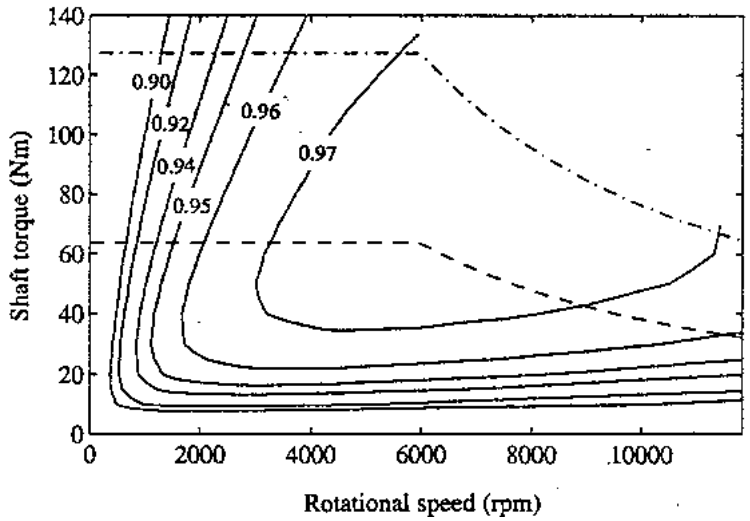

Figure 7: Predicted constant-efficiency curves of the PMSM

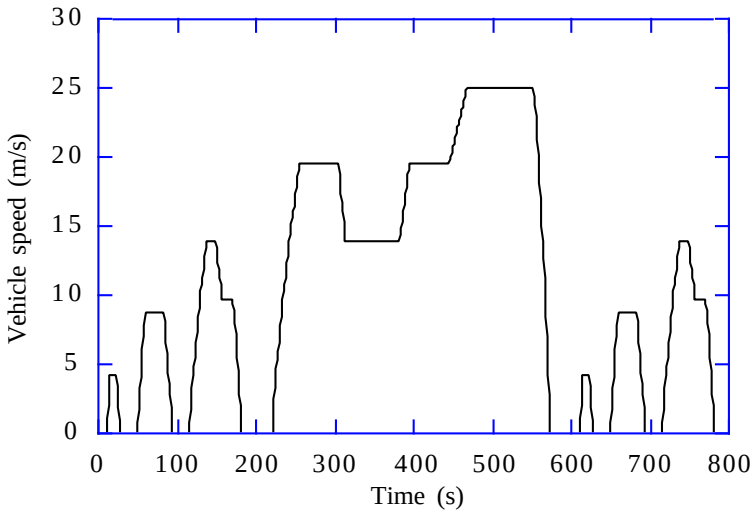

Figure 8: Driving cycle used for efficiency comparison

Table 7: Overall efficiencies over the driving cycle

IM	0.948
PMSM	0.953
IM and transmission	0.788
PMSM and transmission	0.813

function of time, and the vehicle acceleration can be found by means of numerical differentiation. The simulation was carried out by solving the equations of vehicle dynamics numerically. The power losses in the transmission were predicted and presented as torque transfer functions between the motor shaft and the wheels. The losses of the electric motors were given as loss charts for the machines in the speed-torque plane, corresponding to the efficiencies in Figs 4 and 7. During the simulation, the most efficient of the two speed ratios was chosen, taking only the losses in the motor into account. Regenerative braking and inverter losses were excluded from the model at this stage of the study. The results of the simulations are shown in Fig. 6 and Table 7. The PMSM has a higher overall efficiency than the high-efficiency IM, but the difference is not big. The losses of the PMSM are higher at light loads that occur at some of the constant speeds in Fig. 6. The difference in the efficiency including the transmission is larger, due to the fact that the PMSM is more likely to operate at low speeds where the efficiency of the transmission is higher.

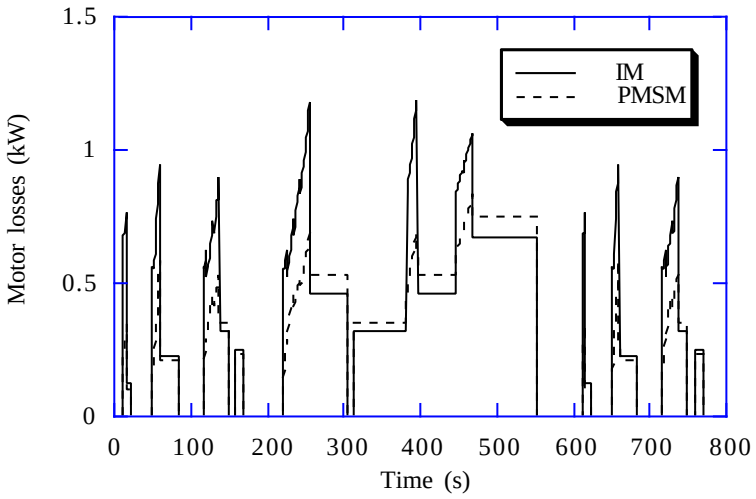

Figure 9: Motor losses from the driving-cycle simulations

7 Reduction of the eddy-current losses in the permanent magnets

The efficiency of the PMSM is high in large parts of the operating region compared with the high-efficiency IM, particularly at low speeds. The losses of the PMSM are higher at high speeds in light-load operation. This is to a great extent due to the resistive losses caused by the flux-weakening current component in the stator winding. Furthermore, the eddy-current losses in the permanent magnets increase with rotor speed. The eddy-current losses are mainly caused by the slot harmonics of the stator.

In order to reduce the eddy-current losses in the permanent magnets, two improvements were considered. Firstly, the slot-openings of the stator slots were decreased from the original value of 2.8 mm to 2.0 mm (Modified design 1). Secondly, the resistivity of the permanent magnets was increased by a factor of 1.6 in addition to the reduction of the slot openings (Modified design 2). The latter change corresponds to a subdivision of the permanent magnets in the axial direction so that the end effects in each permanent magnet decrease the eddy currents. The comparison of the losses of the three designs is shown in Fig. 7 at the frequency of 400 Hz.

A considerable reduction of the total losses is achieved, mainly due to lower losses in the permanent magnets. The losses of the Modified design 2 would not exceed the losses of the IM like those of the original design during certain intervals in Fig. 6, and the overall efficiency over the driving cycle would be increased.

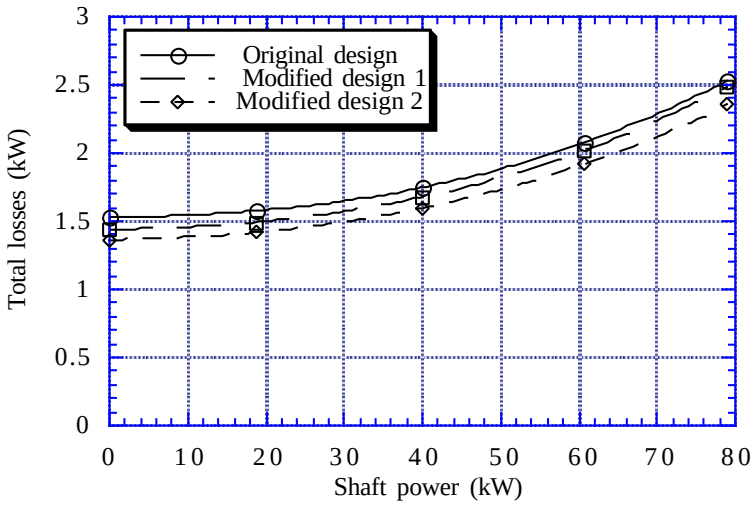

Figure 10: Predicted total losses of the PMSM at 400 Hz (12000 rpm)

8 Conclusions

Time-stepping finite-element analysis and driving-cycle simulation give detailed information of the behaviour and losses of the electrical motor in a drive system. A carefully designed cage induction motor can reach a very high efficiency in a hybrid electric vehicle application, but it will be more expensive than a standard motor. A further improvement of the efficiency can be achieved by using a permanent-magnet synchronous motor. In the constant-power range of 2:1, an inset-magnet motor can be designed for good field-weakening characteristics.

9 Acknowledgements

The authors are grateful to Dr Anders Hedman for his contributions to the preliminary design and modelling of the mechanical transmission. The financial support of Swedish National Board for Industrial and Technical Development (NUTEK) is gratefully acknowledged.

References

[1] G. Henneberger, G. Bailly, and J.R. Hadji-Minaglou, "Design and comparison of different motor types for electric vehicle application," in *EVS-11 Symposium Proceedings*, Florence, Italy, September 27-30 1992, vol. 1.

[2] D.F. Gosden, "Wide speed range operation of an ac pm ev drive," in *EVS-11 Symposium Proceedings*, Florence, Italy, September 27-30 1992, vol. 1.

[3] T. Sebastian and G.R. Slemon, "Operating limits of inverter-driven permanent magnet motor drives," *IEEE Transactions on Industry Applications*, vol. 23, no. 2, pp. 327–333, March 1987.

[4] R.F. Schiferl and T.A. Lipo, "Power capability of salient pole permanent magnet synchronous motors in variable speed drive applications," *IEEE Transactions on Industry Applications*, vol. IA-26, no. 1, pp. 115–123, January 1990.

[5] W.L. Soong and T.J.E. Miller, "Field-weakening performance of brushless synchronous ac motor drives," *IEE Proc.-Electr.Power Appl.*, vol. 141, no. 6, pp. 331–340, November 1994.

[6] A. Arkkio, "Finite element analysis of cage induction motors fed by static frequency converters," *IEEE Transactions on Magnetics*, vol. 26, no. 2, pp. 551–554, March 1990.

[7] A. Arkkio and A. Niemenmaa, "Estimation of losses in cage induction motors using finite element techniques," in *Proceedings of the International Conference on Electrical Machines*, Manchester, U.K, September 15-17 1992, vol. 2, pp. 317–321.

[8] Z.Q. Zhu, D. Howe, and Z.P. Xia, "Prediction of open-circuit airgap field distribution in brushless machines having an inset permanent magnet rotor prediction of open-circuit airgap field distribution in brushless machines having an inset permanent magnet rotor topology," *IEEE Transactions on Magnetics*, vol. 30, no. 1, pp. 98–107, January 1994.

[9] G.R. Slemon and X. Liu, "Modeling and design optimization of permanent magnet motors," *Electric Machines and Power Systems*, vol. 20, no. 2, pp. 71–92, March 1992.

Design of high-efficiency electrical motors for a hybrid electric vehicle

J. Lindström, J. Hellsing, J. Luomi
Department of Electric Power Engineering
Chalmers University of Technology
S-412 96 Göteborg, Sweden

1996

Abstract

The paper deals with the design and optimization of a permanent-magnet synchronous motor for a hybrid electric vehicle. Finite element analysis and a thermal network are used to evaluate the electromagnetic properties, losses and temperature distribution of the motor. The losses of the motor, mechanical transmission and power electronics are presented as loss charts, and used in the simulation of the vehicle dynamics over standardized driving cycles. In this way, the total energy consumption of the drive line can be evaluated. The variation in the manufacturing costs, weight and losses of the drive line as well as the variation in the battery cost and weight are used to evaluate an objective function for the optimization of the motor. The calculated results show that the motor design and properties are influenced by the definition of the objective function. The predicted energy efficiency of the optimized inset-magnet motor is over 96%.

1 Introduction

Low weight, small volume, high efficiency and low cost are required of the electric drive of a hybrid electric vehicle (HEV). In such drives, a permanent-magnet synchronous motor (PMSM) can offer advantages in terms of high efficiency and specific power [1] [2] [3].

An HEV is operated at an approximately constant maximum power output in a wide speed range, and the constant-torque region covers only the lowest speeds. The constant-power operation of a PMSM is achieved by weakening the flux of the machine by a demagnetizing field component supplied by the stator winding [4] [5] [6]. The load of the machine varies greatly. Therefore, the efficiency of the whole drive system should be high in a wide range of speeds and loads for obtaining a wide driving range in the electric vehicle mode.

Table 1: Vehicle properties

Mass	1700 kg
Wheelbase	2.66 m
Centre of gravity height	0.6 m
Projected front area	2.1 m^2
Drag coefficient	0.30
Rolling resistance coefficient	0.013
Top speed	150 km/h
Acceleration time 0100 km/h	10.5 s
Minimum gradeability	12%

An earlier investigation [3] showed that the losses at light loads are important for the overall efficiency of the drive system. A specially designed cage induction motor can reach a very high efficiency in an HEV application, but a further improvement of the efficiency can be achieved by using a PMSM. The most undesired features of the PMSM are the losses at light loads and in the field-weakening range.

This paper deals with the design and optimization of a PMSM for a series hybrid electric vehicle. The cost optimization is based on the manufacturing costs and weight of the PMSM, manufacturing costs of the power electronics as well as on the total energy losses in the PMSM, power electronics and mechanical transmission. The calculation of the total losses in the drive train is based on the energy consumed during standardized driving cycles for the vehicle.

2 Drive Line and its Components

2.1 Vehicle specification

The specification of the HEV considered in this work is summarized in Table 1. The performance of the vehicle is required to correspond to a regular modern car powered by a combustion engine. The series hybrid system consists of a complex energy source (battery and auxiliary power unit), converter, electrical motor and transmission, as illustrated in Figure 1

2.2 Transmission

Preliminary design of two alternative mechanical transmissions (with one speed and two speeds) was carried out [7], and the total volume, weight and cost of the two systems were compared. The two-speed design was regardedas a good

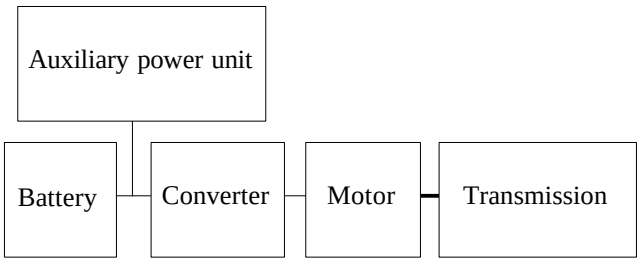

Figure 1: Series hybrid system

compromise between the size of the electrical motor and the size and complexity of the transmission.

2.3 Motor

The required torque-speed characteristics of the motor are shown in Figure 2 The constant-power region extends the rotational speed to twice the base speed, which was chosen to be 6000 rpm. The required continuous maximum power is about 50 kW,and maximum intermittent power is about 100 kW (3 minutes value).

The chosen electrical motor type is a four-pole PMSM with neodymium-iron-boron magnets inset in the rotor surface. The inset-magnet design has better field-weakening and torque characteristics than for example the surface-magnet design. The geometry of the motor is illustrated in Figure 3

It is assumed that the remanenceof the permanent magnets is1.07 T, corresponding to a powerful NdFeB magnet material at 100°C temperature. In order to avoid permanent demagnetization,the minimum flux density has to be restricted; it is assumed here that the permanent magnets allow a minimum flux density of 0.6 T.

For obtaining high efficiency, the iron core is made of low-loss steel sheet of 0.2 mm thickness. Furthermore, the losses are evaluated correponding to a voltage-control strategy that minimizes the total losses of the motor at each operating point.

2.4 Converter

The DC/AC converter feeding the motor is a water-cooled three-phase inverter with IGBT valves. The maximum output (rms) voltage of the converter is assumed to be 220 V. The maximum current is determined by the electrical motor. The maximum torque of a PMSM is limited by the stator current rating, and the speed that can be attained by this torque is limited by the available supply voltage. The base speed, the maximum torque and the power factor thus determine the VA rating of the power electronics.

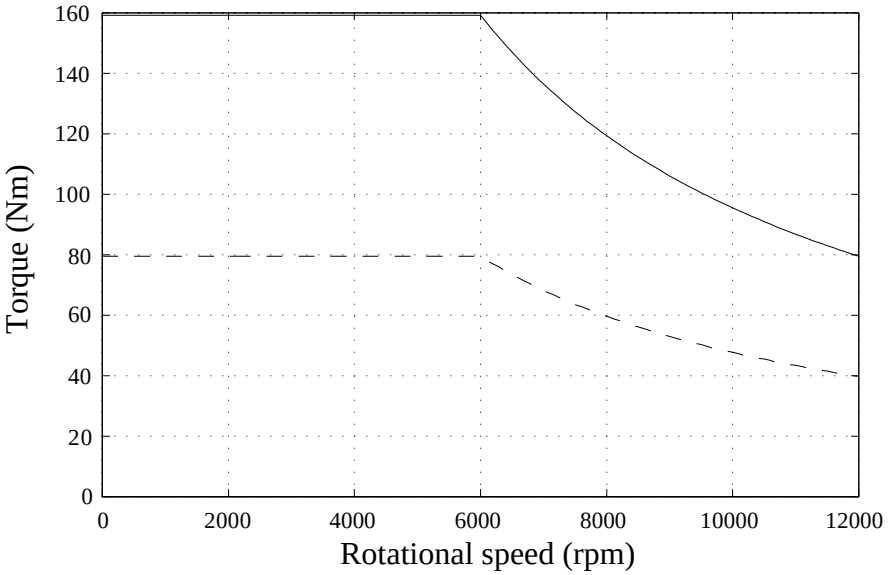

Figure 2: Operating region of the motor. The dashed curve shows the maximum intermittent torque (3 minutes)

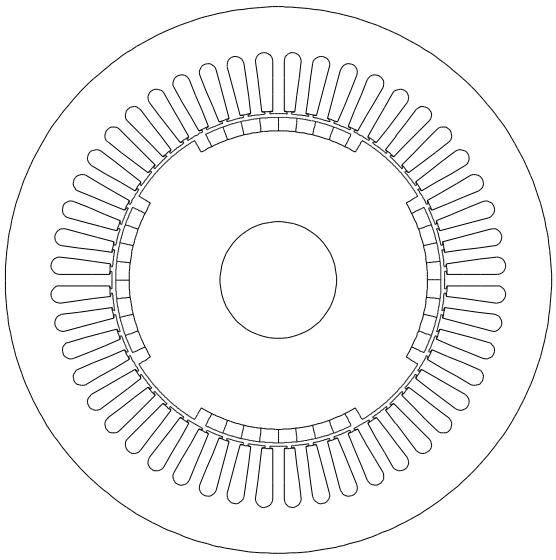

Figure 3: Cross-sectional geometry of the inset-magnet PMSM

3 Method of Synthesis

Figure 4 illustrates the methods used for the design calculations of the PMSM. The electromagnetic properties and losses of the motor were computed by using the finite element method (FEM). In addition, the losses were modelled based on the results from the finite element analysis. After the loss calculation, the temperatures of the machine were analysed by using a thermal network. In this way, the performance of the design was analysed, and its feasibility was checked. In addition, the losses of the converter and the mechanical transmission were modelled.

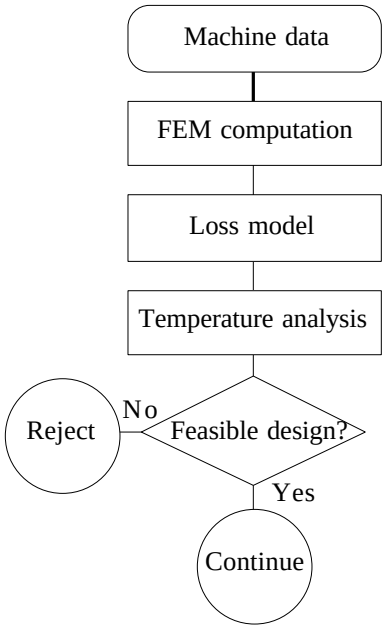

Figure 4: Flow chart of the synthesis

3.1 FEM computation

The steady-state operation of the PMSM was evaluated by two-dimensional finite element solution of the magnetostatic field. The method is based on the simultaneous solution of the finite element equations and the stationary voltage equations of the machine. The characteristics of PMSMs such as reactances, average torque and minimum flux density in the permanent magnets can be efficiently solved by such a method.

More detailed evaluation of the electromagnetic operational characteristics of the PMSM was based on two-dimensional, time-stepping finite element analysis [3]. Eddy currents, magnetic saturation, iron losses, the rotation of the rotor and non-sinusoidal voltages are included in the method of solution.

3.2 Motor losses

The time-stepping finite element analysis consumes plenty of computer time, and it should thus be used to analyse only a few working points. Analytical models were used to interpolate different power loss components between the computed points. In this way, a loss chart can be obtained for the whole operating region based on six time-stepping computer runs.

3.3 Temperature analysis

The temperature analysis was used to check the feasibility of the PMSM design. The temperature distribution in the machine was modelled by a thermal network both in steady and transient state. A constant temperature of 60°C was assumed for the cooling medium. Special attention was given to the temperature of the permanent magnets as the minimum allowed flux density in the magnets increases with the temperature.

3.4 Converter losses

The converter losses were predicted according to analytical expressions presented by Rockot. The losses were calculated based on information on the motor current, power factor, DC voltage, switching frequency and transistor parameters. The turn-on losses, turn-off losses and on-state conduction losses of the transistors as well as the conducting losses in the free-wheel diodes were included in the model.

3.5 Transmission losses

A model for the power losses in the transmission was developed by Hedman [7]. The losses depend on the wheel torque, vehicle speed and gear ratio; they were presented as torque transfer functions between the motor shaft and the wheels.

4 Driving-cycle Simulation

The energy consumption of an HEV depends on the vehicle properties, the topography of the area where the vehicle is propelled and the speed demand as a function of time. The latter is known as a driving cycle.

In order to compare the motors, the performance and energy consumption of the drive train was evaluated during a driving cycle by solving the dynamic equations of the vehicle. The losses of the motor, transmission and converter were presented as loss charts in the whole operating region, and the Matlab/Simulink program was used for the solution. Figure 5 illustrates the data needed for the simulation.

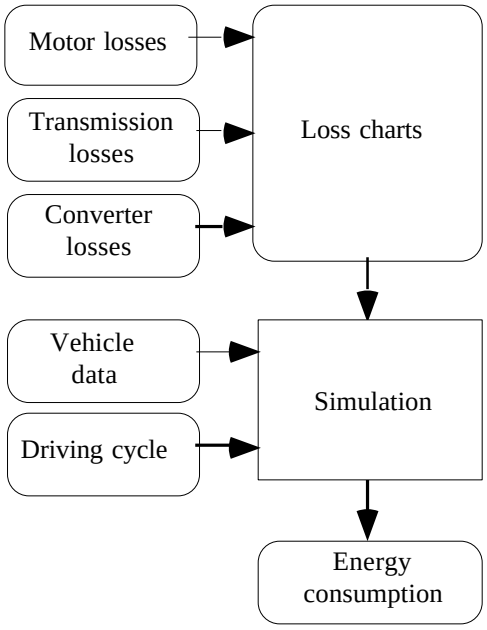

Figure 5: Flow chart of simulation

As the result of the simulation, the total energy consumption of the vehicle as well as the loss energies of the components of the drive train were obtained. Recuperative braking was not included in the simulations, and variations in altitude were neglected.

The driving cycle used in the simulations consists of one HFEDS and one UDDS driving cycle [8]. These driving cycles are shown in Figures 6 and 7. The results of the driving cycle simulation depend on the strategy for shifting gear of the two-speed gearbox. It was chosen to use the gear which results in the best overall efficiency of the drive train. This may not result in a realistic sequence of shifting, but is a simple way to obtain an adequate comparison between different designs. An example of the resulting working points of the PMSM is shown in Figure 8.

5 Optimization

For optimizing the electrical machine for an HEV, several features are to be considered. The design has to be feasible, i.e. the requirements of maximum torque, maximum temperature and minimum flux density in permanent magnets have to be satisfied. The optimization problem is to find a design which minimizes an objective function. The price, the weight and the cost of losses of the electrical machine should be included in the objective function. In addition, the influence of the electrical machine on the prices, weights and losses of other vehicle parts should be considered.

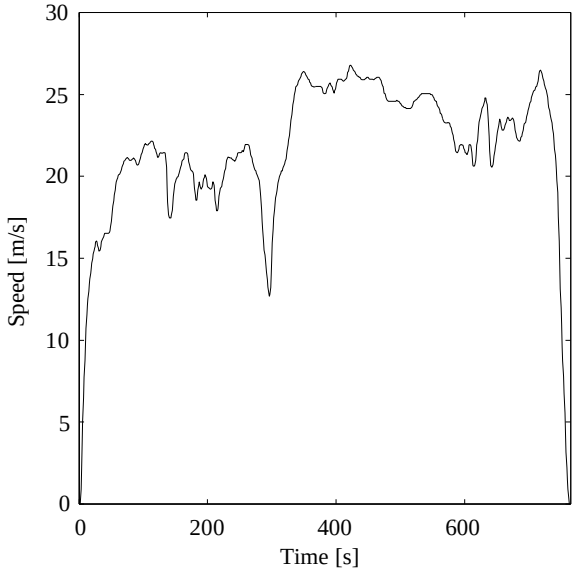

Figure 6: Driving cycle HFEDS

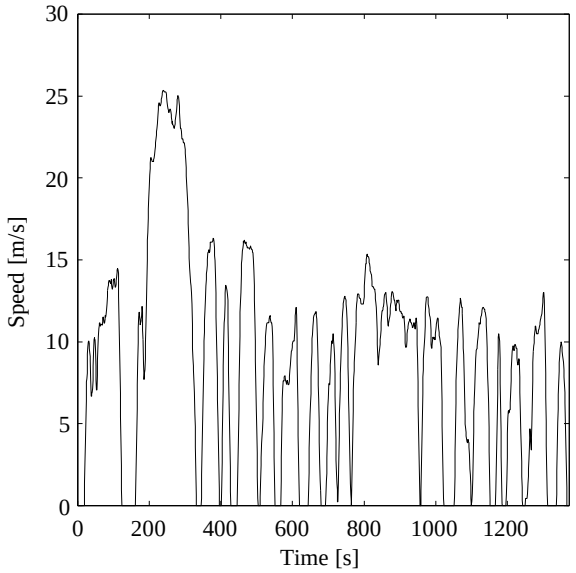

Figure 7: Driving cycle UDDS

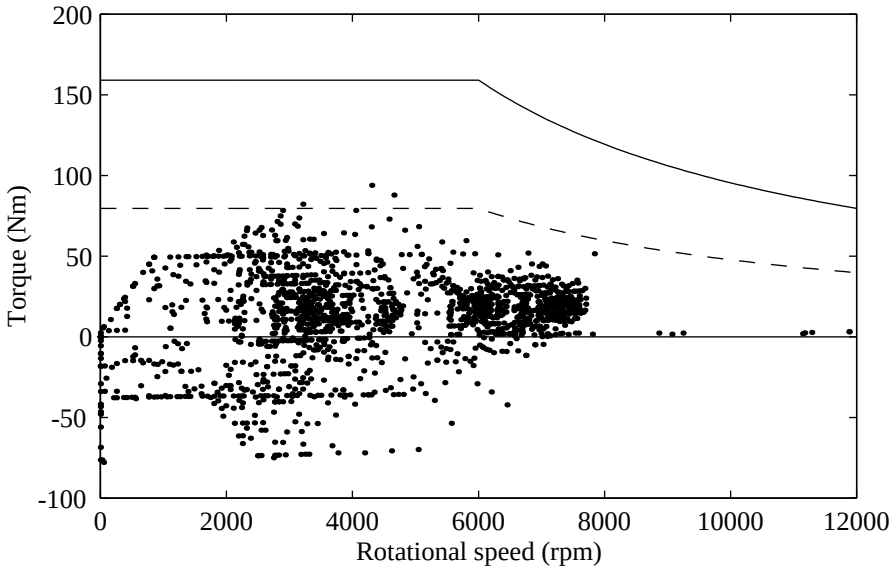

Figure 8: One-second samples of the combined driving cycle

In the following, the objective function chosen for designing the inset-magnet PMSM is defined. Naturally, the exact definition of such an objective function may be discussed. It is, however, important to realize that the losses and also the properties of the whole drive train have an influence on the design of the electrical machine.

5.1 Objective function

The objective function is defined as

$$C = C_m + C_c + c_m m_m + c_d W_d + c_b W_d \tag{1}$$

where

- C_m is the cost of active materials of the motor
- C_c is the cost of converter
- c_m is the cost of weight per kg
- m_m is the weight of the motor
- c_d is the cost of energy losses per kWh
- W_d is the energy losses

- c_b is the cost of extra batteries per kWh energy losses

It was assumed that the car is driven 15 000 km/year. The total driving time was assumed to be 5000 h during the life time of the car, corresponding to 8427 driving cycles. The auxiliary power unit was considered only as a constant part of the total vehicle mass. Considering the mechanical transmission, only the energy losses were taken into account, i.e. the price and weight were assumed to be constants. Also the weight of the converter was assumed constant.

5.2 Material cost

The varying part of the manufacturing costs of the electrical machine can be roughly estimated by the costs of the materials for the active part of the machine, if these costs are adjusted in order to take labour and machine costs into account. The material costs used in the optimization are given in Table 2.

Table 2: Material costs

Laminated iron	5 ECU/kg
Solid iron	5 ECU/kg
Copper	6 ECU/kg
NdFeB magnets	100 ECU/kg

5.3 Converter cost

The converter was assumed to have a maximum output voltage of 220 V. The cost of the converter was assumed to vary with the maximum current Imax of the motor according to

$$C_c = k_1 + k_2 I_{max} \tag{2}$$

where $k_1 = 353$ ECU and $k_2 = 3.53$ ECU/A.

5.4 Cost of weight

Carrying extra weight increases both energy consumption and the cost of the mechanical construction of the vehicle. The cost of extra mass of the motor was set to $c_m = 23.5$ ECU/kg.

5.5 Cost of losses

Energy is lost in the drive line only when the vehicle is in operation. However, charging will also introduce losses, which have to be accounted for. Assuming the energy price of 0.141 ECU/kWh, charger efficiency of 90% and battery efficiency of 80% yields the cost of energy losses of $c_d = 0.196$ ECU/kWh.

5.6 Cost of extra batteries

It was required that the capacity of the batteries corresponds to 96 km driving in the electric-vehicle mode10. If the overall efficiency would be 100% , the vehicle propulsion would consume a specific amount of energy during a specified driving cycle. An energy consumption exceeding this ideal value implies that additional batteries have to be carried, increasing both the cost of batteries and the weight cost. An energy density of 80 Wh/kg and a battery cost of 118 ECU/kWh yields the cost of extra batteries of $c_b = 0.208$ ECU/kWh.

5.7 Primary variables

The PMSM design is essentially determined by the following eight primary variables:

- inner diameter of stator core
- core length of the machine
- air gap
- magnet thickness
- current density of stator winding
- flux density of stator teeth
- flux density of stator yoke
- open-circuit voltage

Also a few other quantities have some influence on the design, but they can be chosen before the optimization process or adjusted after the end of the process.

The optimization of the machine means to determine a feasible design that corresponds to the smallest possible value of the objective function defined by Equation (1). The approach chosen for the optimization corresponds to the method presented by Nurdin et al.. The essential point of this approach is the synthesis, i.e. the creation of feasible designs prior to optimization. The optimization was carried out by using a simple search method.

6 Results

The initial design for the optimization was based on an earlier investigation [3]. Some of the dimensions and properties of this machine, called Design A, are presented in Table 3 The optimization was carried out using the method outlined above. The resulting Design B is also presented in Table 3. The constant-efficiency curves of Design B are shown in Figure 9.

The air gap of the machine was not varied during the optimization, but set to 1.2 mm. This value is large enough to restrict the eddy-current losses in the magnets to a low value. The motor is to be operated up to twice its base speed by flux weakening. The strongest demagnetization occurs at the highest stator current, which is obtained at the base speed in this case. The power factor at the maximum speed is high, and the current is not increased in the flux-weakening region used. The lowest value of the flux density in the permanent

Table 3: Calculated results

	Design A	Design B	Design C
Outer diameter of stator core (mm)	207	181	182
Inner diameter of stator core (mm)	130	110	110
Core length (mm)	200	235	220
Mass of active parts mm (kg)	51.0	45.4	42.8
Open-circuit voltage (V)	156	176	161
Maximum rms current (A)	345	313	356
Energy efficiency of drive train	0.777	0.784	0.772
Energy efficiency of motor	0.959	0.963	0.957
Energy losses per driving cycle (kWh)	1.11	1.07	1.154
Energy losses Wd (kWh)	9390	9040	9680
Cost of motor materials Cm (ECU)	372	386	362
Cost of converter Cc (ECU)	1570	1460	1610
Cost of weight cmmm (ECU)	1200	1070	1010
Cost of energy losses cdWd (ECU)	1840	1770	1900
Cost of extra batteries cbWd (ECU)	1950	1880	2010
Objective function C (ECU)	6930	6560	6890

magnets was, however, obtained for a sudden short circuit. The minimum feasible thickess of the permanent magnets is about 4.5 mm to avoid permanent demagnetization of the magnets.

The minimum value of the inner diameter of stator core was set to 110 mm. The optimization process converged to this limit. The cost of motor materials is slightly higher for Design B than for Design A. On the other hand, all the other costs are reduced, resulting in a value of the objective function that is lower than the original one.

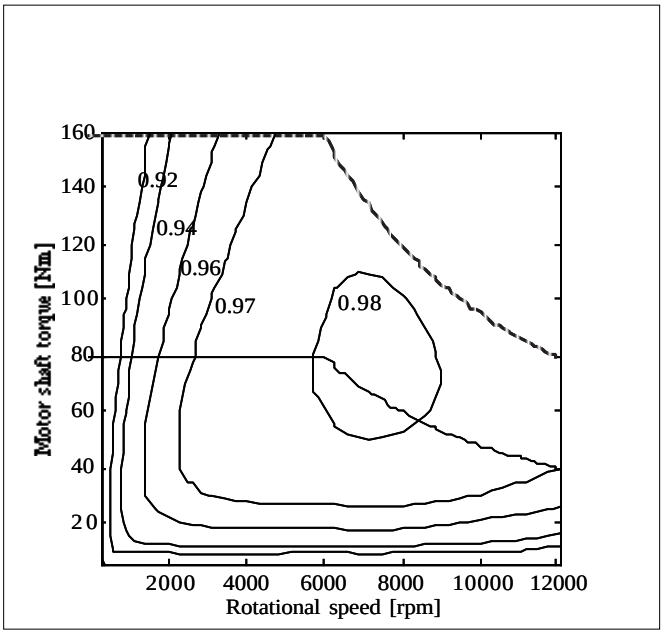

Figure 9: Calculated constant-efficiency curves of Design B

The open-circuit voltage of Design B is 0.80 p.u. A lower value of the open-circuit voltage would reduce both the iron losses at light loads at low speeds and the losses caused in the stator winding by the flux-weakening current component. On the other hand, a low open-circuit voltage increases the rating and losses of the converter.

Table 3 also shows the result obtained for a modified objective function, in which the losses of the mechanical transmission as well as the price and losses of the converter were neglected (Design C). In this case, the motor becomes lighter and the motor losses increase, as compared with Design B. Simultaneously, the open-circuit voltage is decreased and the current is increased, since the design is not influenced by the converter rating and losses.

7 Conclusions

A hybrid electric vehicle drive operates in a wide range of speeds and loads, and it is thus relevant to evaluate the total energy consumption (or energy efficiency) of the electric motor by driving-cycle simulation. As the drive line comprises the power-electronic converter and the mechanical transmission as well, the energy consumption of the whole drive line should be evaluated. This makes it possible to compare different machine designs adequately. The optimization of the machine can be based on the variation in the manufacturing costs, weight and losses of the drive line, and the variation in the battery cost and weight. The calculated results

show that the motor design and properties are influenced by the definition of the objective function. The predicted energy efficiency of the optimized inset-magnet motor is over 96%.

References

[1] G. Henneberger, G. Bailly, and J.R. Hadji-Minaglou, "Design and comparison of different motor types for electric vehicle application," in *EVS-11 Symposium Proceedings*, Florence, Italy, September 27-30 1992, vol. 1.

[2] D.F. Gosden, "Wide speed range operation of an ac pm ev drive," in *EVS-11 Symposium Proceedings*, Florence, Italy, September 27-30 1992, vol. 1.

[3] J. Luomi, J. Lindström, and J. Hellsing, "Design and analysis of electrical motors for a hybrid electric vehicle," in *IEEE/Stockholm Power Tech Conference Proceedings*, Stockholm, Sweden, June 18-22 1995, vol. Electrical Machines and Drives, pp. 274–279.

[4] T. Sebastian and G.R. Slemon, "Operating limits of inverter-driven permanent magnet motor drives," *IEEE Transactions on Industry Applications*, vol. 23, no. 2, pp. 327–333, March 1987.

[5] R.F. Schiferl and T.A. Lipo, "Power capability of salient pole permanent magnet synchronous motors in variable speed drive applications," *IEEE Transactions on Industry Applications*, vol. IA-26, no. 1, pp. 115–123, January 1990.

[6] W.L. Soong and T.J.E. Miller, "Field-weakening performance of brushless synchronous ac motor drives," *IEE Proc.-Electr.Power Appl.*, vol. 141, no. 6, pp. 331–340, November 1994.

[7] A. Hedman, "Transmission and vehicle simulation models for a hybrid electric vehicle," Tech. Rep. R-96-01, Department of Electric Power Engineering, Chalmers University of Technology, School of Electrical Engineering, Göteborg, Sweden, May 1996.

[8] "Electric vehicle energy consumption and range test procedure," 1995, SAE Standard J1634.

Permanent-Magnet Motor for a Hybrid Electric Vehicle

J. Lindström, J. Luomi, J. Hellsing*
Department of Electric Power Engineering
Chalmers University of Technology
S-412 96 Göteborg, Sweden
Phone +46-31-772 1636, Fax +46-31-772 1633
E-mail: joachim.lindstrom@elkraft.chalmers.se
* Present address: Volvo Car Corporation
S-405 08 Göteborg, Sweden

1998

Abstract

The paper deals with a 100 kW permanent-magnet synchronous motor of the inset-magnet type for a hybrid electric vehicle. The motor characteristics are evaluated by finite element analysis and driving simulations. The optimization of the motor is based on an objective function including the energy losses, weights and production costs of the electric drivetrain, as well as the amount of batteries required in a pure-electric operation. The experimental motor has a high efficiency in a wide operating region. A calorimetric method is used for measuring the losses of the machine.

1 Introduction

In electric and hybrid electric vehicles, the basic requirement for the electric drivetrain is high efficiency. The efficiency of the whole drive system should be high in a wide range of speeds and loads for obtaining a wide driving range in pure-electric driving or a satisfactory fuel efficiency when using the internal combustion engine. In addition, low weight and small volume as well as low production cost and high reliability are crucial for mass-produced cars.

When choosing the electrical motor for the vehicle drive, a permanent-magnet synchronous motor can offer advantages in terms of high efficiency and specific power. One of the possible choices is the inset-magnet design [1] shown in Fig. 1. This permanent-magnet motor type offers effective utilization of the permanent magnets and can be designed for good flux-weakening properties [2], [3], [4]. In

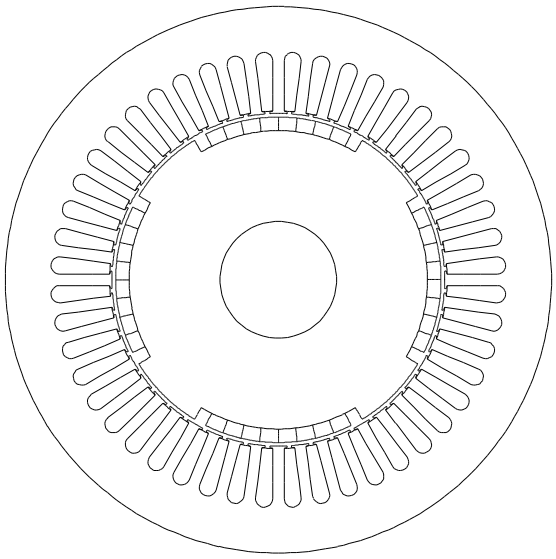

Figure 1: Cross-sectional geometry of a four-pole inset-magnet motor

the design of the motor, the total energy consumption, the total weight and the total production cost of the drivetrain should be accounted for. The design can be based on mathematical optimization combined with numerical computation of the motor properties by the finite element method and driving simulations [3] , [5].

This paper deals with the design and analysis of a 100 kW permanent-magnet synchronous motor for a series hybrid electric vehicle. A goal of the study has been to develop methods for the analysis and design of the electrical motor as a part of the drive system, and a special emphasis is put on the energy efficiency of the drivetrain.

2 Drive specification

The electric drivetrain of a series hybrid electric vehicle consists of a power-electronic inverter, an electrical motor and a mechanical transmission as illustrated in Fig. 2. The electric energy is supplied by the battery or the auxiliary power unit (APU), which usually consists of an internal combustion engine and a generator.

The series hybrid electric vehicle is required to reach a performance of 150 km/h top speed and 10.5 s acceleration time from 0 to 100 km/h, and the vehicle mass is 1700 kg. A two-speed mechanical transmission was chosen as a compromise between the size of the electrical motor and the size and complexity of the transmission. Table 1 shows the performance required of the motor [3] The maximum

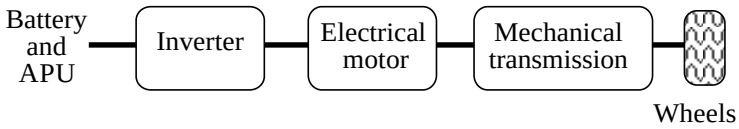

Figure 2: The components of the electric drivetrain of a series hybrid electric vehicle

Table 1: Motor performance

Nominal power	50 kW
Maximum power (3 min)	100 kW
Nominal speed	6 000 rpm
Maximum speed	12 000 rpm

motor speed is constrained by the maximum speed of the transmission, and the maximum-to-nominal speed ratio of 2 is chosen for the motor as the two-speed transmission is used. Above the nominal motor speed, flux weakening is applied to achieve the constant-power operation.

3 Motor design

3.1 Analysis

A method based on the finite element solution of the magnetostatic field is used to compute the characteristics and parameters of the machine. Furthermore, a time-stepping finite element method is used for the prediction of the iron losses and the cogging torque [6], [7] as well as the demagnetization of the permanent magnets and the eddy current losses in the magnets [2]. The losses should be evaluated for varying speed and load in the whole operating region of the motor, but the time-stepping finite element method consumes plenty of computer time. Therefore, analytical models were developed for interpolating different loss components between computed points, allowing the operating region to be analyzed based on six time-stepping computations [3].

In addition to the losses of the motor, the losses of the other components of the drive train are calculated. The converter losses are predicted by means of analytical expressions based on the motor current, the power factor, the dc voltage, the switching frequency and the transistor parameters [8]. For the mechanical transmission, a loss model depending on the wheel torque, the vehicle speed and the gear ratio was developed [9]. The losses of the motor, mechanical transmission and power electronics are presented as loss charts in the speed-torque plane for evaluating the losses of the drivetrain in the whole operating region. In addition,

the losses of the batteries are approximately taken into account by means of a charger efficiency and a battery efficiency.

The drive operates in a wide range of speeds and loads. To compare two drivetrain designs from an efficiency point of view, the total energy consumption is the only relevant entity. Simulation according to a specific driving pattern is, therefore, necessary. The energy consumption of the drivetrain is evaluated for an expected lifetime of the vehicle by a simulation of the vehicle dynamics over standardized driving cycles, using the data of the loss charts for the calculation of the drivetrain losses. Furthermore, a thermal network is used to model the temperature distribution in the motor both in steady and transient state.

3.2 Optimization

The optimization of the motor is based on the minimization of an objective function consisting of contributions from:

- the production cost of the electric drivetrain
- the weight of the electric drivetrain
- the energy consumption of the electric drivetrain over standardized driving cycles
- the weight and cost of batteries needed in pure electric-vehicle operation for a given minimum driving range.

The minimization problem is defined in terms of eight primary variables. The approach chosen for the optimization corresponds to the method presented by Nurdin et al. [10]. The essential point of this approach is the synthesis consisting of the creation of feasible designs prior to optimization. First, the designs must be feasible, i.e., the requirements of maximum torque, maximum temperature and minimum flux density in permanent magnets must be fulfilled. Then, the optimization problem is defined as finding a feasible design which minimizes the objective function. The optimization is carried out by using a simple search method [3], [5].

3.3 Experimental motor

A full-scale experimental motor was built based on the optimization result. The iron core is made of low-loss steel sheet of 0.2 mm thickness, and the NdFeB

permanent magnets are made of electrically insulated pieces in order to reduce the eddy-current losses. A pre-tensed carbon-fiber composite retaining sleeve is fitted around the rotor to ensure sufficient mechanical strength of the rotor construction at the maximum speed. A compact motor design is achieved by using water-cooling of the stator frame. Some of the dimensions and properties of the motor are presented in Table 2.

Table 2: Motor data

Stator outer diameter	186 mm
Stator inner diameter	110 mm
Stack length	220 mm
Overall mass	62 kg
Mass of active parts	37 kg
Mass of NdFeB permanent magnets	1.7 kg
Nominal voltage	220 V
Open-circuit voltage	0.79 p.u.
Direct-axis synchronous reactance	0.34 p.u.
Quadrature-axis synchronous reactance	0.80 p.u.
Nominal efficiency	96%

4 Losses and efficiency

4.1 Loss minimization by control

In the flux-weakening region, a negative direct-axis component is injected to the armature winding for reducing the flux level of the machine [11]. Below the nominal speed, the losses of the motor can be reduced by controlling the direct-axis current. Based on the calculated motor characteristics, three different control strategies were investigated for reducing the losses at partial load. Fig. 3 illustrates the corresponding motor voltage as a function of load at nominal speed. Curve A shows the often recommended motor-control strategy which is based on finding the maximum torque per current ratio, i.e., the lowest possible resistive losses of the armature winding [12], [11]. This means that the voltage is lowered towards the open-circuit voltage as the load is reduced.

Another alternative is to minimize the predicted total motor losses [3]. As shown by curve B in Fig. 3, the voltage in this case kept at a slightly lower value, since a reduced voltage corresponds to a lower flux level and reduced iron losses. Simultaneously, a higher armature current and increased resistive losses are obtained. Finally, it is possible to minimize the predicted drivetrain losses including the motor losses and the inverter losses [5]. Inverter losses are largely due to the motor

current, which explains why the optimal voltage shown by curve C in Fig. 3 is between the two previous curves.

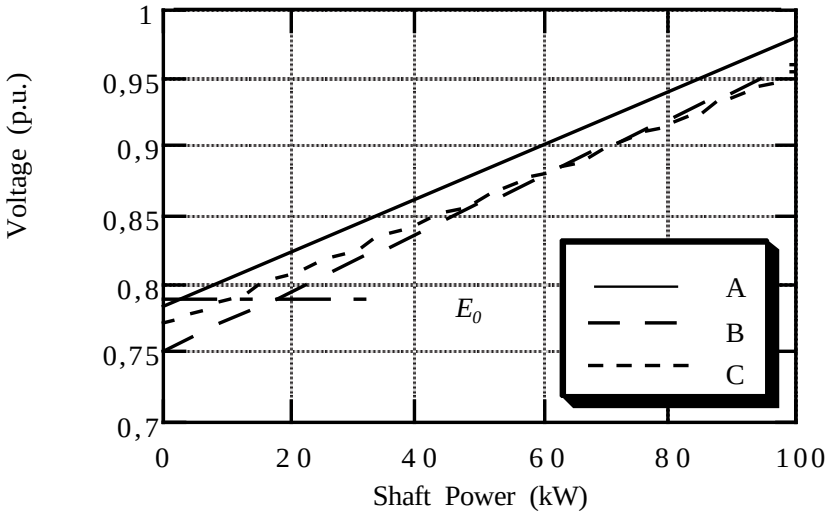

Figure 3: Voltage control strategies at 6000 rpm for (A) maximum torque-to-current ratio, (B) minimum motor losses and (C) minimum drivetrain losses. E_0 is the open-circuit voltage

4.2 Efficiency map

Fig. 4 shows predicted constant-efficiency curves of the motor. The predicted maximum efficiency of the motor is 97.1 % and that of the inverter and motor combination is 95.4 %.

4.3 Driving simulations

The SAE driving cycle J1634 used in the driving simulations is shown in Fig. 5 [13]. The driving cycle consists of both city driving and highway driving. The driving cycle is 28 496 meters long and lasts for 2136 seconds at an average speed of 48 km/h. The top speed is 96.4 km/h and the maximum acceleration 1.50 m/s^2. The vehicle spends 64 % of the time and 42 % of the distance in city driving, and the rest in highway driving.

The output from the driving simulation is the drivetrain energy consumption. Fig. 6(a) shows the losses of each drivetrain component at nominal load and nominal speed, and Fig. 6(b) shows the corresponding losses as an average during the driving cycle. The different motor loss components are shown in Fig. 7. In Fig. 7(a), the different motor loss components are shown at nominal load and nominal speed; winding losses and iron losses are almost equal in this case. In Fig. 7(b) the

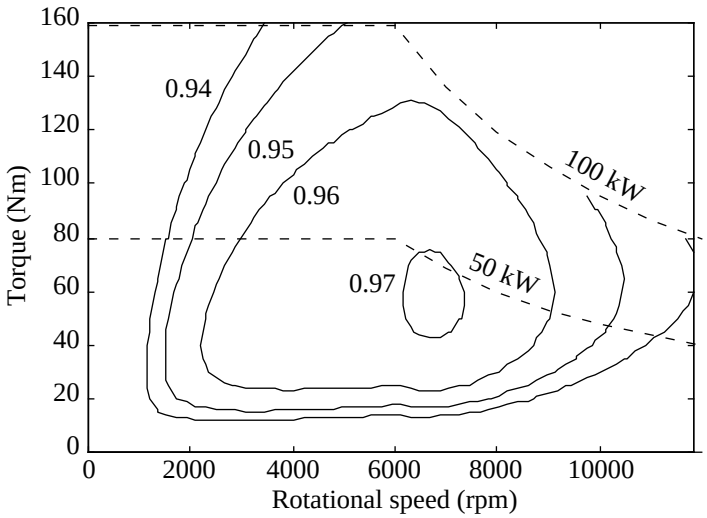

Figure 4: Predicted efficiency map of the motor

different motor loss components are shown as an average during the driving cycle; in this case, iron losses clearly dominate the motor losses. The predicted energy efficiency of the motor is 95.4 % and that of the inverter and motor combination is 92.8%.

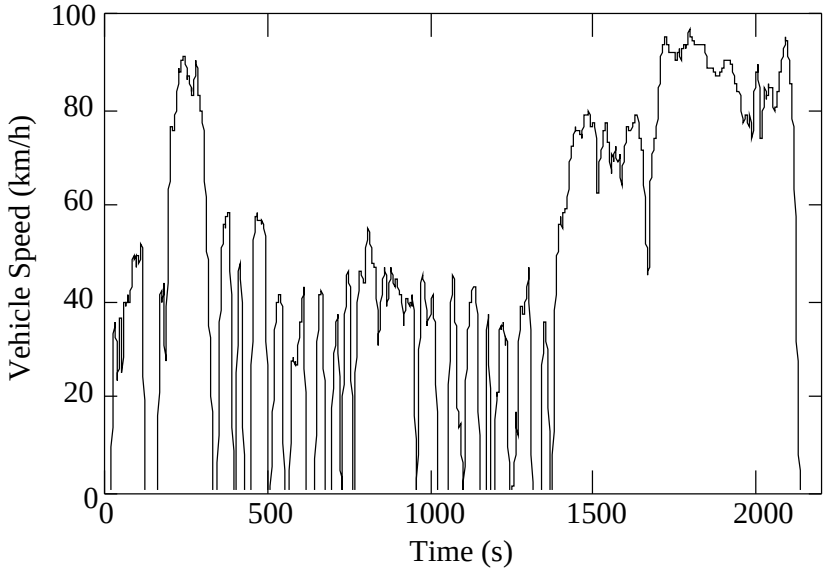

Figure 5: The J1634 driving cycle

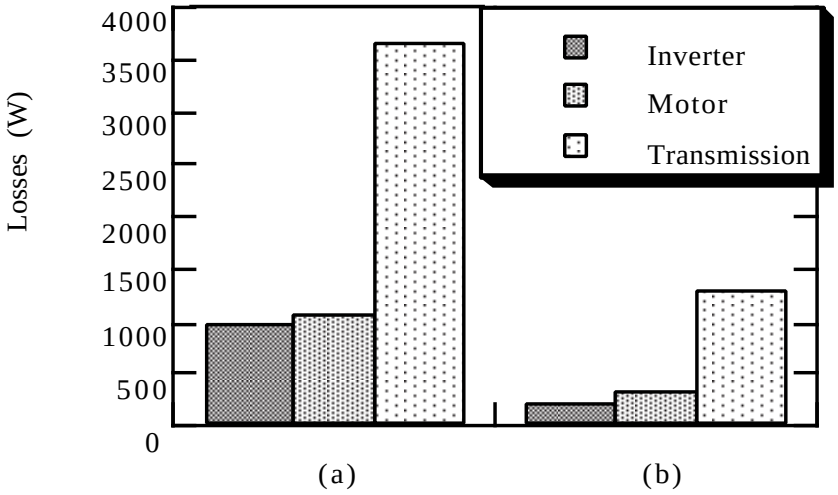

Figure 6: Drivetrain losses: (a) losses at nominal load and nominal speed, (b) average drivetrain losses during driving

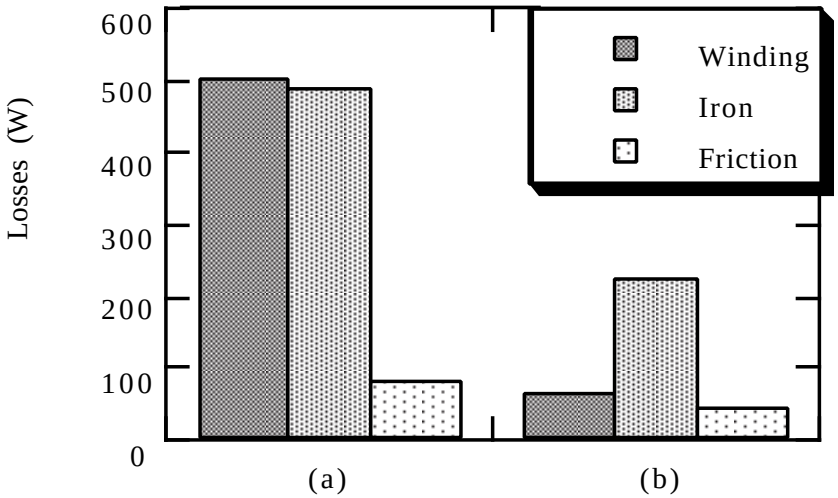

Figure 7: Motor losses: (a) losses at nominal load and nominal speed, (b) average motor losses during driving

5 Laboratory set-up

In addition to the experimental motor, an inverter was constructed for the drive system. It is equipped with intelligent IGBT-modules and uses water-cooling, which allows a compact design suitable for vehicle application. Signals are optically transferred between the control system and the power circuit. The control is implemented using a controller board based on a TMS 320C30 digital signal processor.

The laboratory set-up used for testing the motor is shown in Fig. 8. Power is supplied to the inverter by a grid-connected thyristor rectifier and the dc-link voltage is smoothed by an LC filter. The experimental motor is mechanically connected to a dc machine via a torque transducer and a reduction gearbox. The dc machine is controlled by a grid-connected thyristor converter.

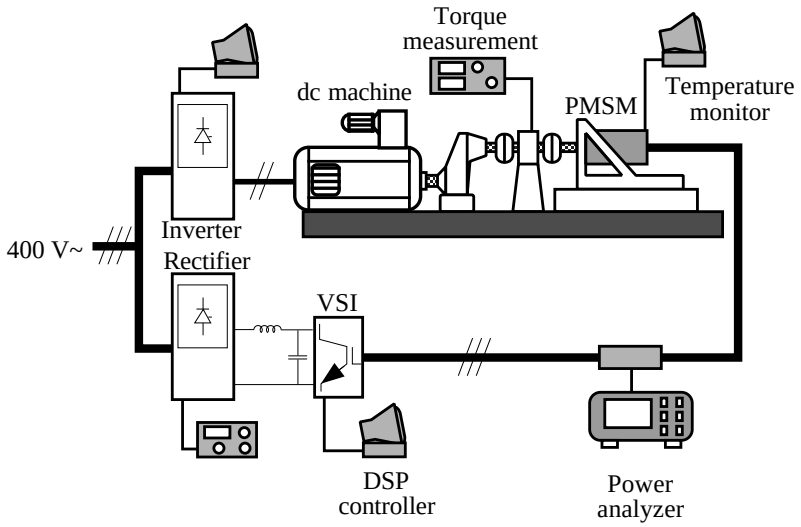

Figure 8: Laboratory set-up

The set-up includes equipment for measurements of mechanical, electrical and thermal quantities. Thermocouples are installed in the coil sides and end windings of the experimental motor to monitor the thermal state during the tests. A data acquisition system is used for monitoring the measured signals, and electrical quantities are also measured by a three-phase power analyzer.

Software implementation of the control provides flexibility and makes it possible to investigate various strategies. The set-up allows measurements with a high accuracy in a wide range of speeds and loads. Computerized control and data acquisition units make it possible to monitor the system properties both in dynamic and in steady state.

6 Calorimetric loss measurement

Because of the high efficiency of the system, special attention is given to the accuracy of loss measurement. The input-output method, in which the losses are found from measurements of the electrical input power and the mechanical output power, involves problems with the accuracy if the efficiency is high.

The experimental motor has a water-cooling system of counter-flow type as illustrated in Fig. 9. The cooling water flows in channels that have been made in the stator frame. Therefore, it is easy to use a calorimetric method for measuring the losses [14]. Platinum resistance sensors are used to measure the temperature rise of the cooling water, and the volumetric flow rate is measured by means of a turbine flow sensor. A calibration of the instruments and sensors was made to improve the accuracy by taking the characteristics of the individual sensors into account.

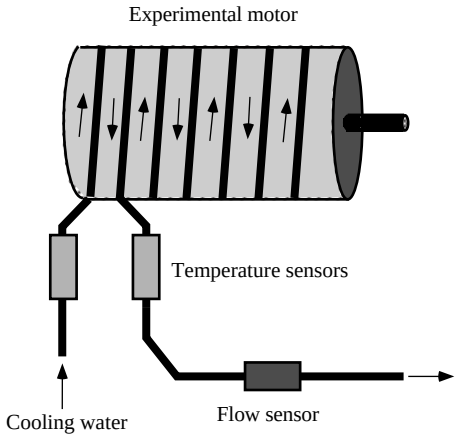

Figure 9: Calorimetric measurement

Losses which are not dissipated through the cooling medium are not measured directly, and it is important to minimize this thermal leakage. A thermal model was developed to evaluate the leakage and improve the system accuracy. Radiation leakage is estimated with a black body model and convection is taken into account by analytical means. Conduction, being the largest part of the leakage, is modeled by finite element analysis of the supporting structure and measurements of the surface temperatures of the shaft and couplings.

In the steady-state tests, thermal equilibrium was considered to have been achieved when the temperature rise of the cooling water varied less than $\pm 1\%$ in one hour [15]. The temperature dependent variations in the density and specific heat of the cooling water were taken into account as well as the influence of the surrounding air temperature. Fig. 10 is an example of the measured results. The efficiency of the inset-magnet machine is shown in a case where the machine operates as a

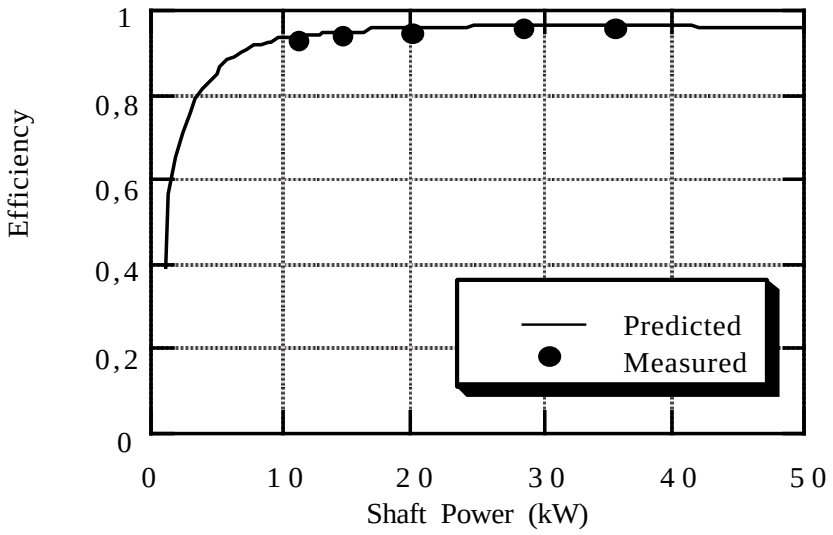

Figure 10: Predicted and measured efficiency in generator operation at 6000 rpm

generator with resistive load. The estimated total thermal leakage during the tests was adjusted to less than 8 W, and the accuracy estimation shows that the total losses of the experimental motor are determined within $\pm 2.7\%$. This value can be compared with the error of $\pm 21\%$ estimated for the input-output method. The measured losses are higher than the predicted ones; the maximum discrepancy is 20 %. The calorimetric measurements will be used for the further analysis of the iron losses, additional losses and friction losses of the machine.

7 Conclusion

A permanent-magnet motor of the inset-magnet type can be designed for a high efficiency in an electric vehicle application. Important aspects in the optimization procedure are accurate computation of the losses and the energy efficiency of the whole drivetrain. Loss measurements by means of the calorimetric method yield a high accuracy.

References

[1] T. Sebastian and G.R. Slemon, "Operating limits of inverter-driven permanent magnet motor drives," *IEEE Transactions on Industry Applications*, vol. 23, no. 2, pp. 327–333, March 1987.

[2] J. Luomi, J. Lindström, and J. Hellsing, "Design and analysis of electrical motors for a hybrid electric vehicle," in *IEEE/Stockholm Power Tech*

Conference Proceedings, Stockholm, Sweden, June 18-22 1995, vol. Electrical Machines and Drives, pp. 274–279.

[3] J. Lindström, J. Hellsing, and J. Luomi, "Design of high-efficiency electrical motors for a hybrid electric vehicle," in *EVS-13 Proceedings*, Osaka, Japan, October 13-16 1996, vol. II, pp. 64–69.

[4] S. Van Haute, S. Henneberger, K. Hameyer, R. Belmans, J. De Temmerman, and J. De Clercq, "Design and control of a permanent magnet synchronous motor drive for a hybrid electric vehicle," in *EPE'97 Proceedings*, Trondheim, Norway, September 8-10 1997, vol. 1, pp. 1570–1575.

[5] J. Hellsing, "Design and optimization of a permanent magnet motor for a hybrid electric vehicle," Licentiate thesis, School of Electrical and Computer Engineering, Chalmers University of Technology, Göteborg, Sweden, March 1998, Tecnical Report No.282L.

[6] A. Arkkio, "Finite element analysis of cage induction motors fed by static frequency converters," *IEEE Transactions on Magnetics*, vol. 26, no. 2, pp. 551–554, March 1990.

[7] A. Arkkio and A. Niemenmaa, "Estimation of losses in cage induction motors using finite element techniques," in *Proceedings of the International Conference on Electrical Machines*, Manchester, U.K, September 15-17 1992, vol. 2, pp. 317–321.

[8] J.H. Rockot, "The calculation of transistor losses in motor drive inverters," in *PCI,Proceedings*, Chicago, Illinois, October 22-25 1985, pp. 122–136.

[9] A. Hedman, "Transmission and vehicle simulation models for a hybrid electric vehicle," Tech. Rep. R-96-01, Department of Electric Power Engineering, Chalmers University of Technology, School of Electrical Engineering, Göteborg, Sweden, May 1996.

[10] M. Nurdin, M. Poloujadoff, and A. Faure, "Synthesis of squirrel cage motors: A key to optimization," *IEEE Transactions on Energy Conversion*, vol. 6, no. 2, pp. 327–333, June 1991.

[11] S. Morimoto, M. Sanada, and Y. Takeda, "Effects and compensation of magnetic saturation in flux-wweakening controlled permanent magnet synchronous motor drives," *IEEE Transactions on Industry Applications*, vol. 30, no. 6, pp. 1632–1637, November 1994.

[12] T.M. Jahns, G.B. Kliman, and T.W. Neumann, "Interior permanent magnet synchronous motors for adjustable speed drives," *IEEE Transactions on Industry Applications*, vol. 22, no. 4, pp. 738–747, July 1986.

[13] "Electric vehicle energy consumption and range test procedure," 1995, SAE Standard J1634.

[14] T. Larsson, "Calorimetric measurement of losses of a permanent magnet synchronous motor," M.Sc.thesis, Department of Electric Power Engineering, Chalmers University of Technology, Göteborg, Sweden,, June 1998, Report No.27E.

[15] IEC Publication 34-2A, "Methods for determining losses and efficiency of rotating electric machinery from tests (excluding machines for traction vehicles), measurement of losses by the calorimetric method," Tech. Rep., 1974.

Thermal Model of a Permanent-Magnet Motor for a Hybrid Electric Vehicle

Joachim Lindström

Department of Electric Power Engineering
Chalmers University of Technology
Göteborg, Sweden

April, 1999

Abstract

The report describes a thermal model of a water cooled permanent-magnet motor, designed and optimized for a hybrid electric vehicle. The study is based on previously published work on thermal modeling of small induction motors. A lumped-parameter model was implemented as a thermal network, using a constant reference temperature both for steady-state calculations and transient simulations. Temperature measurements of a full-scale experimental motor show good agreement with the calculated temperatures, using measured losses applied to the thermal model. The relative error of the temperature rise is less than 12 %. A sensitivity analysis of the model showed a maximum temperature deviation of $\pm$12 K, when the thermal resistances were changed from +100 % down to -50 % of the nominal value. Especially important components in the modeling are the thermal contact resistance between yoke and frame and the heat transfer from coil sides to stator teeth.

Contents

List of Symbols

Latin		Greek	
A	area	α	heat transfer coefficient
a	distance	δ	air-gap
b	distance	γ	angle
C	capacitance	λ	thermal conductivity
$\mathbf{C}$	capacity matrix	ν	kinematic viscosity
d	diameter, distance	Ω	angular frequency, mechanical
G	conductance	ω	angular frequency, electrical
$\mathbf{G}$	conductance matrix	θ	temperature rise
h	height, distance	Θ	temperature rise vector
l	length	ρ	density
Nu	Nusselt number	τ	pole pitch
n	number of item	ψ	flux linkage
P	power, heat flow		
$\mathbf{P}$	power loss vector		
p	pole-pair number		
Q	slot number		
r	radius	**Subscripts**	
R	resistance		
Ta	Taylor number	A	air
x	distance	Al	aluminum
y	distance	av	average
		b	bearing
		c	core
		Cu	copper
		d	tooth, teeth
		el	electrical
		ew	end winding
		fin	fin
		fr	frame
		Fe	iron
		I	insulation
		m	mechanical
		Q	slot
		r	rotor
		s	stator
		sh	shaft
		th	thermal
		y	yoke

1 Introduction

Heat is dissipated in all energy conversion systems as a consequence of losses. The requirement for proper thermal modeling is obvious; to prevent overheating and eventually damage inflicted on the system. Knowledge of thermal behavior in different situations can prevent overheating, but can also improve the utilization of the system at normal operation.

Electric machinery has been used in industrial applications since the end of the 19:th century, which means that the design procedure has matured. Despite this fact, electrical machines do overheat, usually due to improper handling or unforeseen faults. Development of a machine type that differs from well-known standard machines requires attention to the thermal aspects since, in the end, it is always the thermal constraints that will determine the power rating of the machine. No matter how sofisticated the tools for designing the electric and magnetic circuits are, ending up with a non-feasible machine is a waste of time and other resources.

An electric machine intended for vehicle propulsion has been developed at the department, as part of a research project during 1995-1997. One important task for the project was to develop methods for the analysis and optimization of an electric motor as a part of the drive system for a hybrid electric vehicle (HEV). The feasibility of a design was determined partly by the thermal characteristics, which had to be predicted by using computer simulations.

This report describes a small thermal network for modeling a permanent-magnet synchronous machine (PMSM). Thermal networks are used frequently for modeling electrical machines and many different solutions of various complexities have been presented in the literature [1] [2] [3] [4]. The model presented emanates from studies of thermal modeling of small induction motors, conducted by Kylander [1]. The work presented in the following chapters is a development of Kylander's model in order to adapt it for the design and optimization of a PMSM.

2 The Lumped-Parameter Thermal Model

2.1 The Experimental PMSM

The machine type chosen for the hybrid electric vehicle is a synchronous motor with an inset-magnet rotor design as shown in Fig. 1. The iron cores of the stator and rotor were made of thin laminations of electrical sheets and the permanent magnets were made of electrically insulated pieces, in order to reduce the eddy-current losses. A pre-tensed carbon-fiber composite retaining sleeve was used to ensure sufficient mechanical strength of the rotor construction at the maximum speed, 12000 rpm. Furthermore, water-cooling of the stator frame was chosen to achieve a compact motor construction, and by making the cooling channels spiral shaped, the temperature differences along the frame surface can be kept small. A picture of the frame construction is shown in Fig. 2.

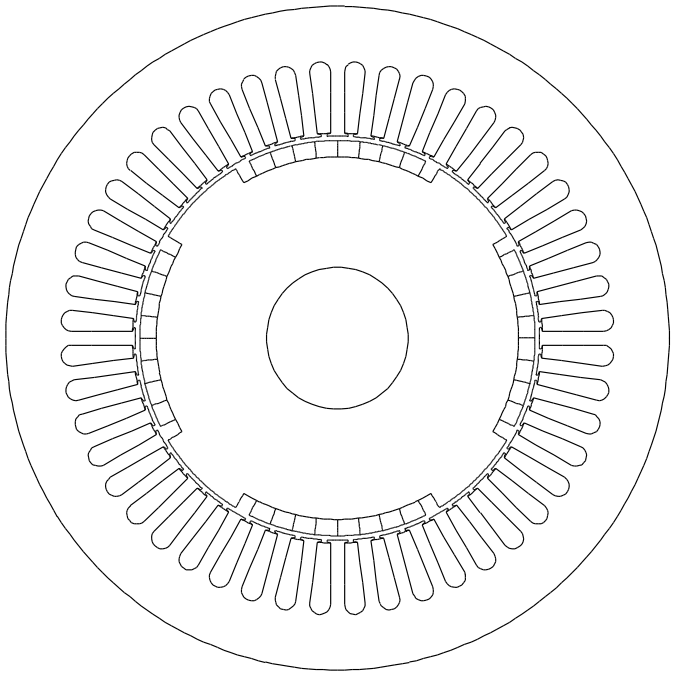

Figure 1: Cross-sectional geometry of the inset-magnet motor

An illustration of the mechanical construction is shown in Fig. 3. Detailed information on the geometrical properties of the motor is given in Table 1 and the material data is presented in Table 2. A complete description of the motor is presented by Hellsing [5].

The final motor design was determined by a univariant optimization procedure, in which each set of machine parameters was first validated in terms of feasibility [5] [6]. A design was regarded as feasible if it could deliver the rated output power

Figure 2: The stator frame during manufacturing

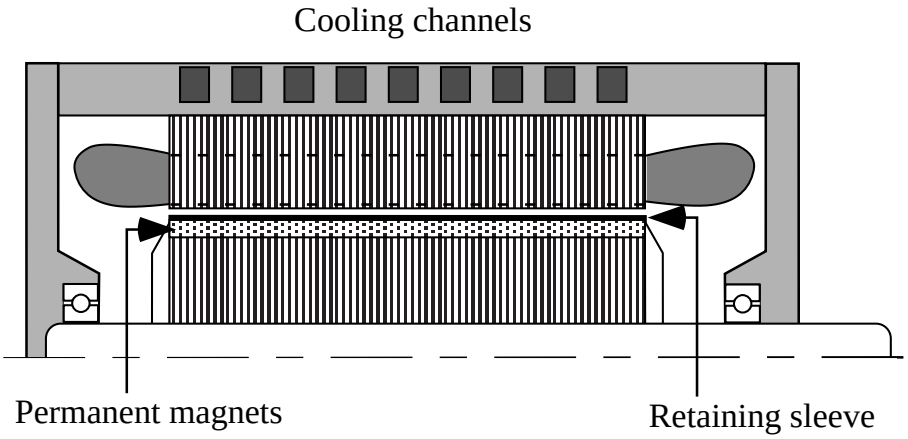

Figure 3: An axial cut of the PMSM

Table 1: Geometrical data of the experimental PMSM.

Stator core length	231 mm
Lamination filling factor	0.965
Stator inner diameter	110 mm
Stator outer diameter	189 mm
Number of stator slots	48
Yoke thickness	16.4 mm
Tooth width	3.5 mm
Slot opening width	1.5 mm
Tooth height	20.4 mm
Slot area	89.8 mm^2
Number of pole pairs	2
Slot filling factor	0.45
Mechanical air gap	0.3 mm
Magnet thickness	5.0 mm
Rotor core outer diameter	107.1 mm
Rotor core inner diameter	64.6 mm
Magnet-pitch /pole-pitch ratio	0.65
Iron-pitch /pole-pitch ratio	0.29
Retaining sleeve thickness	0.75 mm

Table 2: Material data used for the model

Machine part	Material	Density (kg/m^3)	Heat conductivity (W/mK)	Specific heat capacity (J/kg K)
Lamination	EBG, NO20	7600	38	460
Winding	Copper (Cu)	8900	395	385
Frame, end shields	Aluminum (Al)	2705	230	900
Shaft	Steel	7800	51	460
Magnets	NeFeB	9	7500	
Winding impregnation	unsaturated polyester	1350	0.2	1700
Air gap, internal air	air	1.23 (at 0°C)	0.0243 (at 0°C)	1010
Retaining sleeve	carbon fiber composite	1800	0.5	
Magnet insulation	glass fiber		0.5	
Slot insulation	mylar film		0.2	

within the specified range of temperature rise and without any risk for permanent demagnetization of the permanent magnets. Table 3 shows the specifications used as constraints in the optimization, where approximate thermal margins were included to allow local hot spots [5].

Table 3: Constraints and limits used in the optimization

Quantity	Limit
Winding temperature	130°C
Magnet temperature	100°C
Continuous output power	50 kW
Intermittent output power (max 3 min.)	100 kW

The temperature distribution in the machine was determined for each set of machine parameters by calculations of steady-state operation and simulations of transient operation. Special attention was given to the temperatures in the stator windings, the bearings and the permanent magnets mounted on the rotor surface.

2.2 A Small Thermal Network

In general, the geometrical complexity of an electrical machine requires a large thermal network if a solution with a high resolution of the temperature distribution is required. Instead of using a large, complex model, the geometrical symmetries of the machine were used to reduce the order of the model. The distributed thermal properties have been lumped together to form a small thermal network, representing the whole machine.

In some cases, a small model can be sufficient if calculations with a coarse temperature distribution yields satisfactory results. In motor design work, it is usually sufficient to calculate the temperatures with a high accuracy in a few, especially important machine parts. From experience, it is known where the critical temperatures occur and in what range they should be.

The PMSM has some differences in construction compared with a totally enclosed fan cooled (TEFC) induction motor. Water-cooling of the stator frame simplifies the model for heat transfer between the machine and the coolant. Air friction is an important subject, since the related losses become more important due to the high rotational speed. The losses in the bearings are also increased because of the high rotational speed, and further, the heat transfer through the internal air is more complicated to model due to increased turbulence. The rotor losses of the experimental PMSM are very small compared with the rotor losses of an induction motor. On the other hand, due to the rotor construction, the heat transfer between stator and rotor is smaller compared with an induction motor.

The eight-node thermal network shown in Fig. 4 was used to model the PMSM. Each node represents a specific part or region of the machine and the thermal resistances between the nodes include complex processes, such as two-dimensional and three-dimensional heat flow, convection, internal heat generation, and variations in material properties.

2.3 The Node Representation

In this section, the choice of the nodes in the thermal network is discussed. Different characteristics of a specific machine part, such as temperature distribution, mechanical complexity and material properties were considered when the nodes and their assignments were selected.

Heat transfer between the machine and the cooling medium was modeled by assuming a constant average temperature of the coolant, which simplifies the thermal network equation system. The construction of the stator frame, shown in Section 2.1, gives a homogeneous temperature distribution very close to the conditions assumed in the model. The solution of the equation system representing the machine gives the temperature rises of the machine parts in reference to the coolant temperature. A worst case approach is achieved when the temperature of the

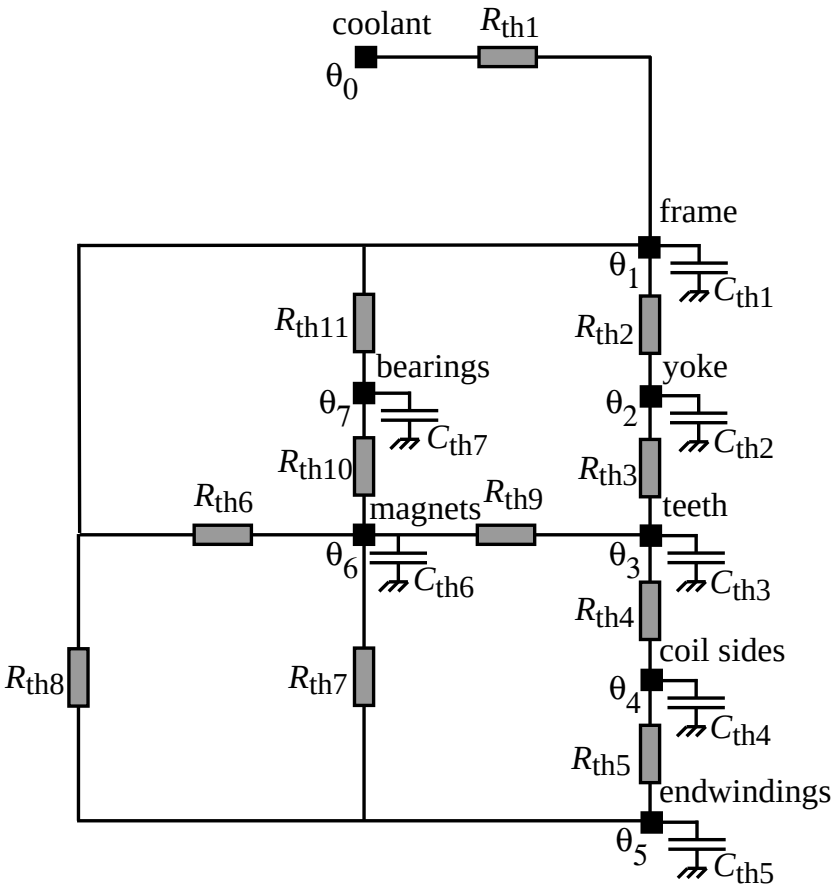

Figure 4: Thermal network

coolant is assumed to be the highest temperature that would possibly appear in the application.

Two nodes were used for the stator core, which is the largest machine part usually exposed to temperature gradients of a large magnitude. The placement of one node in the yoke and one in the teeth was regarded as satisfactory, since the iron temperature itself is not crucial. The relevant quantity is, instead, the amount of heat transported from the coil sides and tooth tips to the coolant. Motor operation at high torque is associated with large heat dissipation in the machine windings. The highest temperature in the machine appears in the end windings, which implies that attention should be given to the heat flow from the end windings. In the model presented, there are two nodes representing the windings; one node for the end windings and one for the coil sides.

Predicting the temperature of the permanent magnets is of great importance. The behavior of the permanent-magnet material at increased temperature can involve risks for permanent demagnetization, and consequently, permanent damage to the machine [7]. For this reason, one node was assigned to the permanent magnets.

Bearing temperature is an important aspect when the lifetime of an electrical machine is estimated. Induction motors are often exposed to a high rotor temperature, with an increased bearing temperature as a consequence. A properly designed PMSM does not suffer from high rotor losses, but it is still important to investigate the bearings since the experimental motor operates at speeds above normal standard motors.

Empirical investigations are important for this kind of modeling, since they can provide information that is difficult, sometimes impossible, to obtain by analytical means. In addition, computer analysis using numerical methods, such as finite-element methods, is useful for developing more accurate lumped-parameter models.

3 Thermal Modeling of the Machine Parts

In this chapter, the thermal resistances of the network model are derived. Simplifications are generally made from geometrical symmetries and assumptions of perfect thermal insulation. First, the thermal resistances for the different machine parts are derived. Then, the thermal resistances of the model are calculated from the machine part resistances.

3.1 Stator Frame and Yoke

The stator frame is, in this case, cylindrical with a diameter much larger than the thickness. An approximate expression for the radial conductive thermal resistance of the frame is

$$R_{thfr} = \frac{h_{fr}}{\pi l_{Fe} \lambda_{Al} (d_{se} + h_{fr})} \tag{1}$$

where h_{fr} is the average thickness of the stator frame adjacent to the stator core, l_{Fe} is the stack length, d_{se} is the outer diameter of the stator core and λ_{Al} is the thermal conductivity of the frame material (Aluminum).

The stator yoke is modeled as a hollow, cylindrical stack of perfectly insulated iron sheets. Heat flow is, therefore, assumed to exist only in the radial direction. The heat conductivity of the insulation material is much lower than that of the iron sheets, which is accounted for by denoting the useful iron length

$$l_u = k_{Fe} l_{Fe} \tag{2}$$

where k_{Fe} is the iron space factor. The stator yoke thermal resistance for radial heat conduction is expressed as

$$R_{thys} = \frac{\ln\left(\frac{d_{se}}{2}\right) - \ln\left(\frac{d_s}{2} + h_s\right)}{2\pi l_u \lambda_{Fe}} \tag{3}$$

where d_s is the stator inner diameter, h_s is the tooth height and λ_{Fe} is the thermal conductivity of the ferromagnetic material.

Apart from the conductive heat resistance of the materials, the thermal resistance between the machine frame and the stator yoke includes a component of conductive resistance due to the interface between the two materials. Air pockets are present at the interface and influence the heat transfer, depending on the surface texture and the applied pressure. One possible approach to estimate the thermal contact

resistance is to introduce an equivalent gap [8]. The thermal contact resistance is defined by

$$R_{thcy} = \frac{g_e}{\lambda_g A_g} \tag{4}$$

where g_e is the equivalent gap, λ_g is the thermal conductivity of the gap and A_g is the equivalent gap area. Table 4 shows suggestions for the gap g_e in different machines [8].

Table 4: Equivalent air gap dimensions

Machine type	g_e (μm)
Cast iron frame or larger than 100 kW	50 .. 75
Aluminum frame or smaller than 100 kW	30 .. 40

Based on Kylander's results, the thermal contact resistance used is equal to the stator yoke thermal resistance [1], which was regarded as applicable to the experimental motor.

Thermal resistance between coolant and frame

The thermal resistance between the frame node and the coolant node, R_{th1}, is small and its influence on the final solution is of less importance, as will be seen in Section 4.3. The frame node is placed in the middle of the frame, as shown in Fig. 5, and the total thermal resistance from the coolant node to the frame node is thus

$$R_{th1} = \frac{1}{2} R_{thfr} \tag{5}$$

Thermal resistance between frame and yoke

The thermal resistance R_{th2} models heat flow between the stator yoke node and the frame node. It consists of the contributions from the yoke, the frame and the contact resistance between the yoke and the frame as described by

$$R_{th2} = \frac{1}{2} R_{thys} + \frac{1}{2} R_{thfr} + R_{thcy} \tag{6}$$

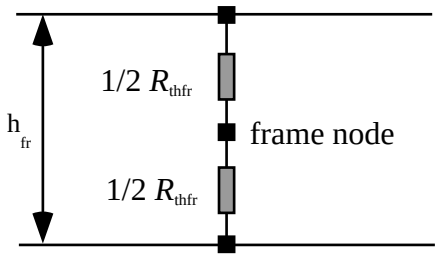

Figure 5: Thermal model of the stator frame

3.2 Stator Teeth

In a thermal network with a one-node representation of the stator teeth, the thermal resistances of all the individual teeth are considered to be in parallel with each other. Axial heat transfer is neglected because of the insulation between the stator iron sheets. The thermal resistance of the stator teeth is found from integration along a tooth in the radial direction, yielding

$$R_{thd} = \int_{y=0}^{h_s} \frac{1}{\lambda_{Fe} Q_s l_u x_d(y)} dy \tag{7}$$

where Q_s is the number of stator slots, $x_d(y)$ is the tooth width and y is the radial coordinate. The integral expression in Equation (7) can be replaced by an expression specific to the tooth geometry. The tooth geometry used in the experimental motor is shown in Fig. 6 and the expression for the stator teeth thermal resistance is [1]

$$\begin{aligned} R_{thd} = \frac{1}{\lambda_{Fe} Q_s l_u} \Bigg[& \frac{y_{d1}}{x_{d1}} + \frac{y_{d3}}{x_{d3}} + \frac{y_{d2}}{x_{d1} - x_{d2}} \\ & \left(\ln \left| \frac{x_{d1} y_{d2}}{x_{d1} - x_{d2}} \right| - \ln \left| y_{d2} - \frac{x_{d1} y_{d2}}{x_{d1} - x_{d2}} \right| \right) - \\ & - \frac{\pi}{4} + \frac{a}{\sqrt{a^2 - 1}} \arctan \left(\frac{a+1}{\sqrt{a^2 - 1}} \right) \Bigg] \end{aligned} \tag{8}$$

where

$$a = \frac{x_{d3} + 2y_{d4}}{2y_{d4}} \tag{9}$$

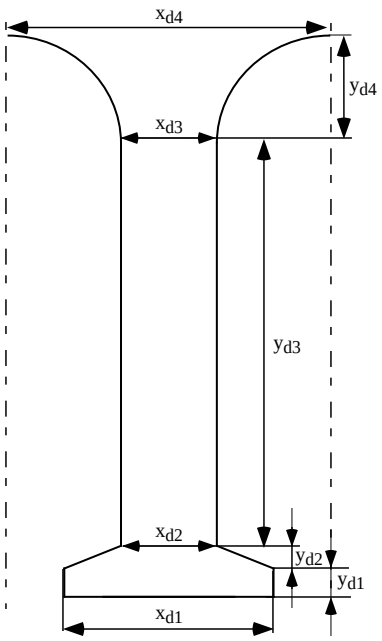

Figure 6: Stator tooth geometry

Thermal resistance between yoke and teeth

By assuming a homogeneous heat flow from the stator windings, it is possible to use a one-dimensional node configuration representing the thermal resistance between the stator yoke node and the teeth node. The expression is comprised of the thermal resistance of half the teeth and half the yoke, yielding

$$R_{th3} = \frac{1}{2}(R_{thys} + R_{thd}) \tag{10}$$

3.3 Stator Windings

Heat flow in the machine windings is present in the axial, radial and circumferential directions. The axial conduction provides a flow path for heat dissipated in the end windings and in the coil sides, which are embedded in the stator core. Heat flows from the coil sides, radially and circumferential across the slot insulation, into the stator core and further out to the coolant. A large portion of the total machine losses is transferred through this path and, consequently, it is a very important part of the modeling of the machine.

In a wound coil, the material properties and dimensions determine the thermal resistance along the conductors but in the directions perpendicular to the conductors, additional quantities must be considered to find the thermal properties. The

cross-sectional geometry of the conductors, the conductor insulation material, the impregnation material properties, the slot insulation and the air pockets in and around the coil influence heat conductivity and should, therefore, be taken into account.

Thermal resistance between coil side and teeth

Calculations of the thermal resistance perpendicular to the winding conductors were made by considering the insulated conductors and impregnation as a homogeneous body of slot material with uniform heat dissipation. A transformation to an equivalent rectangular slot shape with a uniform boundary temperature was made, as shown in Fig. 7 [1]. By neglecting the thermal resistivity of the conductor material, an equivalent thermal conductivity, λ_Q, of the slot material can be defined from the impregnation thermal conductivity, λ_{imp}, and the slot space factor k_Q. The dimensions of the rectangular slot is found from

$$d = d_I + d_A \tag{11}$$

$$b = \frac{x_{Q3} + x_{Q2}}{2} - 2d \tag{12}$$

$$h = \frac{2A_Q}{x_{Q3} + x_{Q2}} - 2d \tag{13}$$

where x_{Q2} and x_{Q3} are the slot widths shown in Fig. 8 and d is an equivalent insulation thickness comprised of the slot insulation thickness, d_I, and the equivalent air film thickness, d_A [1].

If the boundary temperature of the equivalent rectangular slot is assumed to be homogeneous and equal to the average stator teeth temperature, the thermal resistance between the coil side node and the stator teeth node is [1]

$$R_{th4} = \frac{R_x R_y}{Q_s l_u (R_x + R_y)} \left(1 - \frac{R_{x0} R_{y0}}{720(R_{x0} + R_{y0})} \right) \tag{14}$$

The per unit-length resistances in Equation (14) are

$$R_x = \frac{1}{2} \left(R_{ix} + \frac{R_{x0}}{6} \right) \tag{15}$$

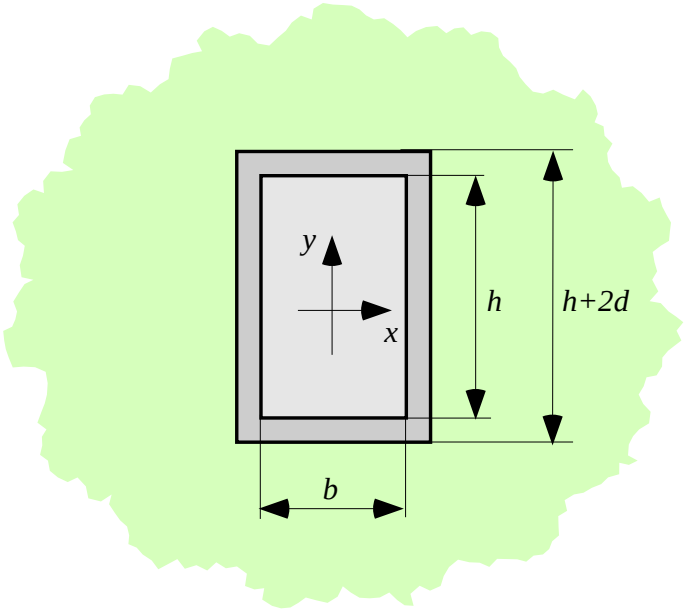

Figure 7: Equivalent rectangular slot shape

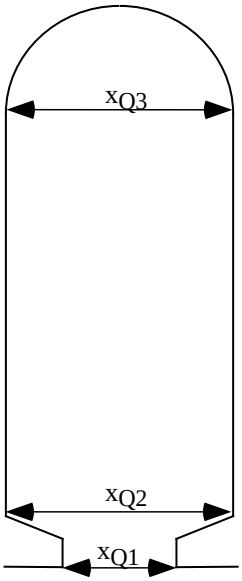

Figure 8: Stator slot geometry

$$R_y = \frac{1}{2}\left(R_{iy} + \frac{R_{y0}}{6}\right) \tag{16}$$

where the slot material contributes with

$$R_{x0} = \frac{b}{h\lambda_Q} \tag{17}$$

$$R_{y0} = \frac{h}{b\lambda_Q} \tag{18}$$

and where the slot insulation and the air film contributes with

$$R_{ix} = \frac{d_I}{h\lambda_I} + \frac{d_A}{h\lambda_A} \tag{19}$$

$$R_{iy} = \frac{d_I}{b\lambda_I} + \frac{d_A}{b\lambda_A} \tag{20}$$

where d_I and d_A are the thermal conductivities of the slot insulation material and the equivalent air film, respectively. Experimental investigations by Kylander resulted in $d_A = 0.30$ mm for a 15 kW IM [1]. Since better information could not be obtained, the same value was used in the model of the PMSM.

Thermal resistance between coil side and end windings

The thermal resistance between the end winding node and the coil side node is a compressed representation of heat flow comprising complex paths. An illustration of the heat flow from the end windings is shown in Fig. 9, where the flow paths are represented by arrows. Dissipated heat from the end winding enters the slot via the conductors. As the end winding reaches the slot, heat starts to flow into the stator iron core and further out to the frame. Heat is also dissipated in the coil sides due to resistive losses, which must be taken into account when the thermal resistance is calculated. Figure 10 shows the lumped-parameter model of one coil, where it is assumed that the temperature distribution is symmetric. The thermal resistance from the mid point on the end winding, to the mid point of the coil side is [8]

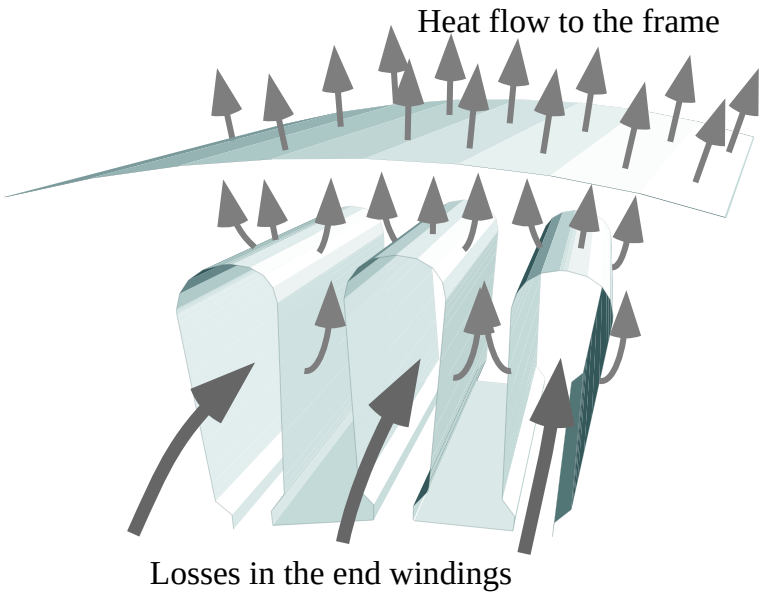

Figure 9: Heat flow from the end windings; the flow path is complex and three-dimensional

$$R_{thw} = \frac{l_{av}}{3A_{Cu}\lambda_{Cu}} \tag{21}$$

where l_{av} is the average conductor length of half a turn. The quantity l_{av} is found by adding the conductor length embedded in the core and the overhang length, which is estimated using the pole pitch and an empirically determined constant, depending on the size of the machine. The average conductor length of half a turn is

$$l_{av} = l_{Fe} + 1.2\tau_p + l' \tag{22}$$

where τ_p is the pole pitch and the quantity l' is equal to 0.05 m, which is valid for small machines [9]. Thermally, the coils are in parallel, as shown in Fig. 11, and the total thermal resistance between the coil side node and the end winding node is

$$R_{th5} = \frac{R_{thw}}{2Q_s} \tag{23}$$

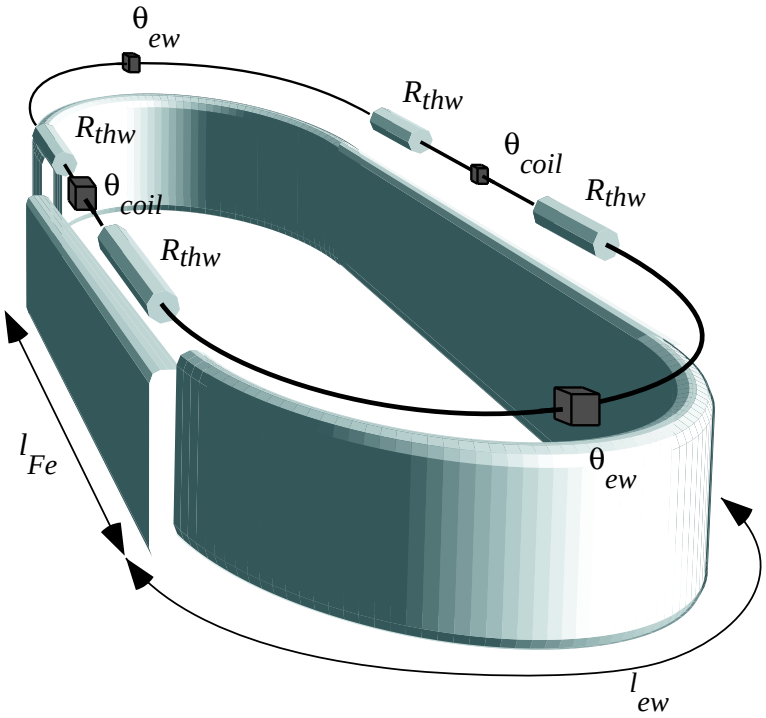

Figure 10: Thermal model of one coil; the left coil side has been cut out

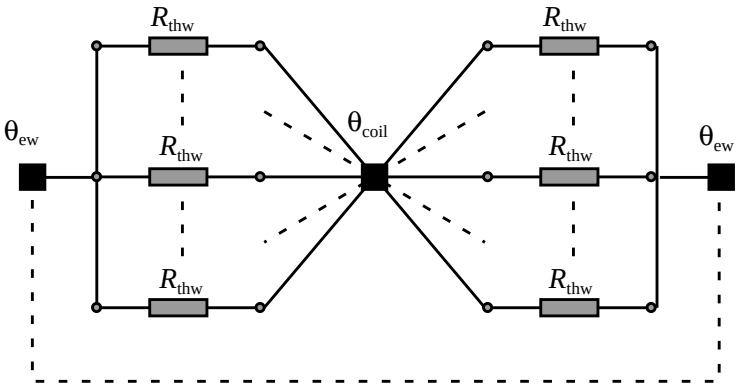

Figure 11: Thermal model of the stator windings

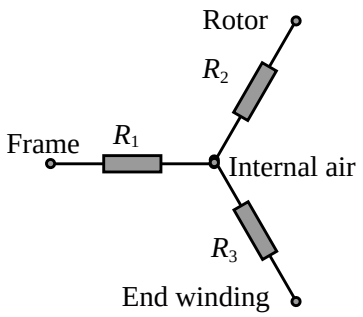

Figure 12: Thermal network of the machine end parts

3.4 Internal Air

Heat transfer in the end regions of the machine involves processes that are very difficult to model due to a complex geometry and encapsulated air in motion. The simplified thermal network representing the end regions of the machine is shown in Fig. 12. The thermal radiation is neglected because of the low temperature difference between the machine parts.

Thermal resistance between internal air and frame

Heat transfer in the end regions is, thus, convective, and the thermal transfer between the machine parts and the internal air are described by Newton's cooling law. The equivalent thermal resistance for heat flow to the frame is expressed as

$$R_1 = \frac{1}{\alpha_1 A_1} \tag{24}$$

where the empirically determined heat transfer coefficient is [1] [2]

$$\alpha_1 = 15 + 6.75^{0.65} + v_r^{0.65} \tag{25}$$

and the area exposed to convection is

$$A_1 = 2A_{es} + A_{if} \tag{26}$$

The rotor peripheral velocity is denoted by v_r, A_{es} is the internal end shield area and A_{if} is the internal frame area. The empirical investigation determining the expressions was made with a machine of similar size to the PMSM.

Thermal resistance between internal air and rotor

Newton's cooling law also describes the equivalent thermal resistance for heat flow from the rotor to the air by the expression

$$R_2 = \frac{1}{\alpha_2 A_2} \tag{27}$$

where the empirically determined heat transfer coefficient is [1] [2]

$$\alpha_2 = 16.5^{0.65} v_r^{0.65} \tag{28}$$

and the area exposed to convection is

$$A_2 = 2 b_{fin} h_{fin} n_{fin} + \pi r_\delta^2 \tag{29}$$

where b_{fin} and h_{fin} are the width and height of the rotor fins, n_{fin} is the number of fins and r_δ is the air gap radius. The machine used in Kylander's experiments is a standard TEFC induction motor that is constructed with rotor end plates shaped as a radial fan. In the experimental PMSM, this is not the case and R_2 in Equation (27) should be evaluated by other means. Since the axial heat flow in the rotor core was neglected, the amount of heat transferred from the rotor end plates to the internal air depends on the heat conduction through the shaft and the end plates. It was assumed that the heat flow to the end plates was small and that the influence on the final result was negligible if R_2 was treated as large.

Thermal resistance between internal air and end windings

In general, it is an intricate task to model convective heat flow from the end windings and it requires good knowledge of the system in question, usually achieved through experiments. Heat flow from the end windings to the internal air is calculated using an expression for the end winding surface area

$$A_{ew} = \pi l_{ov} \frac{d_1 + d_2}{2} \tag{30}$$

where d_1 and d_2 are the outer and inner diameters of the end winding wreath, respectively, the average conductor length of the end windings is

$$l_{ov} = l_{av} - l_{Fe} \tag{31}$$

The equivalent thermal resistance for heat flow from the end windings is

$$R_3 = \frac{1}{\alpha_3 A_3} \tag{32}$$

where $A_3 = A_{ew}$ and the empirically determined heat transfer coefficient is [1] [2]

$$\alpha_2 = 6.5 + 5.25^{0.65} v_r^{0.6} \tag{33}$$

The temperature of the internal air is not in itself important. For convenience, a wye-delta ($Y - \Delta$) transformation was made, yielding a simplified thermal network, as shown in Fig. 13.

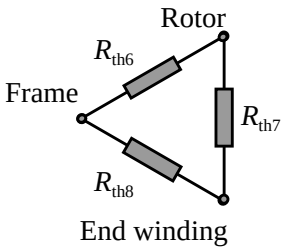

Figure 13: A simplified thermal model of heat transfer via the internal air

3.5 Air Gap

Across the air gap, heat transfer occurs as conduction, convection and radiation. The radiating portion of the heat flow is neglected because of a relatively small temperature difference between the rotor and the stator surfaces. The convective heat transfer depends on the nature of the airflow in the air gap. The influence on air gap convection is determined by two main quantities: the ruggedness of the rotor and stator surfaces and the peripheral speed of the rotor surface. By assuming smooth surfaces, the critical transition between laminar and turbulent flow is characterized by the modified Taylor number [1] [3]

$$(Ta)_m = \frac{\Omega_m^2 r_\delta \delta^3}{\nu_A^2} \tag{34}$$

where Ω_m is the mechanical angular speed of the rotor, r_δ is the air gap radius, δ is the air gap length and ν_A is the kinematic viscosity of the air. According to Becker and Kaye, the critical magnitude of $(Ta)_m$ is 1740 and if $(Ta)_m$ is less than 1740, the airflow is regarded as laminar and the Nusselt number, Nu, is equal to

2. When the critical magnitude is exceeded, the Nusselt number is given by the empirically derived expression [10]

$$Nu = 0.409(Ta)_m^{0.241} - 137(Ta)_m^{-0.75} \tag{35}$$

Axial airflow is not included since the machine is small and the influence is negligible [3]. The heat transfer coefficient for the air gap includes both conduction and convection and is given by [1]

$$\alpha_\delta = \frac{Nu\lambda_A}{2\delta} \tag{36}$$

The thermal resistance of the air gap between rotor and stator is

$$R_{th\delta} = \frac{1}{\alpha_\delta 2\pi r_\delta l_{Fe}} \tag{37}$$

which is a temperature dependent quantity, since both ν_A and λ_A vary with the temperature. The variations were taken into account by evaluating the temperature dependent quantities using the calculated average temperature in the air gap. Furthermore, the air gap length variation due to the rotor and stator thermal expansion was accounted for using the calculated rotor and stator temperatures.

3.6 Rotor

Temperature dependent properties of the permanent magnet material emphasize the importance of accurate calculations of the magnet temperature. At increased temperature, the minimal flux density allowed for an unchanged recoil line increases. Permanent demagnetization of the material is possible if the temperature rises above a certain level.

Both the eddy-current losses in the permanent magnets and the iron losses in the rotor core have been assigned to the magnet node. As the rotor iron losses are very small and a worst case approach was adopted, this was considered a good way to simplify the model.

The rotor cross-sectional geometry is shown in Fig. 14. Axial heat flow in the rotor core was neglected, as well as heat transfer through the protruding iron parts of the rotor core. Another simplification was introduced by assuming that the shaft cross-section has a homogeneous temperature distribution, which was regarded a good approximation since the contact resistance between the shaft and the core is an uncertain quantity. The contact resistance probably has a larger influence on the final solution than the temperature distribution in the shaft.

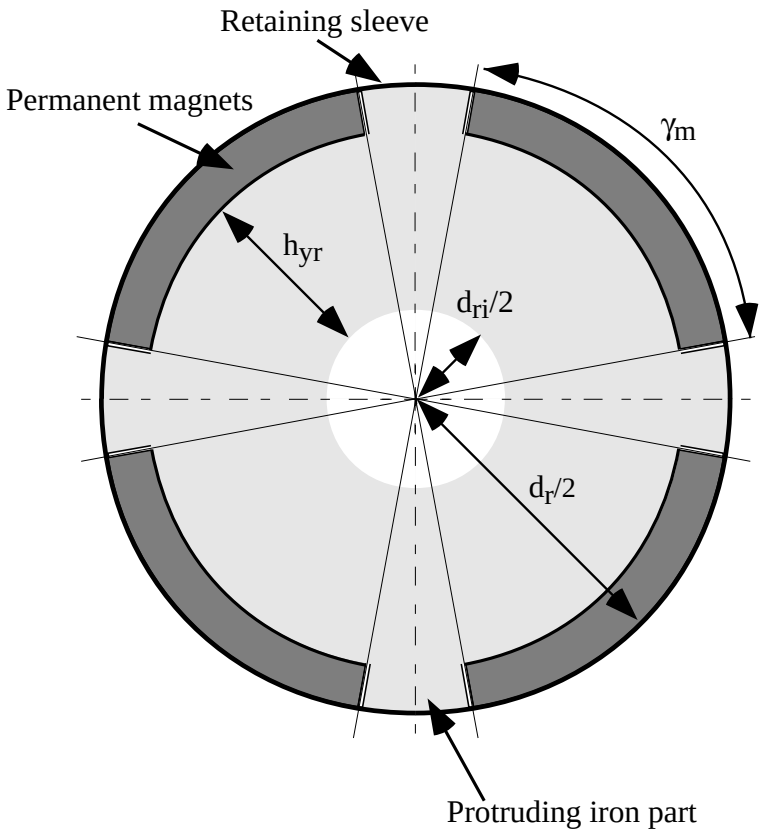

Figure 14: Rotor geometry

The radial rotor yoke thermal resistance is calculated in analogy with the stator yoke. It is expressed as

$$R_{thyr} = \frac{\ln\left(\frac{d_{ri}}{2} + h_{yr}\right) - \ln\left(\frac{d_{ri}}{2}\right)}{2\pi l_u \lambda_{Fe}} \tag{38}$$

where d_{ri} is the shaft diameter and h_{yr} is the height of the rotor yoke.

In the experimental motor, the permanent magnets are divided into rectangular shaped blocks, electrically and thermally insulated from each other and from the rotor core. The permanent magnets are modeled as a cylindrical layer of permanent-magnet material, in which axial and circumferential heat flow is not present. The thermal resistance of the permanent magnets is found from

$$R_{thpm} = \frac{\ln\left(\frac{d_{ri}}{2} + h_{yr} + h_{pm}\right) - \ln\left(\frac{d_{ri}}{2} + h_{yr}\right)}{2\pi l_{Fe} \lambda_{pm}} \frac{2\pi}{2p\gamma_m} \tag{39}$$

where $h_{pm}$is the height of the permanent magnets, λ_{pm} is the thermal conductivity of the permanent magnets and γ_m is the angle occupied by magnets in one pole pitch.

Because of the small thickness of the retaining sleeve compared with the radius, the radial thermal resistance of the retaining sleeve is

$$R_{thsl} = \frac{h_{sl}}{\pi d_r l_{Fe} \lambda_{sl}} \frac{2\pi}{2p\gamma_m} \tag{40}$$

where h_{sl} is the sleeve thickness, λ_{sl} is the thermal conductivity of the sleeve and d_r is the outer diameter of the rotor.

The insulation between the magnets and the rotor yoke has a thermal resistance expressed by

$$R_{thins} = \frac{d_{Ir}}{\pi(d_{ri} + 2h_{yr}) l_{Fe} \lambda_{Ir}} \frac{2\pi}{2p\gamma_m} \tag{41}$$

where d_{Ir} is the insulation thickness and λ_{Ir} is the thermal conductivity of the insulation material.

Thermal resistance between stator and rotor

In the thermal network, R_{th9} represents the thermal resistance between the stator teeth node, placed in the middle of the teeth, and the permanent magnet node, placed in the middle of the permanent magnets. It is expressed as

$$R_{th9} = R_{th\delta} + \frac{1}{2}R_{thd} + R_{thsl} + \frac{1}{2}R_{thpm} \tag{42}$$

3.7 Shaft

Heat flow in the axial direction in the rotor construction is assumed to be present in the shaft only. A further simplification is that the temperature distribution in a shaft cross-section is regarded as homogeneous. The axial thermal resistance of the shaft, between the bearings, is, thus, expressed as

$$R_{thsh} = \frac{l_{bb}}{\pi \left(\frac{d_{ri}}{2}\right)^2 \lambda_{sh}} \tag{43}$$

where l_{bb} is the axial distance between the bearings and λ_{sh} is the heat conductivity of the shaft material.

3.8 Bearings

Heat transfer through a ball bearing is mainly provided through contact between the balls and the inner and outer rails. If the conductivity of sealing and grease is neglected, the physical dimension of the bearing and the rotational speed will determine the thermal resistance. Internally generated losses due to friction are assumed to appear in the balls and, therefore, assigned the ball node, as shown in Fig. 15. An expression for the thermal resistance of one bearing is given by

$$R_{thb} = k_1(0.12 - k_2 d_b)(33 - k_3 \Omega_m d_b) \tag{44}$$

where the average diameter of the bearing is denoted by d_b, Ω_m is the mechanical angular frequency and

- k_1=0.45 K/W
- k_2=1 m^{-1}
- k_3=1 s/m

are empirically determined constants [1] [2]. The constants are valid for dimensions and rotational speeds similar to those used in Kylander's experiments. Equation (44) cannot be applied directly because of the higher rotational speed of the PMSM. For simplicity, the speed dependence of the thermal resistance of the bearing was neglected. The worst case approach supports the neglected speed dependence.

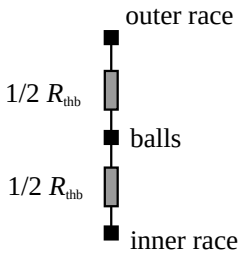

Figure 15: Thermal model of a bearing.

The bearing losses were calculated from the linear approximation

$$P_b = P_{b,max} \frac{\Omega_m}{\Omega_{m,max}} \tag{45}$$

where $P_{b,max}$ is the total bearing losses at maximum speed $\Omega_{m,max}$. The maximum losses were estimated to be 60 W at the maximum speed 12000 rpm [5] [11].

Thermal resistance between bearings and frame

Symmetry in the thermal model implies that an equal portion of heat flows through the two bearings and the thermal resistance between the bearing node and the frame node is thus

$$R_{th11} = \frac{1}{4} R_{thb} \tag{46}$$

Thermal resistance between magnets and bearings

The conductive heat transfer from the magnets to the shaft is similar to the case with heat transfer from the stator yoke to the frame. A contact resistance is present at the interface between the rotor core and the shaft, which is difficult to predict accurately. As with the contact resistance between the stator yoke and the frame, previously presented results from empirical investigations of similar machines have been used. The proposed value for the thermal contact resistance

between the rotor core and the shaft, R_{thcr}, is equal to the thermal resistance of the rotor core.

The expression for the thermal resistance between the rotor node and the bearing node is the sum of the contributions from the magnets, the magnet insulation, the rotor core, the contact resistance, the shaft and the bearings.

$$R_{th10} = \frac{1}{2}R_{thpm} + R_{thins} + R_{thyr} + R_{thcr} + \frac{1}{2}R_{thsh} + \frac{1}{4}R_{thb} \tag{47}$$

4 Steady-State Analysis

In general, a thermal network with $n+1$ nodes is represented by n coupled algebraic equations. The temperature rise in the nodes relative to a reference temperature are found from

$$\Theta = \mathbf{G}^{-1}\mathbf{P} \tag{48}$$

where $\mathbf{P}$ is the loss vector, containing the dissipated losses assigned to each node

$$\mathbf{P} = \begin{bmatrix} P_1 \\ P_2 \\ \vdots \\ P_n \end{bmatrix} \tag{49}$$

and Θ is the temperature rise vector

$$\Theta = \begin{bmatrix} \theta_1 \\ \theta_2 \\ \vdots \\ \theta_n \end{bmatrix} \tag{50}$$

The thermal resistances of the model are used to form a thermal conductance matrix, $\mathbf{G}$, which is defined as

$$\mathbf{G} = \begin{bmatrix} \sum_{i=1}^{n} \frac{1}{R_{1,i}} & -\frac{1}{R_{1,2}} & \cdots & -\frac{1}{R_{1,n}} \\ -\frac{1}{R_{2,1}} & \sum_{i=1}^{n} \frac{1}{R_{1,i}} & \cdots & -\frac{1}{R_{2,n}} \\ \vdots & \vdots & \ddots & \vdots \\ -\frac{1}{R_{n,1}} & -\frac{1}{R_{n,2}} & \cdots & \sum_{i=1}^{n} \frac{1}{R_{n,i}} \end{bmatrix} \tag{51}$$

Temperature dependent elements in $\mathbf{G}$ and $\mathbf{P}$ require an iterative solution where the matrix must be updated regularly. In the simulations, R_{th9} was implemented as a temperature dependent element. Table 5 shows the resulting thermal resistances.

Table 5: Thermal Resistances of the Model

Thermal resistance	Value (K/W)
R_{th1}	0.0002
R_{th2}	0.0064
R_{th3}	0.0085
R_{th4}	0.0056
R_{th5}	0.0747
R_{th6}	0.4350
R_{th7}	1.5489
R_{th8}	0.2242
R_{th9}	0.1811
R_{th10}	2.8640
R_{th11}	0.3119

4.1 Temperature Measurements

Laboratory tests were made with the experimental PMSM for validation of the design. For this purpose, an experimental set-up was made, which included equipment for measurements of various temperatures. Calorimetric loss measurements were made by measuring the inlet and outlet cooling water temperatures with individually calibrated platinum resistance temperature detectors (Pt-100) [12].

Temperature monitoring of the machine was made by thermocouples mounted in the PMSM, according to Fig. 16. There were nine sensors installed; three at the bottom of stator slots, three at the top of stator slots and three in the end windings. A data acquisition unit was used to collect the signals from all the temperature sensors, with measurement accuracies presented in Table 6.

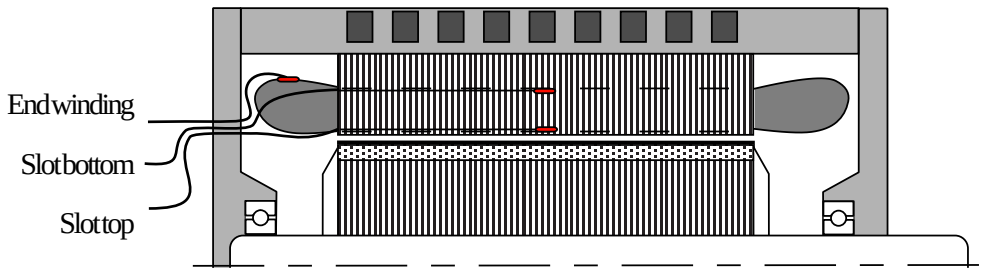

Figure 16: Placement of the thermocouple sensors

Table 6: Temperature measurement accuracy

Temperature sensor	Accuracy
Pt-100 with 4-wire connection	±0.21°C
Thermocouple type K	±0.42°C

4.2 Comparison of Calculated and Measured Temperatures

In this section, the calculated steady-state temperatures are compared with measurements made with the experimental motor. The operating point chosen for the comparison is 80 Nm at 6000 rpm, which is the nominal operating point of the motor, corresponding to 50 kW output power. Table 7 presents the data used in the calculation. The total losses were measured with a calorimetric method and a loss separation was made according to calculations made with a finite-element method [5]. The calculated temperatures are shown in Fig. 17

Table 7: Separated losses from measurements, used for the comparison

Terminal current	170 A
Shaft power	49 kW
Supply frequency	201 Hz
Rotational speed	6021 rpm
Resistive losses	1335 W
Coil sides	822 W
End windings	513 W
Stator core losses	851 W
Yoke	464 W
Teeth	387 W
Rotor losses	22 W
Friction losses	90 W
Total losses	2298 W

The comparison of measured and simulated temperatures was made in three nodes determined by the probe configuration of the experimental motor. As shown in Table 8, the deviation is small, which implies that the model works well, at least for predicting the temperature in the end windings and coil sides. The difference of 4 °C in temperature rise corresponds to an error of approximately 11 %.

4.3 Sensitivity Analysis

An investigation of the system sensitivity was conducted by a simple iterative method. The steady-state solution was compared with each thermal resistance

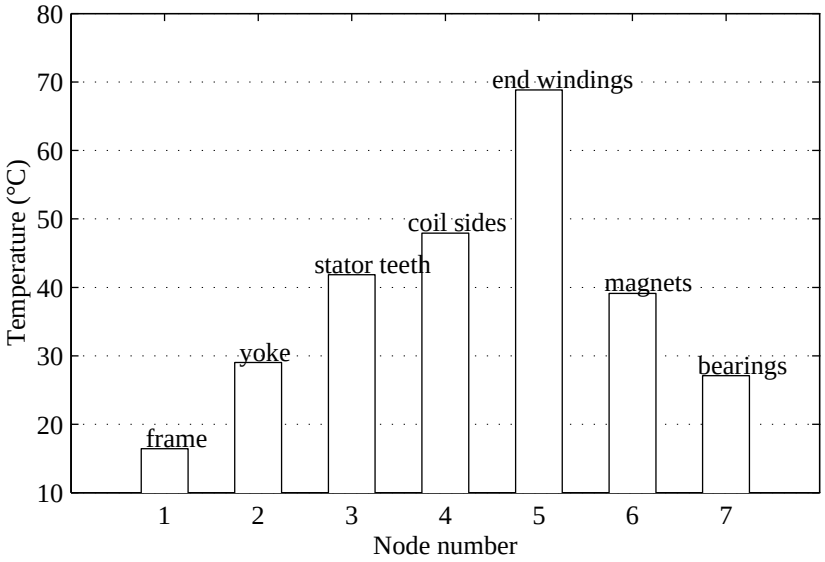

Figure 17: Calculated temperatures at 50 kW, 6000 rpm and 16°C inlet temperature

Table 8: Measured and calculated temperatures at nominal speed and load

Node	Measured (°C)	Calculated (°C)
End windings	72	68
Coil sides	51	47
Cooling water	16	16

doubled and reduced by half. The results of the sensitivity analysis are presented in Table 9. The following observations can be made:

- The absolute change in temperature rise when R_{th1} changes is small, which implies that its significance is of minor order.
- A variation in R_{th2} alters the temperature rises in all nodes except the frame node. The change of the temperature rises are, in some cases, large and the importance of accurate modeling cannot be foreseen. Therefore, a special investigation should be focused on the contact resistance between the stator core and the frame since this is especially difficult to calculate.
- The end winding temperature is of great importance since it is the part in the machine which reaches the highest temperature. As shown in Table 9, R_{th3}, R_{th4} and R_{th5} affect the predicted end winding temperature significantly. Focusing on regions with high temperature gradients is especially important here. In this case, the slot insulation and air pockets around the stator windings should be brought to attention.
- The largest impact on the magnet temperature, θ_6, is imposed by R_{th3} and R_{th6}. The thermal resistance across the air gap, included in R_{th9}, does not influence the magnet temperature very much. One reason is that the rotor losses are small and the temperature in the stator teeth is higher than in the magnets. The magnets are, thus, not cooled through the stator but, instead, through the shaft and bearings.

Table 9: Temperature rises (K) at 6000 rpm 50 kW

Change	Frame	Yoke	Teeth	Coil sides	End windings	Magnets	Bearings
None	0.4	13.0	26.5	33.7	59.4	23.9	8.4
R_{th1} double	0.9	13.5	26.9	34.2	59.9	24.3	8.8
R_{th1} half	0.2	12.8	26.3	33.5	59.2	23.7	8.1
R_{th2} double	0.4	17.0	30.4	37.5	62.3	26.5	8.6
R_{th2} half	0.4	11.0	24.5	31.8	58.0	22.6	8.2
R_{th3} double	0.4	12.6	38.6	45.6	68.3	32.0	9.2
R_{th3} half	0.4	13.2	20.1	27.5	54.7	19.5	7.9
R_{th4} double	0.4	12.9	26.2	40.4	64.3	24.0	8.4
R_{th4} half	0.4	13.1	26.7	30.3	57.0	23.8	8.4
R_{th5} double	0.4	12.6	25.6	32.4	73.3	24.3	8.4
R_{th5} half	0.4	13.3	27.2	34.7	49.4	23.6	8.3
R_{th6} double	0.4	13.1	26.8	34.0	59.8	27.7	8.7
R_{th6} half	0.4	12.8	26.1	33.3	59.0	18.8	7.9
R_{th7} double	0.4	13.0	26.5	37.8	60.1	22.6	8.2
R_{th7} half	0.4	13.0	26.5	33.6	58.3	26.2	8.6
R_{th8} double	0.4	13.7	28.1	35.9	69.4	25.6	8.5
R_{th8} half	0.4	12.1	24.4	30.9	46.3	21.6	8.1
R_{th9} double	0.4	13.0	26.5	33.7	59.4	23.9	8.4
R_{th9} half	0.4	13.0	26.5	33.7	59.4	23.9	8.4
R_{th10} double	0.4	13.0	26.5	33.8	59.5	24.2	7.6
R_{th10} half	0.4	13.0	26.5	33.7	59.4	23.4	9.7
R_{th11} double	0.4	13.0	26.5	33.8	59.5	24.2	14.8
R_{th11} half	0.4	13.0	26.5	33.7	59.4	23.7	4.7

5 Transient Analysis

In time dependent problems, a representation for the stored thermal energy in the system is introduced as thermal capacitances [1]. Each node is assigned a thermal capacitance from the node to the ambient. The thermal capacitance of an element is derived from geometrical and material data. An element consisting of several parts has the thermal capacity

$$C_{th} = \sum_{i=1}^{n} m_i c_i \tag{52}$$

where m_i is the mass of part i, and c_i is the specific heat capacity of part i. The equation system requires a thermal capacitance matrix, which is defined as

$$\mathbf{C} = \begin{bmatrix} C_{th1} & 0 & \dots & 0 \\ 0 & C_{th2} & \dots & 0 \\ \vdots & \vdots & \ddots & \vdots \\ 0 & 0 & \dots & C_{thn} \end{bmatrix} \tag{53}$$

The thermal network with $n+1$ nodes is represented in transient state by n first-order coupled differential equations. The temperature rises relative to a reference temperature, θ_0, are found by solving

$$\frac{d}{dt}(\Theta) = \mathbf{C}^{-1}(\mathbf{P} - \mathbf{G}\Theta) \tag{54}$$

5.1 Transient Simulation

Simulations of the transient-state temperature distribution were made using initial conditions from a calculated thermal steady-state at nominal output power. A step to maximum output power was applied and the transient temperatures were solved.

The predicted losses have been calculated using a time-stepping finite element method where the electric circuit equations are solved simultaneously with the magnetic field [13] [14]. From experience, it is known that the losses will be larger in reality. Compensation for additional losses was made by increasing the iron losses by 50% and the rotor losses by 100%, as a worst-case approach in the optimization procedure.

Preliminary results have shown that the optimized motor design fulfilled the thermal requirements (see Section 2.1). The simulations were based on results from loss calculations made by means of a finite element method [13] [5]. The method is approximate, and additional losses were expected due to simplifications made in the loss model. Thermal margins for the winding temperatures were chosen with respect to the unknown loss components of the calculations, which implies that the maximum winding temperature specified is low compared with a practical case.

Results from preliminary measurements of the experimental motor were used for a loss separation to predict the thermal characteristics of the motor construction. Examples of simulated results made with the rotational speed kept constant are shown in Figs. 18 and 19. The end winding temperatures will apparently exceed the specified maximum winding temperature, which implies that the time limit for intermittent operation should be changed.

The differences between the previously predicted temperature distribution and the result presented here is a higher winding resistance than expected. Skin effect and proximity effects in the stator windings are a major source of the increase in winding losses. Measurements of the experimental motor have shown that the winding resistance increases by approximately 84 % at 200 Hz and 172 % at 400 Hz, compared with the dc-resistance [5]. Furthermore, the temperature dependence of the winding resistance also contributes to the differences in the winding losses.

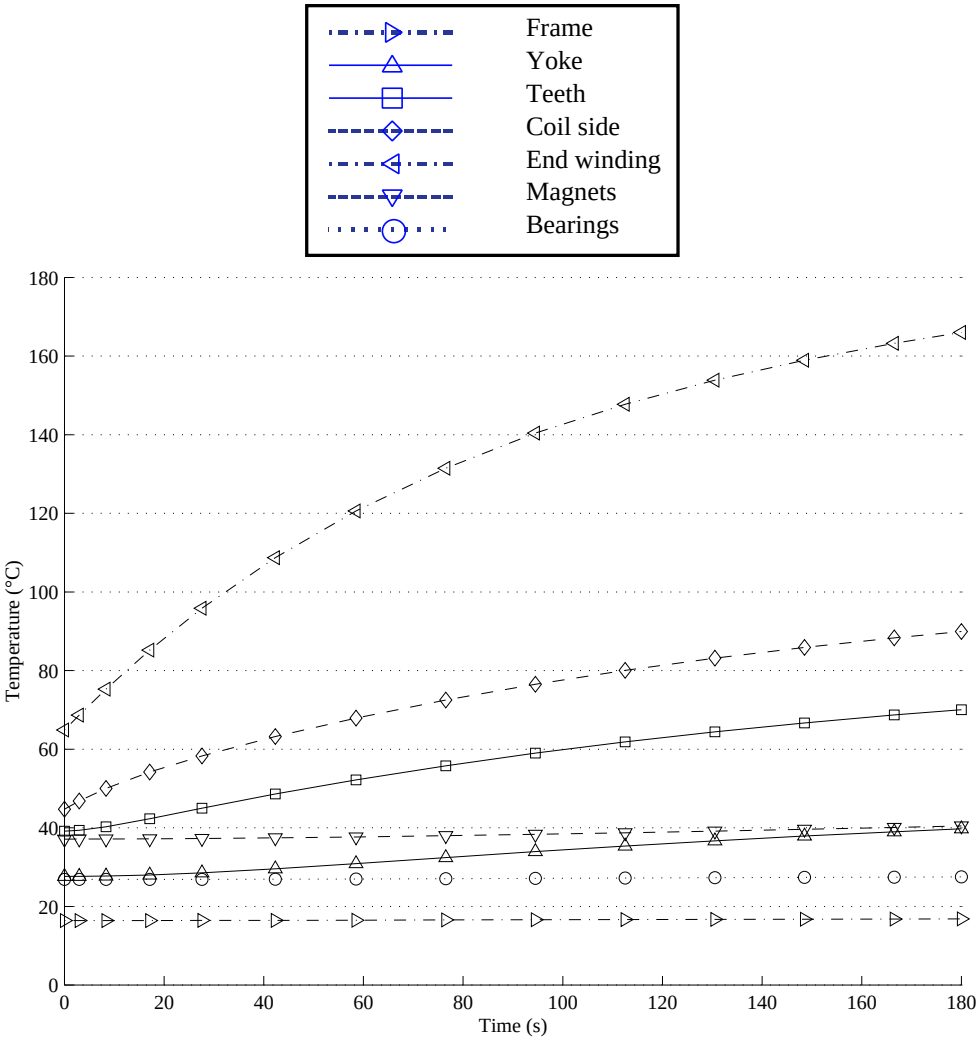

Figure 18: Transient temperatures due to a load step from 50 kW to 100 kW at 6000 rpm. The assumed average cooling water temperature is 16°C

According to the presented results, a winding able to withstand a higher temperature would be suitable as well as a reduction of the frequency dependence of the windings. The latter could possibly be achieved by the use of litz-wire.

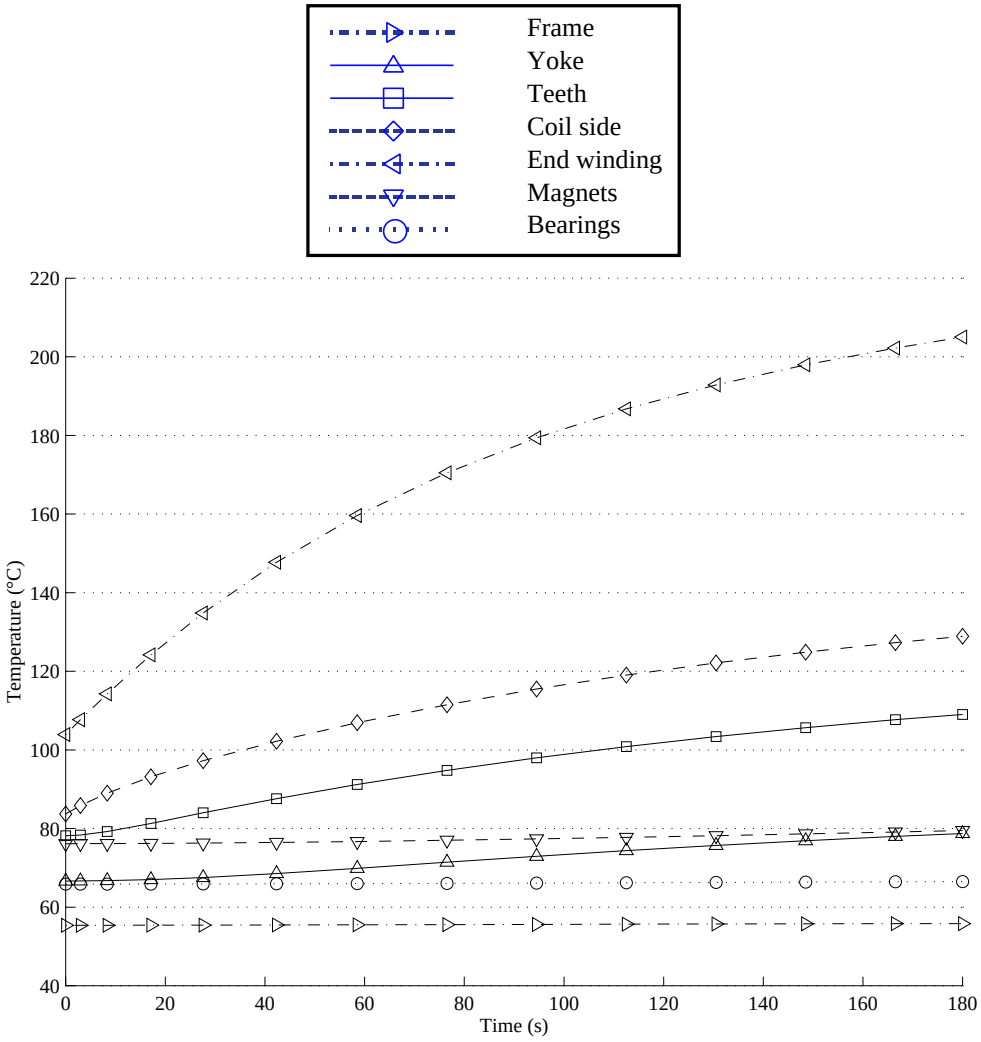

Figure 19: Transient temperatures due to a load step from 50 kW to 100 kW at 6000 rpm. The assumed average cooling water temperature is 55°C

6 Conclusion

A thermal model has been developed for the design and optimization procedure of a permanent-magnet motor for a hybrid electric vehicle application. The model is a thermal network with lumped parameters represented by equivalent thermal resistances and equivalent thermal capacitances. Steady-state calculations and transient simulations with the thermal network were made using a constant reference temperature. Special focus was put on the temperatures of the permanent magnets and the end windings.

A sensitivity analysis of the model resulted in deviations of the temperature rise less than ± 12 K, when the thermal resistances were altered between +100 % and -50 % of the nominal value.

Temperature measurements in steady-state operation of the full-scale experimental motor were compared with the numerically computed results of the thermal model. The maximum difference between calculated and measured temperature rises was 4 K, corresponding to a relative error of approximately 11 %.

Regions of the machine which are associated with temperature gradients of a high magnitude are of special importance in the modeling. Results from the investigation point out that the following components should be brought to attention:

- The contact thermal resistance between stator yoke and frame
- The contact thermal resistance between rotor yoke and shaft
- The thermal resistance of the slot insulation and air pockets
- The thermal properties of the end windings

In comparison with the predicted loss distribution, a significant increase in the winding losses was observed at high frequencies. Skin effect and proximity effects are the two phenomena likely to be the cause of the increase. Thermally, the consequence is an increased winding temperature exceeding the specified maximum temperature in transient state when the maximum intermittent output power is applied as a step function.

References

[1] G. Kylander, *Thermal Modelling of Small Cage Induction Motors*, Ph.D. thesis, School of Electrical and Computer Engineering, Chalmers University of Technology, Göteborg, Sweden, February 1995, Technical Report No.265.

[2] G. Kylander, "Modellering och mätning av temperatur och förluster i mindre asynkronmaskiner," Licentiate thesis, Chalmers University of Technology, Göteborg, Sweden,, May 1993, Technical Report No.147L.

[3] J. Saari, *Thermal Analysis of High-Speed Induction Machines*, Ph.D. thesis, Laboratory of Electromechanics, Helsinki University of Technology, Otaniemi, Finland, 1998, Acta Polytechnica Scandinavica, Electrical Engineering Series No.90.

[4] J. Saari and M. Kaltenbacher, "An asymmetric thermal model for totally enclosed fan-cooled motors," Tech. Rep. 38, Laboratory of Electromechanics, Helsinki University of Technology, Espoo, Finland, 1992.

[5] J. Hellsing, "Design and optimization of a permanent magnet motor for a hybrid electric vehicle," Licentiate thesis, School of Electrical and Computer Engineering, Chalmers University of Technology, Göteborg, Sweden, March 1998, Tecnical Report No.282L.

[6] M. Nurdin, M. Poloujadoff, and A. Faure, "Synthesis of squirrel cage motors: A key to optimization," *IEEE Transactions on Energy Conversion*, vol. 6, no. 2, pp. 327–333, June 1991.

[7] G.R. Slemon and X. Liu, "Modeling and design optimization of permanent magnet motors," *Electric Machines and Power Systems*, vol. 20, no. 2, pp. 71–92, March 1992.

[8] V. Kotrba, "Cooling and ventilation of electrical machines," Laboratory of Electromechanics, Helsinki University of Technology, Espoo, Finland, 1993, Postgraduate seminar on electromechanics (S-17.202).

[9] J. Luomi, "Magnetic field calculations and electrical machines," Department of Electrical Machines and Power Electronics, Chalmers University of Technology, Göteborg, Sweden, 1994, Lecture notes for a course in electrical machines.

[10] K.M. Becker and J. Kaye, "Measurements of diabatic flow in an annulus with an inner rotating cylinder," *Journal of Heat Transfer*, , no. 84, pp. 97–105, 1962.

[11] SKF, "Huvudkatalog," 1994, Katalog4000/II S.

[12] T. Larsson, "Calorimetric measurement of losses of a permanent magnet synchronous motor," M.Sc.thesis, Department of Electric Power Engineering, Chalmers University of Technology, Göteborg, Sweden,, June 1998, Report No.27E.

[13] J. Luomi, J. Lindström, and J. Hellsing, "Design and analysis of electrical motors for a hybrid electric vehicle," in *IEEE/Stockholm Power Tech Conference Proceedings*, Stockholm, Sweden, June 18-22 1995, vol. Electrical Machines and Drives, pp. 274–279.

[14] A. Arkkio and A. Niemenmaa, "Estimation of losses in cage induction motors using finite element techniques," in *Proceedings of the International Conference on Electrical Machines*, Manchester, U.K, September 15-17 1992, vol. 2, pp. 317–321.

An Experimental Permanent-Magnet Motor Drive – System Description and Preliminary Measurements

Joachim Lindström

Department of Electric Power Engineering
Chalmers University of Technology
Göteborg, Sweden

April, 1999

Abstract

The report describes a drive system built for experimental use in a laboratory. An experimental permanent-magnet motor of the inset-magnet design, optimized for a hybrid electric vehicle was the test object. A power electronic converter with a digital control system was built for the drive system. Results from preliminary experiments with the drive system are presented and a discussion is given. The predicted induced emf corresponds well to the expected performance, which indicates that the calculated flux linkage agrees well with the real one. In addition, the predicted torque characteristics agree well with the ones experienced in the laboratory. A control method suitable for the motor design was implemented for the experimental drive. Motor operation tests in the constant torque region show that the commonly used current minimization strategy works well. The total losses of the motor were measured with a calorimetric method for improved accuracy. Estimation of the accuracy has shown that the total losses can be determined within $\pm 2.3\%$ of the measured losses at the nominal operating point, where the motor efficiency was 95.5%. Further investigation associated with the control aspects is required in order to validate the experimental motor to its full extent.

Contents

List of Symbols

Latin		**Greek**	
c	specific heat capacity	γ	angle
i	current	η	efficiency
$\underline{i}$	current vector	ω	angular frequency
K	gain	ψ	flux linkage
L	inductance	ρ	density
P	power	θ	temperature
p	pole-pair number	**Subscripts**	
R	resistance	a	armature
T	torque	b	base
u	voltage	dc	direct current
q	flow	d	d-axis
		d	dissipated
		e	electrodynamic
		i	integral
		i	internal
		m	magnet
		p	proportional
		q	q-axis
		s	stator
		v	volumetric

1 Introduction

The progress in energy storage technology and increasing demands for energy efficient systems have enhanced the potentiality to produce competitive vehicle solutions with low emissions. Electric vehicles (EV) and hybrid electric vehicles (HEV) are possible alternatives for personal transportation in a more environmental friendly future society.

Development of an electric drive for an HEV requires methods for design and analysis that are different from the traditional ones. The HEV drive operates in a wide range of speeds and loads, which must be accounted for in the design procedure. In order to obtain a long driving range with the HEV in a pure-electric mode, the overall efficiency of the drive system must be high over the whole operating range. For a correct analysis, the losses of all components in the drive line should be taken into account and validation should be made according to the conditions encountered in a vehicle application.

An experimental motor for an HEV was developed as a part of a research project at the department. The motor is a permanent-magnet synchronous motor (PMSM) of the inset-magnet type. Optimization and design of the motor was based on calculations made with a finite-element method and driving-cycle simulations [1] [2] [3].

This report describes the laboratory set-up built for the experimental investigation of the drive system. Short descriptions are given of the electrical motor and the power electronic converter with the included control system. An introduction to the theoretical aspects concerning drive limitations and interaction with the control is also included.

A calorimetric method was chosen for the measurements of the total losses in order to improve the accuracy [4]. Preliminary results from the laboratory tests are presented and compared with the originally calculated performance. A discussion of the preliminary results and possible sources of errors is given.

2 The Experimental Motor

A PMSM with an inset-magnet rotor design was chosen for the HEV. The geometry of the motor is illustrated in Fig.1. The rotor topology offers effective utilization of the permanent magnets, and can be designed for good flux-weakening properties. The constant power speed ratio (CPSR) was chosen to be 2:1 in this application, which was considered a suitable compromise between motor size and transmission complexity [1].

The iron core is made of laminations of thin, high-grade electrical sheets and the NdFeB permanent magnets are made of electrically insulated pieces in order to reduce the eddy-current losses. A 0.75 mm thick pre-tensed carbon-fiber composite cylinder is mounted around the rotor to ensure sufficient mechanical strength of the rotor construction at the maximum speed. The advantage of using carbon fiber is that it has high mechanical strength, high stiffness and low electrical conductivity. A compact motor design is achieved by using water cooling of the stator frame. The motor data obtained from the optimization procedure is given in Table 1 and a complete description of the motor has been published by Hellsing [3]. In Fig.2, a picture of the experimental motor is shown. The view is from the drive end with the end shield removed. The permanent magnets and the carbon fiber retaining cylinder are visible.

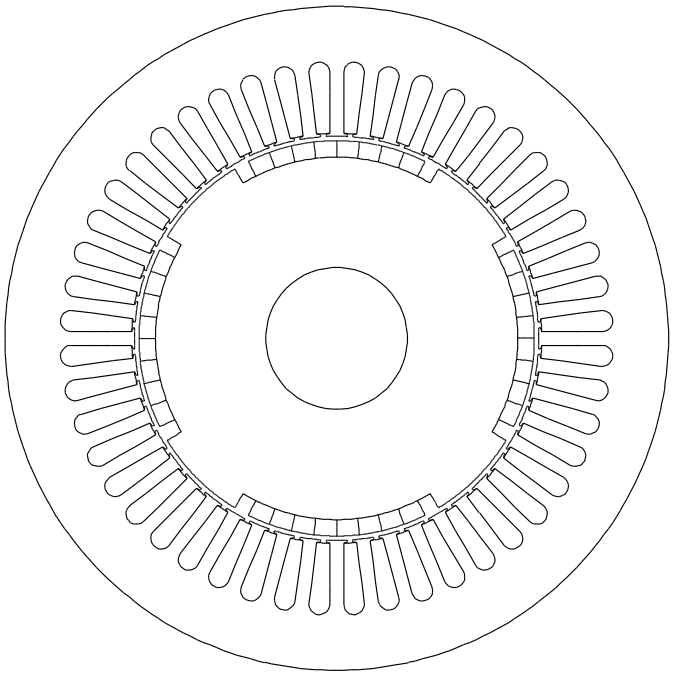

Figure 1: Cross-sectional geometry of the inset-magnet motor

Table 1: Motor data

Stator outer diameter	186 mm
Stator inner diameter	110 mm
Stack length	220 mm
Overall mass	62 kg
Mass of active parts	37 kg
Mass of NdFeB permanent magnets	1.7 kg
Open-circuit voltage	0.79 p.u.
Direct-axis synchronous reactance	0.34 p.u.
Quadrature-axis synchronous reactance	0.80 p.u.
Nominal predicted efficiency	97%
Nominal speed (base speed)	6000 rpm
Maximum speed	12000 rpm
Maximum continuous output power	50 kW
Maximum intermittent output power	100 kW
Rated current (50 kW, 6000 rpm)	160 A
Rated voltage (1 p.u.)	220 V

Figure 2: A view from the drive end of the experimental motor

3 The Voltage Source Converter

A voltage source converter (VSC) was designed and constructed for the experiments. The converter is equipped with intelligent, integrated power modules (IPM) based on IGBT-technology and is designed to meet the demands on an electric vehicle drive. Examples of such requirements are: robust mechanical construction, low weight and small volume. Water-cooling was regarded a good solution for achieving these requirements and, further, a compact dc-link circuit with low stray-inductance was implemented. A picture of the converter in laboratory environment is shown in Fig.3.

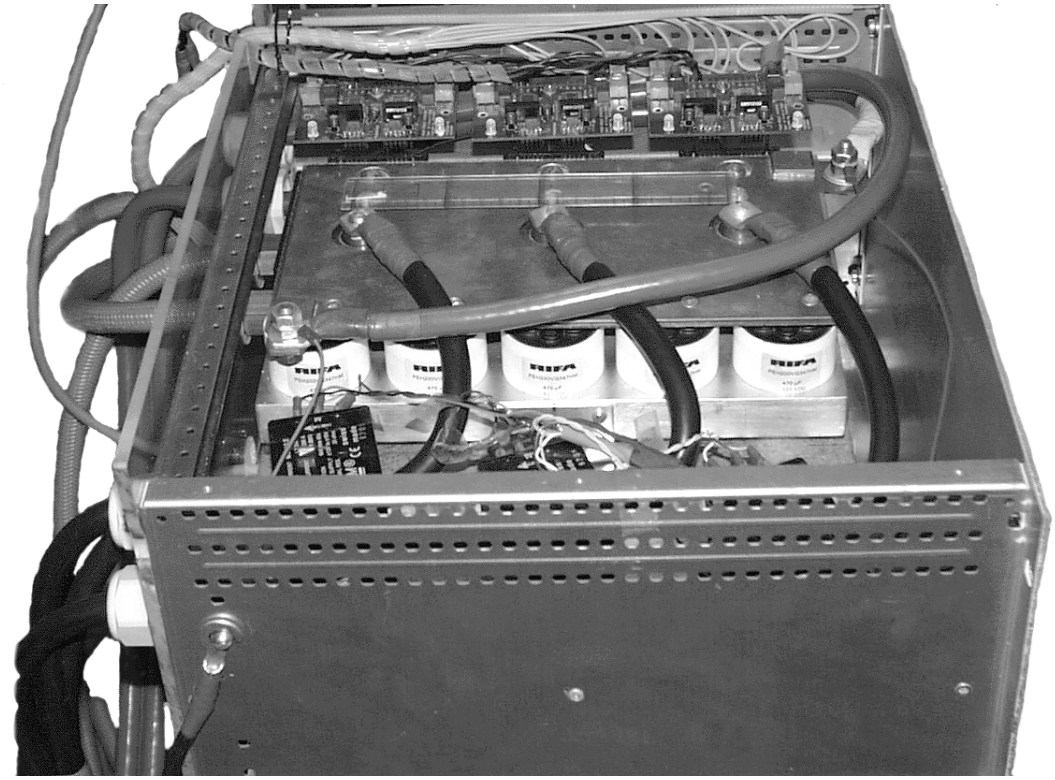

Figure 3: The power electronic converter in laboratory environment

Converter Rating

Maximum output current from the VSC is determined by the thermal restrictions for the power semiconductors. In steady-state operation, the limitation is determined by the cooling system. Current constraints in intermittent operation are related to the fatigue in the bonding construction of the power transistors and the thermal tension in their silicon structure, which usually is the limiting factor to be accounted for. Table 2 presents data on the power modules used in the VSC.

Table 2: IPM data at 25°C junction temperature

Manufacturer/Type	Mitsubishi/PM600DSA060
Max. dc-link voltage	450 V
Max. collector current	600 A
Max. collector dissipation	1790 W
Junction temperature	- 20°C – + 150°C
Collector-emitter saturation voltage	1.8 V (at 600 A)
Max. PWM switching frequency	20 kHz

The maximum output voltage depends on the dc-link voltage and the pulse width modulation (PWM) used with the converter. The influence of the PWM was accounted for by assuming that a method of symmetrical modulating waves was applied to a triangular-wave sub-oscillating modulator [5]. As a result, the converter rating is 125 kVA, based on the maximum motor current at intermittent operation, 320 A, and the assumed battery voltage, 320 V.

4 Laboratory Set-up

The experiments were conducted with a set-up connecting the converter to the experimental motor, according to Fig. 4. Measurements of the three phase currents were made using LEM-modules and the dc-link voltage was measured with a resistive voltage divider. An isolation amplifier provided galvanic separation between the dc-link voltage probe and the controller. Transfer of signals to the power modules was done through optical fibers, reducing electromagnetic interference with the control. The rotor position was measured with a resolver mounted inside the machine frame.

The IEA-MIMO controller [6] used is based on the TMS320C30 digital signal processor (DSP), enabling experimental investigation of various control strategies by software implementation of the control. Development of the controller software was made in a C-language environment, hosted by an ordinary desktop computer. Switching signals for the PWM are generated on a separate board, the IEA-PWM6, where the modulator is implemented in a programmable circuit [6].

Mechanically, the PMSM was connected to a DC-machine via a 3.09:1 reduction gear box and a torque transducer. A picture of the laboratory machine arrangement is shown in Fig.5.

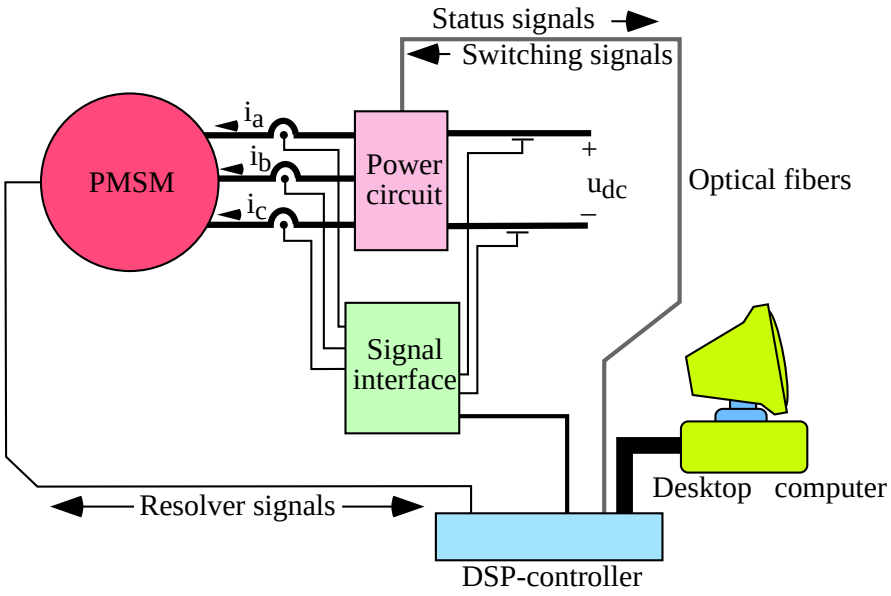

Figure 4: Drive topology

The primary aim of the measurements was to verify the performance of the PMSM. Because of the high efficiency of the experimental motor, special attention was given to the methods for determining the total losses. In addition to the measurements of electric input power and mechanical output power, a calorimetric

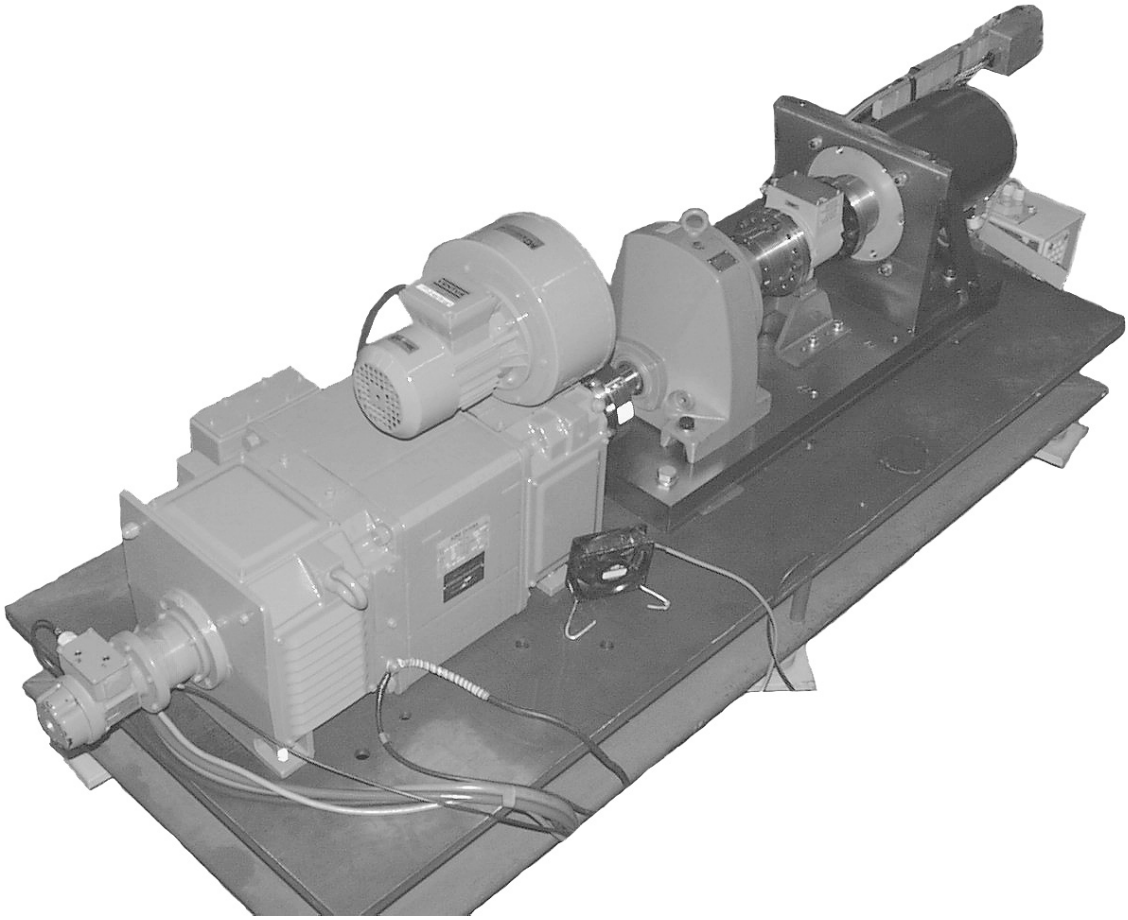

Figure 5: The PMSM (to the right) mechanically connected, via a reduction gear box, to a DC-machine (to the left) in the laboratory

method was used in order to improve the accuracy [4]. Figure 6 illustrates the laboratory set-up used for the experimental verification and the instruments used in the experiments are presented in Table 3.

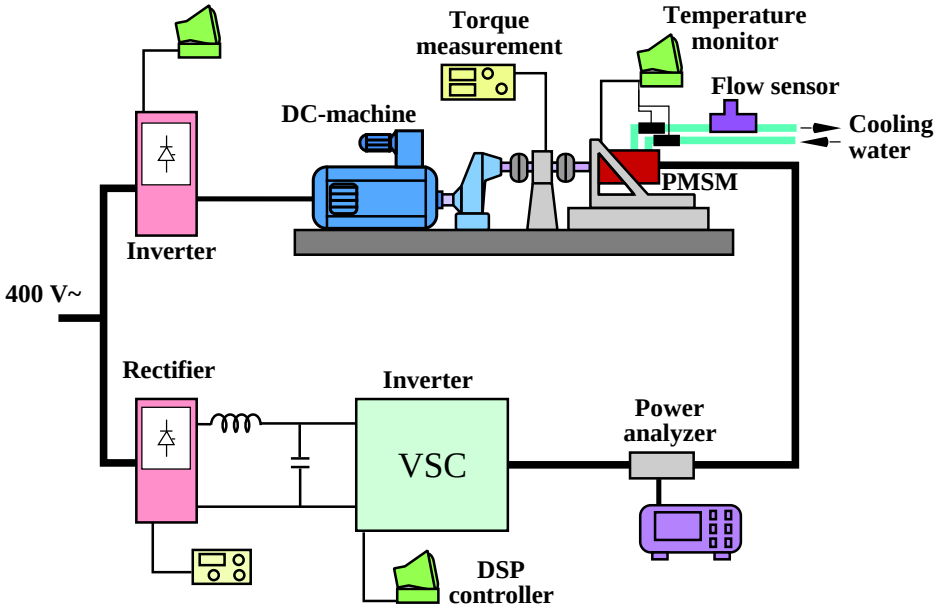

Figure 6: Laboratory set-up

Table 3: Instruments used in the experiments

Instrument	Measurement	Error m.v.: measured value m.r.: measuring range
NORMA D 6100 power analyzer	Electrical input quantities	not available
HMB T 32 FN torque transducer	Mechanical torque	±0.35% of m.v.
HMB MD 18 N signal amplifier	Mechanical torque	±0.15% of m.r.
Fluke 8060 A multimeter	Mechanical torque signal	±0.05% of m.v.
Fluke HYDRA 2625A data acquisition unit	Motor temperatures Coolant temperature rise	±0.42°C ±0.01°C
HP 54520 A oscilloscope	Flow sensor pulse frequency	
SIKA VTH 15 K5-40 flow sensor	Volumetric flow rate	±1.2% of m.v.
Le Croy 9410 oscilloscope	Curve tracing	

5 Theoretical Description of the Drive

5.1 Reference Frame

In this chapter, a space vector representation of the voltages, currents and flux-linkages is used to describe different characteristics of the drive system. The drive model is based on a rotating reference frame where the transformations between the three-phase stationary reference frame and the two-phase rotating reference frame are made on an amplitude invariant basis, assuming sinusoidally distributed windings in the machine. For this type of application, the center line of the rotor pole was chosen as a reference for the transformation to rotor coordinates, yielding the well-known dq-reference frame.

The operating point of a machine can be represented by the d-axis and q-axis stator current components, i_d and i_q, in a coordinate system (the dq-plane). Limitations, restrictions and characteristics of the drive can be presented graphically by plotting the currents at different speeds and loads in steady-state operation. The different trajectories and curves shown in this chapter originate from system parameters and the chosen control strategy.

The origins of the study are the voltage equations expressed in the dq-frame, where the d-axis and q-axis stator voltage components are

$$u_d = R_s i_d + L_d \frac{di_d}{dt} - \omega L_q i_q \tag{1}$$

and

$$u_q = R_s i_q + L_q \frac{di_q}{dt} + \omega L_q i_q + \omega \psi_m \tag{2}$$

where the stator resistance is denoted by R_s, the d-axis and q-axis synchronous inductances by L_d and L_q, respectively. ψ_m is the flux linkage due to the permanent magnets and ω is the angular frequency of the rotor. In the dq-frame, the expression for electrodynamic torque becomes

$$T_e = \frac{3}{2} p \left(\psi_m i_q + (L_d - L_q)\, i_d i_q \right) \tag{3}$$

where p is the pole pair number.

5.2 Converter Related Limitations

Torque production, and, hence, the output power of a current controlled drive is associated with the maximum current, i_{max}, determined by the converter rating. The current constraint is described by

$$i_d^2 + i_q^2 \leq i_{max}^2 \tag{4}$$

The trajectory of the maximum current vector, $\underline{i}_{max}$, forms a circle, centered in the origin of the dq-plane, as shown in Fig.7.

Furthermore, the voltage output from the converter is limited because of restrictions on the maximum allowed dc-link voltage, modulation constraints and power semiconductor characteristics. The maximum output voltage, u_{max}, limits the d-axis and q-axis voltage components by the relation

$$u_d^2 + u_q^2 \leq u_{max}^2 \tag{5}$$

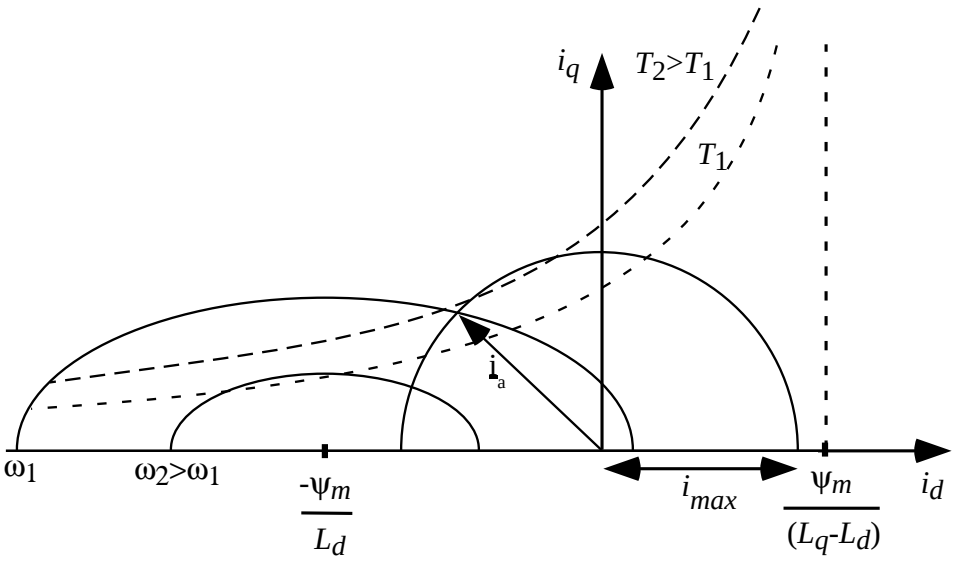

Figure 7: The drive characteristics, visualized in the dq-plane

5.3 Drive Limitations

The ability to control a variable speed drive is related to the knowledge of the limitations introduced by the combination of power electronics and machine. In

addition, the method of control selected to utilize the system becomes important [7] [8] [9] [10].

Rewriting Equation (5) and inserting Equations (1) and (2) makes it possible to visualize the voltage limitation in the dq-plane. For simplicity, voltage drops caused by armature resistances are neglected, yielding

$$\left(i_d + \frac{\psi_m}{L_d}\right)^2 + \left(\frac{L_q}{L_d} i_q\right)^2 \leq \left(\frac{1}{\omega L_d}\right)^2 \tag{6}$$

which describes an ellipse in the dq-plane, with its center at $i_d = \frac{-\psi_m}{L_d}$ and the ellipticity $\frac{L_q}{L_d}$, as illustrated in Fig.7. The limiting influence of the voltage can be seen as the speed increases and the voltage limit ellipse shrinks towards its center. Possible operating points are at all times inside the voltage limit ellipse [7] [8] [9] [10] [11].

In addition, curves representing constant torque show the characteristics of the machine. The curves originate from the torque expression in Equation(3), yielding hyperbolae in the dq-plane with the asymptotes $i_q = 0$ and $i_d = \frac{\psi_m}{L_q - L_d}$.

5.4 Motor Control Principles

Generally, a variable speed drive is controlled in two modes. In the constant torque region below the base speed, ω_b, the drive is able to deliver approximately constant torque. A further increase in speed requires control action in order to decrease the back-emf of the machine. A common method for extending the operating speed range is called flux weakening. The induced back-emf is decreased by imposing a de-magnetizing current component in the stator windings. For a PMSM model expressed in the dq-frame, the de-magnetizing current component is in the negative d-axis direction. Consequently, when a part of the current rating is used for flux weakening, there is less current left to be used for torque production.

Figure 8 illustrates the operating region chosen for the experimental motor. The base speed is 6000 rpm, up to which the motor shall deliver 80 Nm in continuous operation and 160 Nm in intermittent operation. As mentioned previously, the CPSR chosen for the machine is 2:1, which means that the output power is limited to 50 kW in continuous operation from the base speed up to twice the base speed. In the same way, the output power is limited to 100 kW in intermittent operation.

Maximum torque in the constant torque region is achieved by applying any current vector along the maximum torque hyperbola. However, there are restrictions due to limitations introduced by the converter and power supply, and the choice of control strategy can also affect the current drawn from the supply, the power factor and the efficiency of the system [12].

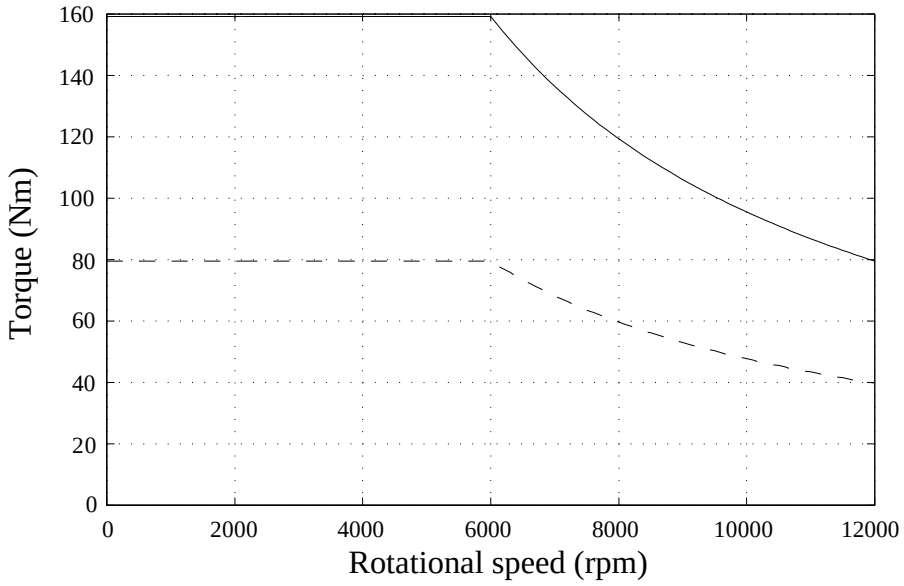

Figure 8: Operating region of the experimental motor

Maximum torque in the flux-weakening region is achieved if the operating current vector trajectory follows the intersection between the voltage limit ellipse and the maximum current circle [7] [9] [10] [11] [8]. However, at partial load, the desired torque can be achieved by finding the intersection between the voltage limit ellipse and the torque command hyperbola.

The control scheme used in the experiments is shown in Fig.9. Measured quantities in the system are the dc-voltage, the phase currents and the rotor position. The conversion of the measured quantities from analogue to digital format is done synchronously and at a sampling interval equal to the inverse of the switching frequency. The measured current signals are transformed to the rotating dq-reference frame using the A/D converted rotor position signal and are, then, fed to the current controller.

The desired voltage reference values from the current controller, expressed in the dq-frame, are transformed back to the stationary three-phase reference frame using an estimated rotor position 1.5 samples ahead of the time instant when the actual quantities are measured.

After the coordinate transformation, the reference values are generated, fed to the modulator and converted to switching commands. An analogue blanking time control circuit was used to prevent two transistors in the same phase-leg from conducting at the same time. The switching signals are transferred to the power circuit via an optical interface, which also receives over-current and over-temperature signals from the IPM's.

The control system includes a pulse-width modulator based on a sinusoidal sub-

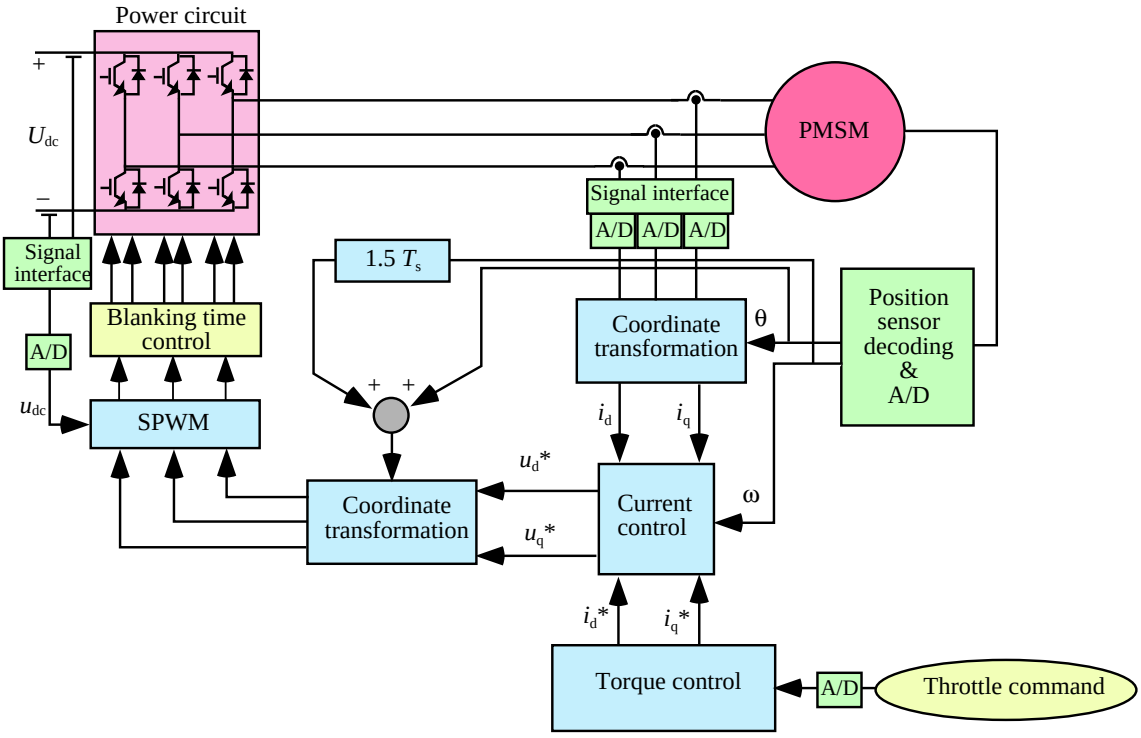

Figure 9: The control scheme

oscillating technique using a triangular carrier wave (SPWM). Due to the inherent limitation of the output voltage with the pure SPWM, the power utilization of the VSC is improved by the implementation of a method for maximum PWM output voltage called the SPWM-Sym. This method is based on the possibility of adding an offset to the phase voltage reference values without changing the demanded phase voltage-time area. With the SPWM-Sym method, the maximum armature voltage is [5]

$$u_{max} = 1.155\frac{U_{dc}}{2} \tag{7}$$

where U_{dc} is the dc-link voltage. The method yields a 15.5% higher voltage output compared with a pure SPWM, hence, increasing the VSC power rating by 15.5%.

5.5 Current Control

Achievement of good dynamic properties is generally the aim of a drive operating in a servo application. This requires a carefully designed control system and good knowledge of the drive characteristics. In such a system, it is essential to use a fast, accurate and robust current controller.

In a normal vehicle application, the requirement for a very fast dynamic response is of minor significance, since the dynamics of the vehicle is much slower than the time constants of the drive. Even though a dynamic response similar to that of a servo drive is not necessary, the influence of the current control is important. Aiming for best possible energy efficiency requires control of the drive to the desired state at any operating point within the specified range. A current controller unable to satisfy this demand would deteriorate the performance even in steady-state, yielding higher losses and, consequently, lower efficiency.

The current control implemented for the experiments is described by the controller equations at sample k

$$u_d^*(k) = K_{pd}\left(i_d^*(k) - i_d(k)\right) + R_s i_d(k) - L_q\omega(k)i_q(k) + \Delta u_d(k) \tag{8}$$

and

$$u_q^*(k) = K_{pq}\left(i_q^*(k) - i_q(k)\right) + R_s i_q(k) + L_d\omega(k)i_d(k) + \omega(k)\psi_m + \Delta u_q(k) \tag{9}$$

where * denotes the desired quantities. K_{pd} and K_{pq} are the proportional controller gains in the d-direction and q-direction, respectively. An example of how

expressions for K_{pd} and K_{pq} can be found for a dead-beat proportional controller is given in Appendix B. The experiments did not require a dead-beat response, but dead-beat gains were used as an upper limit for setting the controller parameters. A reduction of remaining control errors was achieved with integral controller components represented by

$$\Delta u_d(k) = K_{id} \sum_{n=0}^{k} (i_d^*(n) - i_d(n)) \tag{10}$$

and

$$\Delta u_q(k) = K_{iq} \sum_{n=0}^{k} \left(i_q^*(n) - i_q(n)\right) \tag{11}$$

where K_{id} and K_{iq} are the integral controller gains in the d-direction and q-direction, respectively.

Equations (8) and (9) describe a well-known PI-controller with feed-forward compensation for resistive and inductive voltage drops and induced back-emf. In the constant torque region, the armature current is controlled to produce the desired torque, which can be achieved in several ways. In machines with constant air gap, a quadrature current control, i.e. $i_d = 0$, is commonly used since the method produces maximum torque per armature current unit$(max\left(\frac{T}{i}\right))$. A salient-pole machine like the experimental motor, with different values of L_d and L_q, offers the potential to utilize a reluctance torque component as well, which means that the minimum current vector is not in the q-direction. The minimum current vector expressed in the d- and q-components is instead found from [13]

$$i_d = \frac{\psi_m}{2(L_d - L_q)} \pm \sqrt{\frac{\psi_m^2}{4(L_d - L_q)} - i_q^2} \tag{12}$$

Further details on current minimization can be found in Appendix A. The trajectory of the armature current vector for the PMSM, according to Equation (12) is shown in Fig.10.

For theoretical studies, ideal valves are often used to model the power semiconductors, but in real applications, errors will occur if the valves are treated as ideal components. The errors arise from nonlinearities in the power semiconductors due to on-state voltage drops. To compensate for the non-ideal performance of the valves, conduction voltage drops should be taken into account in the controller equations for both the transistors and the anti-parallel diodes. Further errors are

introduced by the blanking time, which prevents two transistors in the same phase leg from conducting at the same time. Both the conduction voltage drops and the blanking time errors were compensated by using a method presented by Svensson and Lindgren [14] [15].

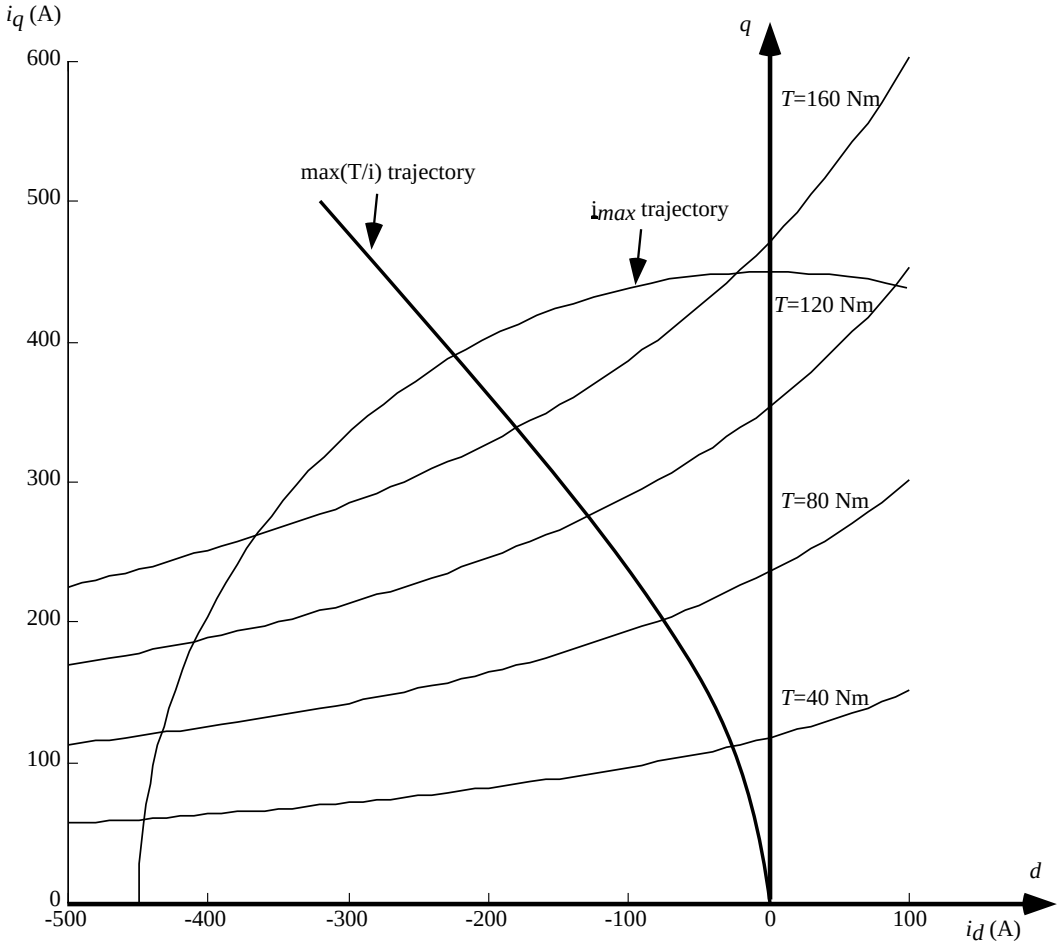

Figure 10: Characteristics of the experimental drive

6 Results

In this chapter, the results of the measurements are presented. A comparison with the preliminary results from the numerical computations is made. The originally calculated losses have been adjusted with regard to the measured winding temperature, the measured winding resistance and the measured open-circuit losses.

Two control modes were used in the measurements. The first mode was a manual control where the d-axis and q-axis currents were assigned separate reference values with the aim of keeping the direct current at zero ($i_d = 0$). Drive limitations, previously described in Section 5.3, restrain the possibility of obtaining the desired torque with $i_d = 0$ at high speeds. In such cases, the d-axis current was adjusted manually to a stable operating point without regard to any general control rules.

In the second mode, a maximum torque per ampere control was implemented, using a torque command as input. The d-axis current command was calculated from an approximate polynomial expression.

The control was implemented assuming constant machine parameters. The winding resistance and flux linkage due to the permanent magnets were derived from measurements and the synchronous d-axis and q-axis inductances were calculated by means of a finite-element method [3].

6.1 Open-Circuit Tests

An initial test of the experimental motor was conducted with the armature circuits open. Calorimetric loss measurements were, unfortunately, not possible to carry through at that time. The machine was brought to constant rotational speed by the mechanically connected dc-machine, and the induced armature voltage and applied shaft torque were measured. An example of the measured phase to neutral open-circuit voltage is shown in Fig.11, where the influence of the stator slotting is clearly visible, as well as the trapezoidal wave shape due to the rotor geometry.

The measured open-circuit losses presented in Fig.12 are associated with a high inaccuracy, especially at low speeds, because of the limited resolution of the torque measurement system. Measurements of very small torque magnitudes require a torque transducer made for such conditions in order to obtain a high accuracy.

6.2 Generator Operation Tests

Generator tests were conducted, where the PMSM was mechanically driven by the dc-machine and the armature currents were fed to an adjustable three-phase resistance. The tests were considered to be an intermediate step in the investigation, before the final motor tests were carried out.

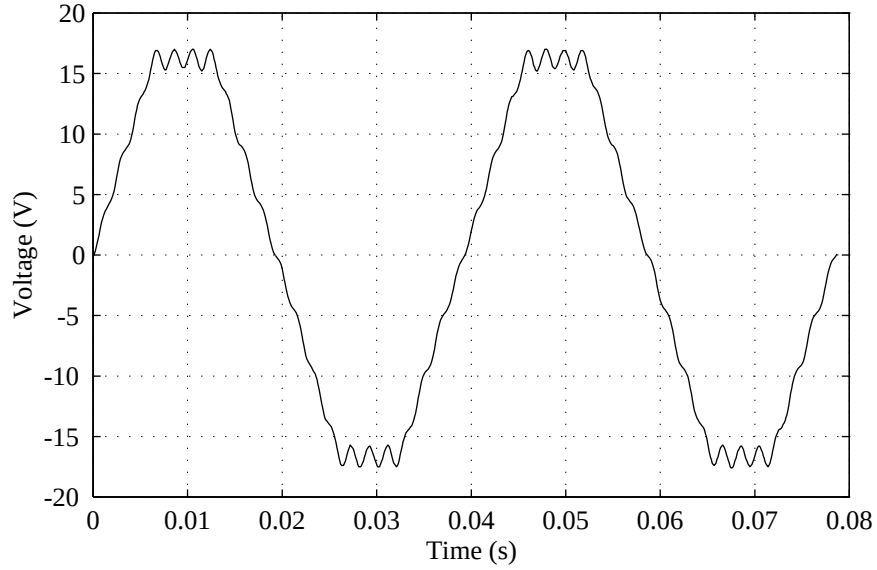

Figure 11: Open-circuit phase-to-neutral voltage at 764 rpm

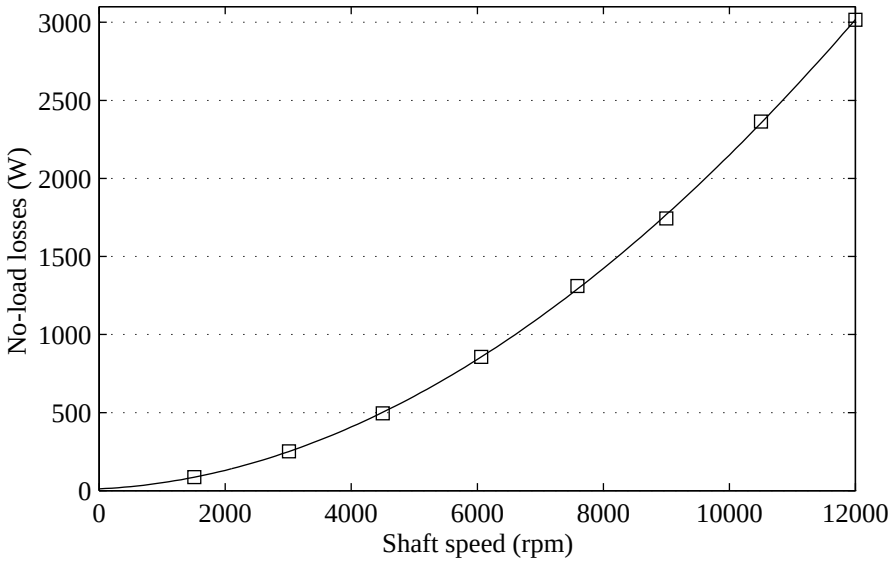

Figure 12: Measured open-circuit losses; the line is a curve fit

By letting the armature current increase at each step in the test series, the thermal properties of the machine were revealed in a controlled way without any critical temperatures occurring. The generator test sequence was also an important step in the calibration procedure of the calorimetric measurements. A few operation points were investigated in terms of losses and efficiency, with good results [16].

6.3 Motor Operation Tests

Measurements of the losses in motor operation were obtained using a switching frequency of 6 kHz, which, in this case, is equal to the sampling frequency of the control system. The investigated operating region involves speeds up to 6000 rpm and torque up to 80 Nm. Motor characteristics in flux weakening operation were, thus, not included in the tests.

In this section, a comparison of the losses calculated by means of a finite-element method and the measured losses is made. The sum of the calculated loss components is presented with the measured results. The calculated loss components include friction losses, winding losses, iron losses and eddy-current losses in the permanent magnets. In addition, a representation of the calculated loss components with additional open-circuit losses included is also presented, as shown in Figs.13, 14, 15 and 16. The deviation at low speeds may be a consequence of the high inaccuracy associated with the measurements of the open-circuit losses.

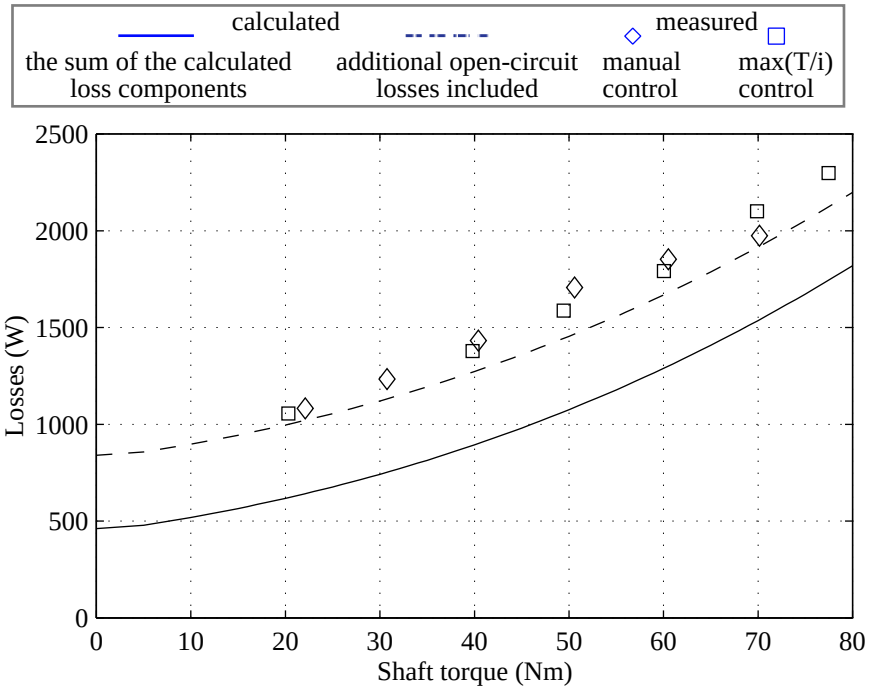

Figure 13: Predicted and measured total losses at 6000 rpm

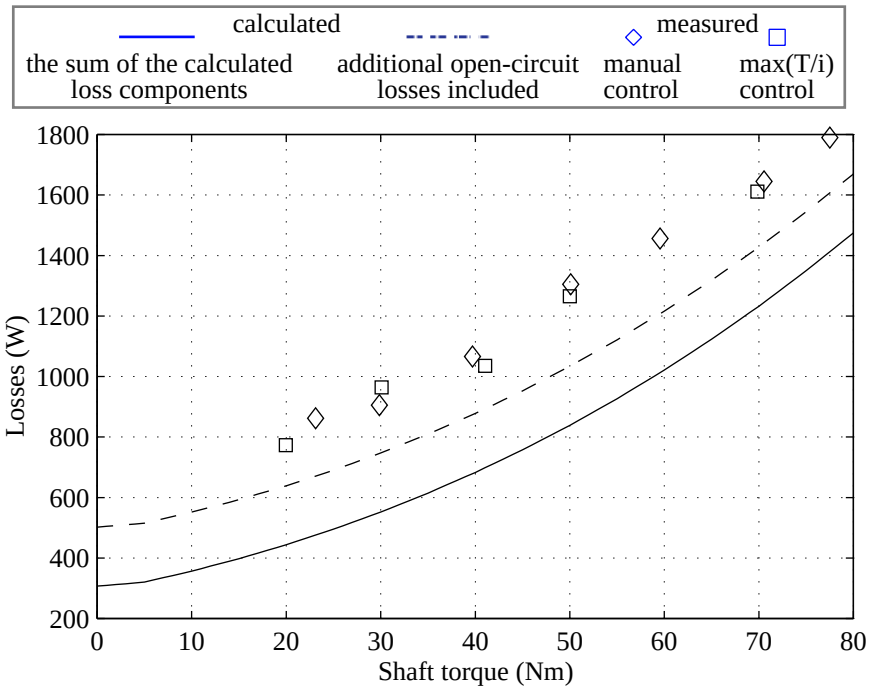

Figure 14: Predicted and measured total losses at 4500 rpm

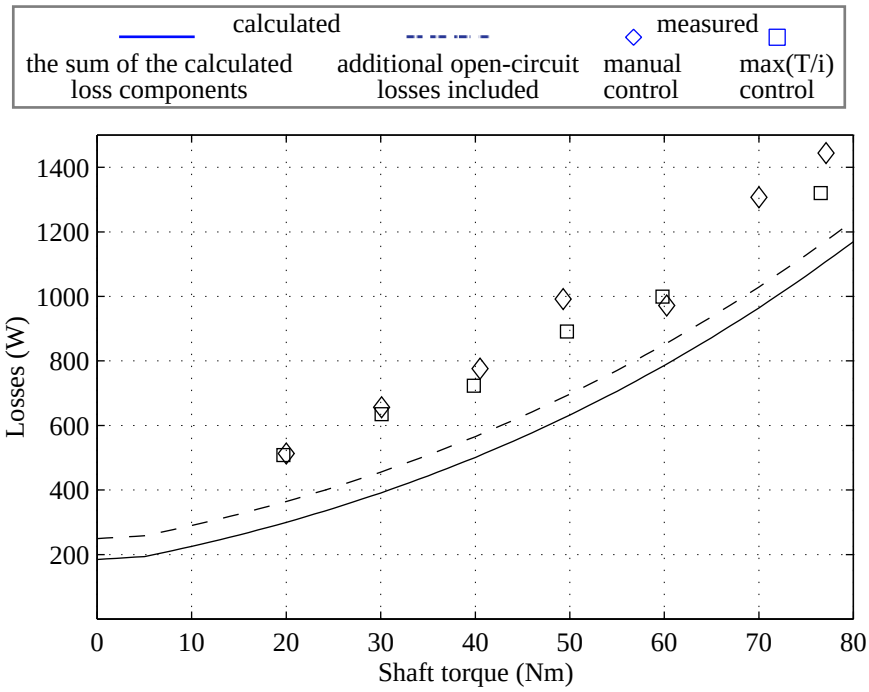

Figure 15: Predicted and measured total losses at 3000 rpm

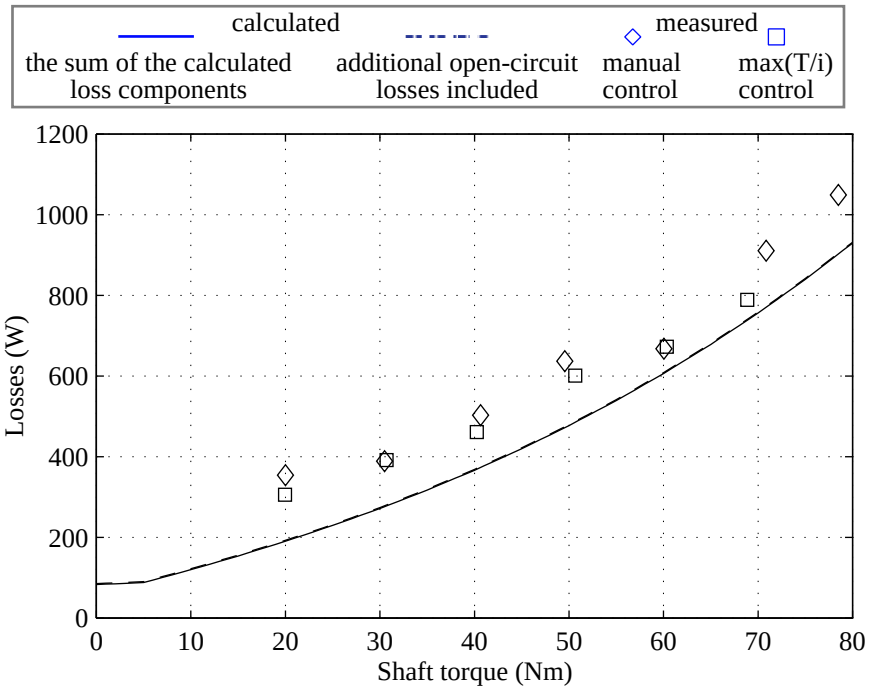

Figure 16: Predicted and measured total losses at 1500 rpm

The motor efficiency was calculated using the calorimetrically measured losses and the measured mechanical output power. Measured and calculated results of the motor efficiency are presented in Figs 17, 18, 19 and 20. In analogy with the presentation of the losses, an additional curve is presented. It represents the efficiency derived from the calculated loss components, taking the measured open-circuit losses into account.

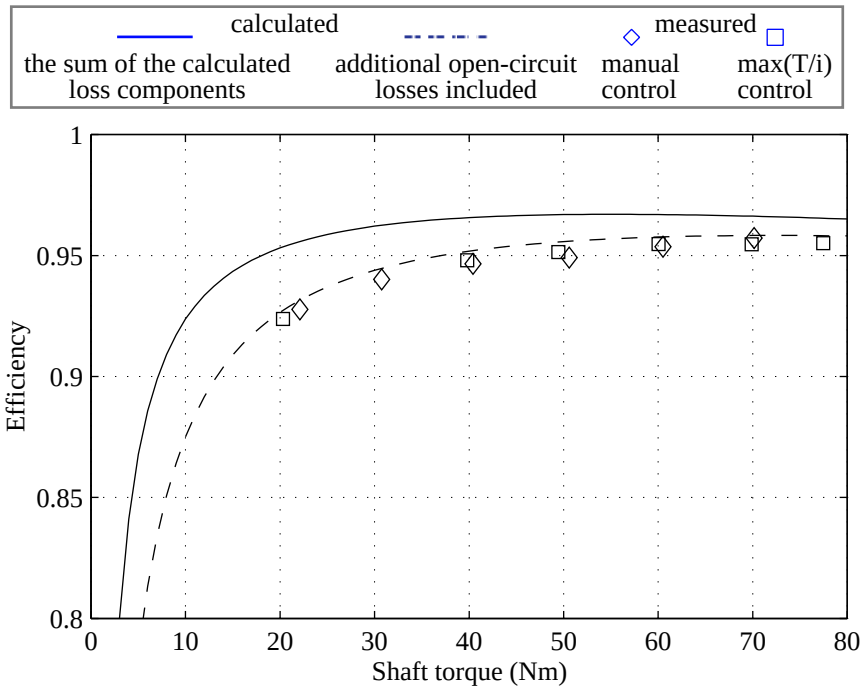

Figure 17: Predicted and measured efficiencies at 6000 rpm

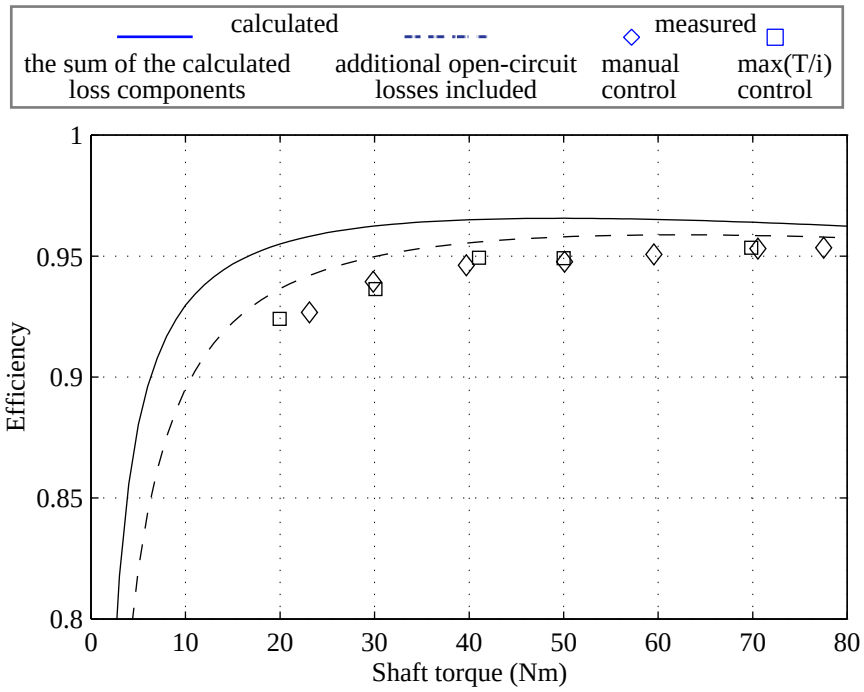

Figure 18: Predicted and measured efficiencies at 4500 rpm

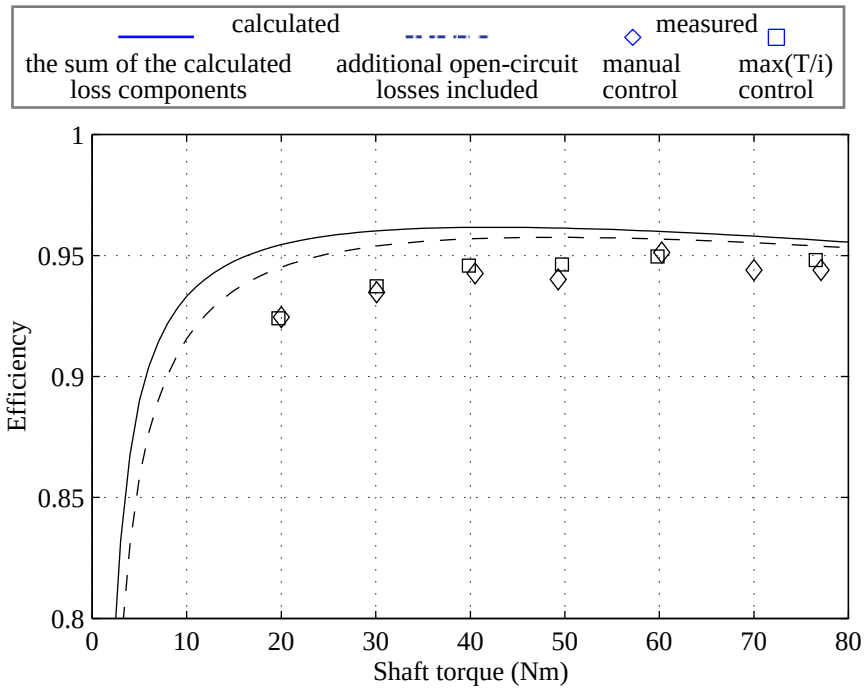

Figure 19: Predicted and measured efficiencies at 3000 rpm

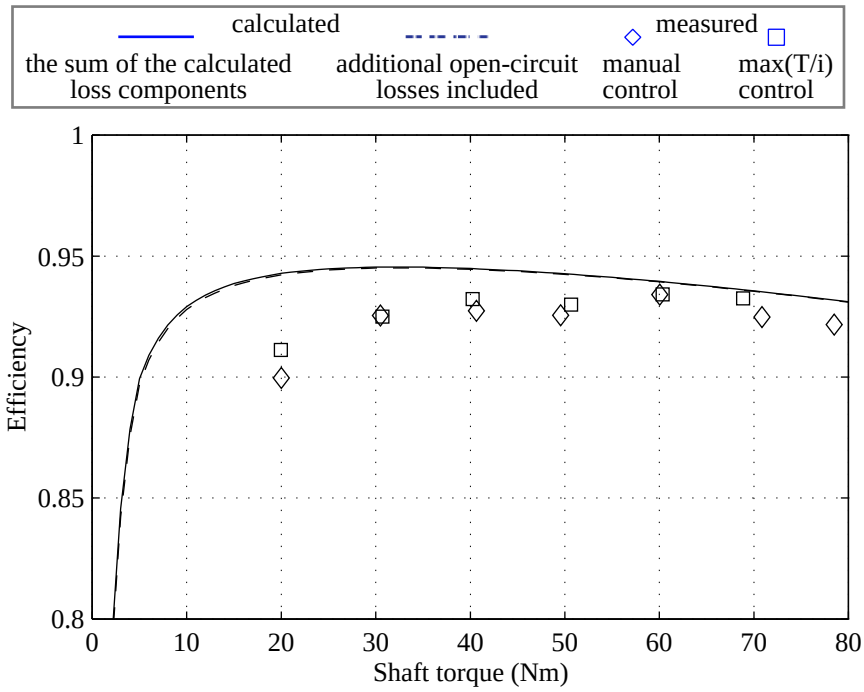

Figure 20: Predicted and measured efficiencies at 1500 rpm

6.4 Error Estimation

The calorimetric measurements of the total motor losses basically involve four important aspects:

The temperature rise measurement of the coolant can be made with good precision. Attention was given to the mounting of the temperature sensors and a calibration with respect to the individual properties of the sensors was made. As a result, the temperature rise of the coolant can be determined within $\pm 0.01°C$.

Coolant properties usually vary with temperature and pressure, which can influence the accuracy depending on the conditions. Temperature dependent variations in density and specific heat capacity were taken into account by using curve fits of the coolant characteristics.

The coolant flow rate measurement is generally a greater source of error than the temperature measurement. Calibration of the instruments used was done in the flow rate region of interest.

The heat leakage which is not registered by the calorimetric method is, in most cases, dependent on outer circumstances. Changes in the surroundings, like temperature, draught and moisture, influence the conditions and, consequently, the amount of heat leaking out of the system. A model of heat leakage combined with temperature measurements of the laboratory environment made it possible to estimate the influence of the leakage. During the experiments, the maximum estimated heat leakage was 17 W.

An estimation of the errors in the loss measurements, including the forementioned aspects, has shown that the total losses can be determined within ± 3.5 % of the measured value in the investigated operating region. At the nominal operating point, the error is less than ± 2.3 %. Further details are presented in Appendix C.

The efficiency of the motor was determined from the calorimetric loss measurements and the measured output power. At the nominal operating point, the measured efficiency was 95.5 %. Analysis of the errors has shown that the lower limit of the efficiency is 95.3 % and the upper limit is 95.6 %.

6.5 Discussion

Accurate computations of the losses in an electrical motor requires detailed information on the material properties and good models of the processes yielding the loss dissipation. Complete knowledge of all components in the motor was not available in the early stages of the project, which left a number of uncertain factors to be revealed.

The measured results presented in this chapter cannot provide a detailed explanation of the discrepancies between calculated and measured losses. A complete separation of the loss components requires additional information based on new computations and measurements. However, a straightforward loss separation, based on the available information, was made to identify the possible sources of error.

Subtraction of the winding losses and friction losses from the total losses leaves a lumped quantity of remaining losses including:

- iron losses in the stator
- iron losses in the rotor
- eddy-current losses in the permanent magnets
- additional losses

which are difficult to separate. The additional losses were not included in the calculations, which emphasizes the difficulty in judging the presented results. A comparison of the remaining losses has shown that the measured quantity was about twice the corresponding quantity of the calculated loss components. A possible reason for this is that the additional losses are high. Possible sources contributing to the deviations are:

Air friction is not negligible in a motor at high speeds. The model used for air friction has not been verified experimentally because of inherent difficulties with loss separation. Iron losses are always present since the excitation of the magnetic circuit is provided by permanent magnets. A simple test frequently used with ordinary machines is the retardation test [17]. Retardation tests with a PMSM would be possible if a dummy rotor without magnets could be constructed. An investigation of friction losses is a topic which should be included in future work with the experimental motor.

The finite element calculations are two-dimensional, neglecting all flux components in the axial direction. The end regions of the machine are, thus, not included in the numerical solution of the magnetic field, and eddy-current losses induced in the regions are neglected. The prediction of stator currents takes the end regions into account, since they are modeled approximately as constant end-winding impedances in the circuit equations. The iron losses are calculated based on the Fourier analysis of the flux density variation [18] [19]. The method is approximate and its accuracy is not always good. Furthermore, the terminal voltage of the motor is assumed to be sinusoidal and, therefore, the influence of voltage harmonics is neglected [3]. The permanent magnets are subdivided into insulated pieces in the axial direction in order to reduce the eddy currents in the magnets. In the finite element analysis, this

effect is only approximately taken into account by increasing the resistivity of the magnets [1]. The chosen manufacturing processes might have affected the properties of the experimental motor. The electrical insulation between the sheets of the iron core in both the stator and the rotor is important for the losses caused by induced eddy-currents. Any damage to the insulating layers provides a current path, giving rise to increased losses. Laser cutting was chosen for the shaping of the electrical sheets and the stator core was welded to obtain the required mechanical strength.

The control used in the experiments was the result of a preliminary study and, thus, not optimized for low losses. Operation at high speeds, close to the base speed, resulted in overmodulation yielding low-frequency current harmonics. The increase in harmonic content caused additional losses due to induced eddy currents and skin effect. The loss calculations were made on the basis that the specified output torque was achieved at the voltage yielding minimum losses in the motor. Mappings of the corresponding currents for the dq-model are needed to obtain the same conditions in the experimental drive as in the finite-element calculations.

6.6 Influence of the Control Method

Minimization of the armature current is a well-known and frequently used method for the control of variable speed drives. Increasing speed is associated with increasing back-emf in the motor, which at some point will naturally affect the possibility of obtaining the desired armature current. As expected, the control method resulted in overmodulation when the back-emf of the PMSM was in the vicinity of the attainable output voltage of the VSC.

The observed overmodulation at high speeds, caused by the limited dc-link voltage, was emphasized under conditions with a high load, naturally associated with a high armature current. An increase in the currents yields high voltage drops in the stator windings and in the power electronic semiconductors, which enhances the situation.

An example from the test using the $max\left(\frac{T}{i}\right)$ strategy is presented below, to show the difference in current response between two operating points with approximately the same load, but at different speeds. As can be seen in Figs.21 and 22, the harmonic content in the armature current is low and the current controller works well.

For comparison, the wave shape and harmonic content of the current are shown in Figs. 23 and 24, where the speed is about equal to the base speed. Current controller saturation causes a high harmonic content, which increases the losses by enhancing the skin effect and giving rise to increased eddy-current losses.

To clarify the situation, an example of the controller influence is illustrated in Fig.25, where the experimental drive is assumed to operate at nominal speed

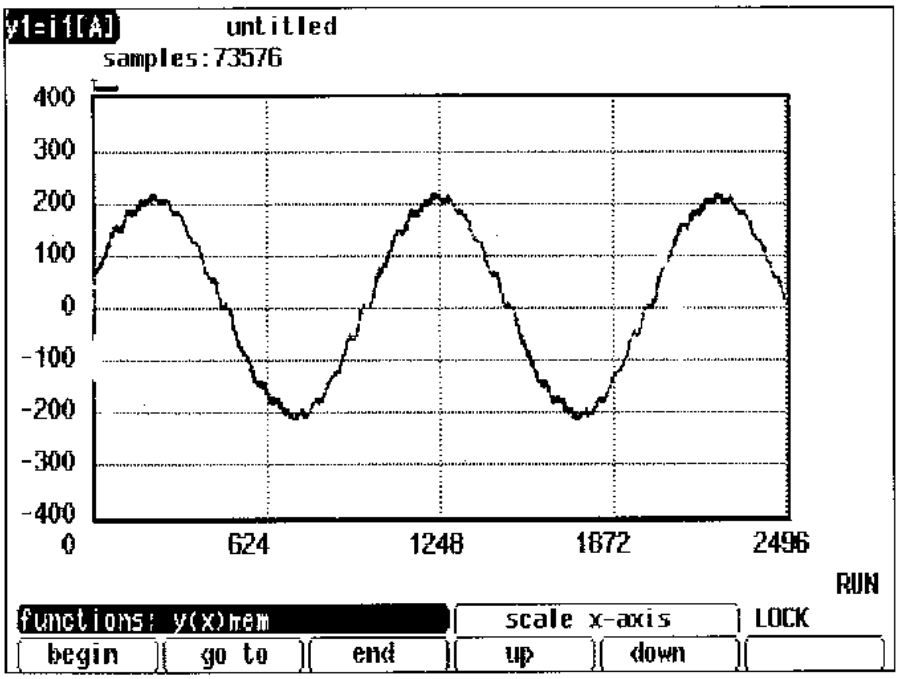

Figure 21: Armature current at 1500 rpm, 70 Nm

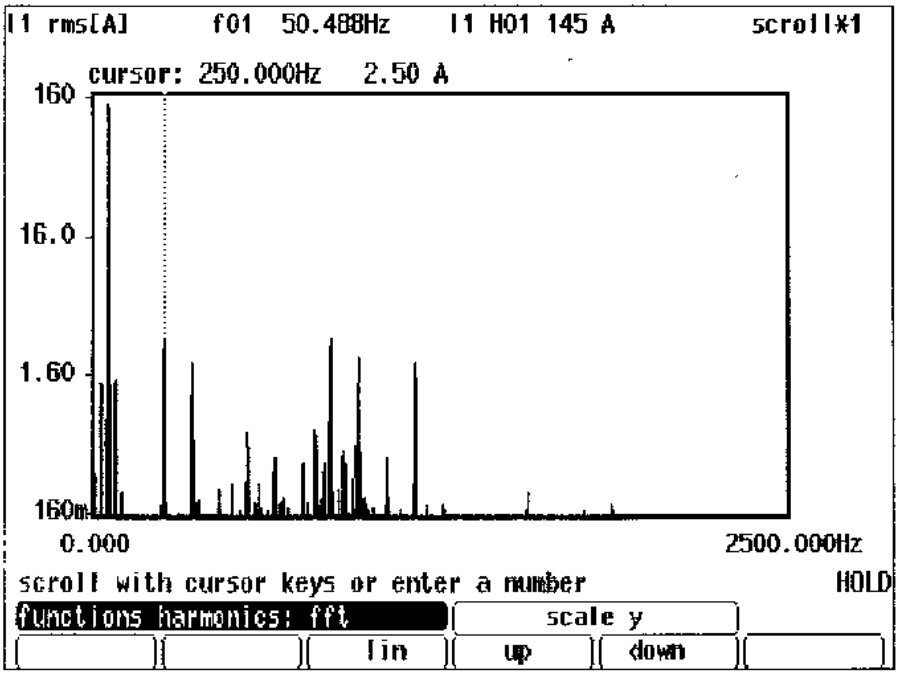

Figure 22: Armature current spectrum at 1500 rpm, 70 Nm

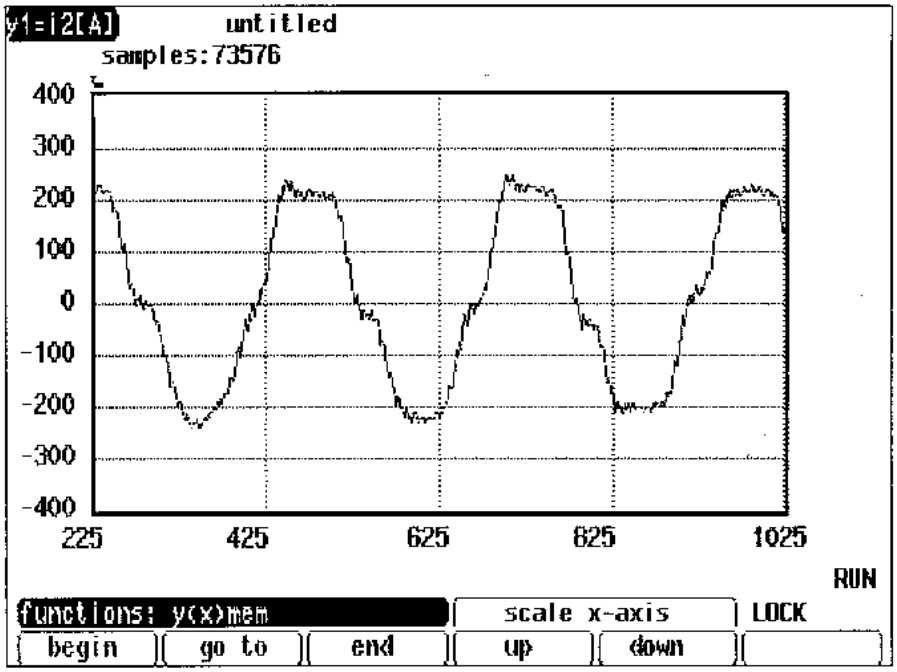

Figure 23: Armature current at 6000 rpm, 80 Nm

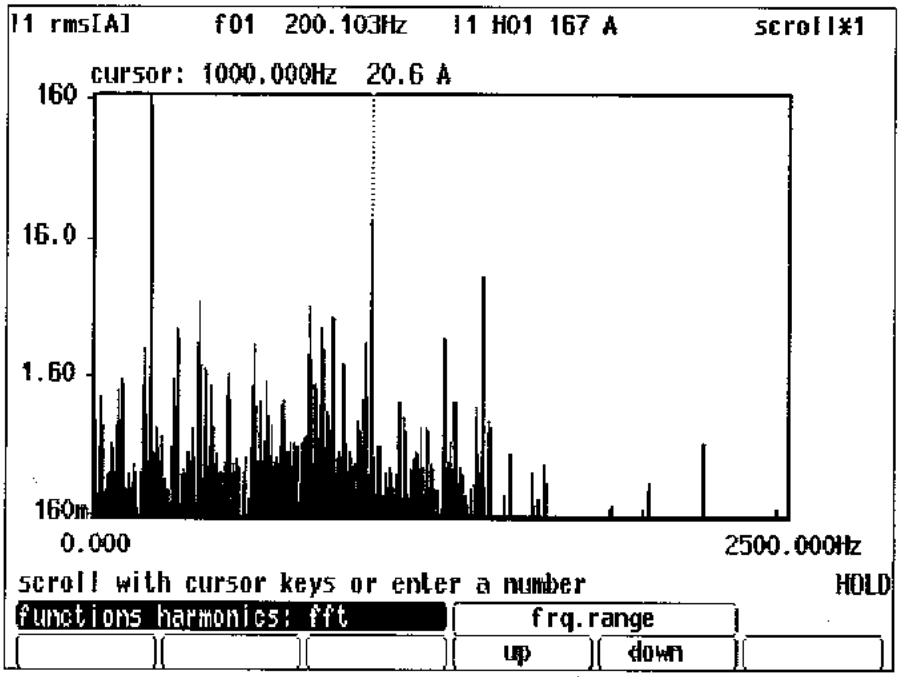

Figure 24: Armature current spectrum at 6000 rpm, 80 Nm

and load, and the resistive voltage drops have been neglected. According to the $max\left(\frac{T}{i}\right)$ control strategy, the current vector corresponding to the situation is represented by $\underline{i}_{a2}$. As can be seen, the current vector is attainable, i.e., within the voltage limit ellipse, according to the assumed conditions. In a practical case, the resistive voltage drops would cause the voltage limit ellipse to shrink towards its center, possibly leaving the intersection between the nominal torque curve and the $max\left(\frac{T}{i}\right)$ trajectory outside the voltage limit ellipse. On such an occasion, the result is a current controller demand, which cannot be achieved, and consequently, the current controller becomes saturated.

Another aspect is to compare the $max\left(\frac{T}{i}\right)$ control with the $i_d = 0$ control. As mentioned before in Section 5.5, a salient pole machine requires a d-axis current component in order to minimize the current, given a specific torque. Furthermore, use of the $i_d = 0$ control with a salient pole machine will cause an encounter with the current controller saturation due to an increase in back-emf at a lower speed than with the $max\left(\frac{T}{i}\right)$ control.

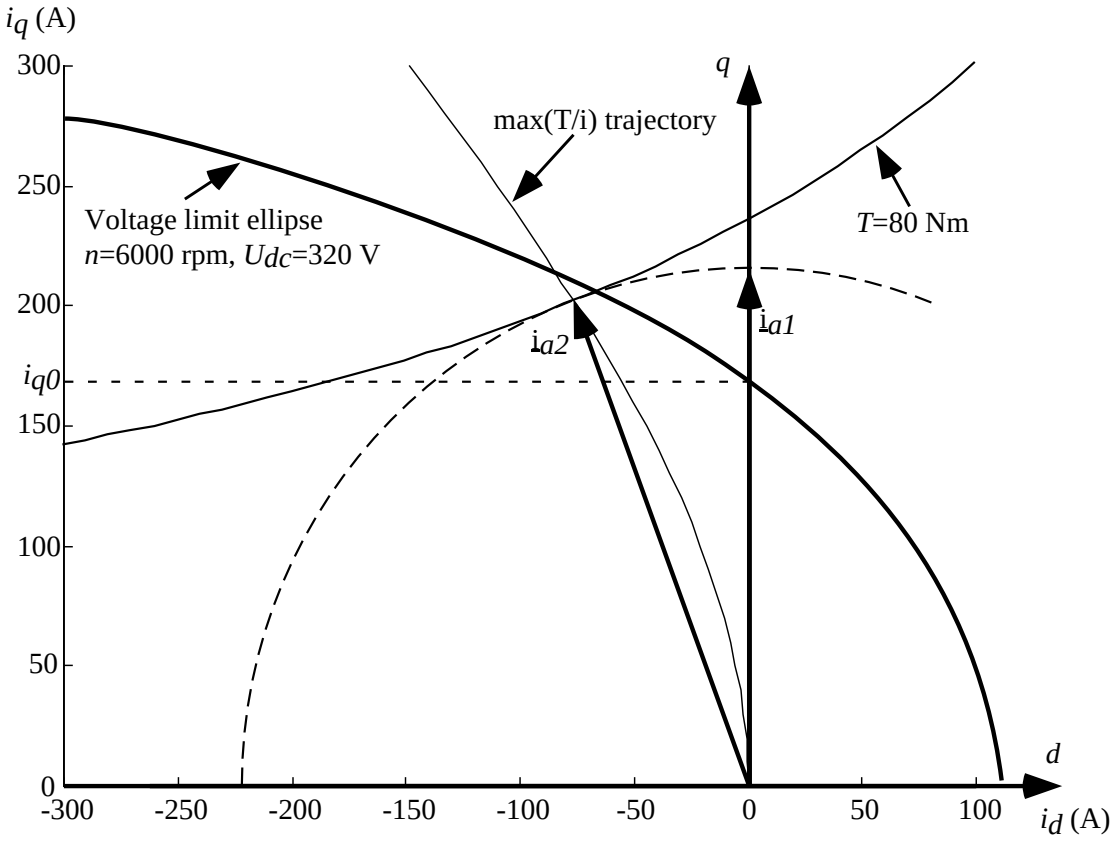

Figure 25: Control dependent limitations

Figure 25 also illustrates the deteriorated response due to the chosen control strategy. The current vector $\underline{i}_{a1}$, representing the $i_d = 0$ control, has the same magni-

tude as $\underline{i}_{a2}$, which corresponds to nominal torque with the $max\left(\frac{T}{i}\right)$ strategy. The highest attainable current using the $i_d = 0$ control in this example is i_{q0} due to the limited output voltage. In comparison with the $max\left(\frac{T}{i}\right)$ control, the deteriorated current response would occur at a lower speed, hence degrading the output power capability of the drive.

In addition to the inherent control restrictions at high speeds, there may be further errors introduced by parameter variations. One major parameter variation arises from magnetic saturation, which causes a decrease in the synchronous inductance in the q-axis direction. Another phenomenon, possibly affecting the control, is dq-crosscoupling due to saturation [20]. Neither saturation nor crosscoupling effects have been taken into account in the experiments presented here, but they might be a subject for investigation in future work.

Variations in the frequency and harmonic content of the stator current affects the resistance of the windings due to the skin effect and proximity effects. Furthermore, the temperature of the windings changes as the load and speed of the machine varies, yielding additional variations in the winding resistance.

The influence of the winding resistance and the synchronous inductances can cause the controller feed forward compensation to lose its effectiveness, especially at high speed [11]. In normal cases, the winding resistance is regarded as a minor influence, but saturation of the q-axis inductance should be taken into account, especially at high load currents, at which the improvement may be significant [13] [7] [10].

7 Conclusion

A complete drive system for experimental investigation has been developed, assembled and tested. The central part of the drive is an inverter fed permanent-magnet motor optimized for a hybrid electric vehicle. The voltage source converter used with the drive was built specially for the motor and a digital control system was included to enable experimental investigation of various control strategies.

Different control methods suitable for the inset-magnet motor design were studied. A current minimization strategy was implemented for the experimental drive and, in addition, a manual control was used for comparison. Below the base speed, the commonly used current minimization strategy works well and utilizes the motor capacity better than the quadrature axis current control. Results from the tests show that there are differences in motor performance depending on which control strategy is chosen.

The predicted torque characteristics agree well with the ones experienced in the laboratory. Moreover, the induced emf corresponds well to the expected performance, which indicates that the calculated flux linkage agrees well with the real one.

The total losses of the PMSM were measured with a calorimetric method in order to obtain a high accuracy. Calculations show that the improvements in accuracy, compared with the traditional input-output method, are significant. Estimations of the accuracy of the calorimetric method show that the total losses can be determined within $\pm 3.5\%$ of the measured value in the whole operating region investigated. At the nominal operating point, the error was less than $\pm 2.3\%$. Estimation of heat leakage from the system is essential for the accuracy of loss measurements. Results show that the heat which was not absorbed by the cooling water was less than 17 W in the worst case.

The maximum motor efficiency measured, 95.5 %, was obtained at nominal speed and load. Analysis and estimation of the errors has shown that the lower limit of the efficiency was 95.3 % and the upper limit of the efficiency was 95.6 %.

Preliminary analysis of the obtained test results indicates that the additional losses are significant. The observed discrepancies between measured and predicted losses are related to the additional losses, since they were neglected in the previously made calculations.

Further investigations associated with the control aspects should be conducted in order to validate the experimental motor to its full extent. The performance in flux weakening operation is of special interest and should be brought to attention. Experimental investigation of the friction losses is required for loss separation and to improve the analysis of measured results.

References

[1] J. Luomi, J. Lindström, and J. Hellsing, "Design and analysis of electrical motors for a hybrid electric vehicle," in *IEEE/Stockholm Power Tech Conference Proceedings*, Stockholm, Sweden, June 18-22 1995, vol. Electrical Machines and Drives, pp. 274–279.

[2] J. Lindström, J. Hellsing, and J. Luomi, "Design of high-efficiency electrical motors for a hybrid electric vehicle," in *EVS-13 Proceedings*, Osaka, Japan, October 13-16 1996, vol. II, pp. 64–69.

[3] J. Hellsing, "Design and optimization of a permanent magnet motor for a hybrid electric vehicle," Licentiate thesis, School of Electrical and Computer Engineering, Chalmers University of Technology, Göteborg, Sweden, March 1998, Tecnical Report No.282L.

[4] T. Larsson, "Calorimetric measurement of losses of a permanent magnet synchronous motor," M.Sc.thesis, Department of Electric Power Engineering, Chalmers University of Technology, Göteborg, Sweden,, June 1998, Report No.27E.

[5] T.Svensson, *On Modulation and Control of Electronic Power Convertors*, Ph.D. thesis, School of Electrical and Computer Engineering, Chalmers University of Technology, Göteborg, Sweden, 1988, Technical Report No.186.

[6] A. Carlsson, "The back-to-back converter – control and design," Licentiate thesis, Lund Institute of Technology, Lund, Sweden, May 1998.

[7] W.L. Soong and T.J.E. Miller, "Practical field-weakening performance of the five classes of brushless synchronous ac motor drives," in *EPE'93 Proceedings*, Brighton, U.K., September 13-16 1993, vol. 5, pp. 303–309.

[8] S. Morimoto, Y. Takeda, T. Hirasa, and K. Taniguchi, "Expansion of operating limits for permanent magnet motor by current vector control considering inverter capacity," *IEEE Transactions on Industry Applications*, vol. 26, no. 5, pp. 866–871, September 1990.

[9] W.L. Soong and T.J.E. Miller, "Theoretical limitations to the field-weakening performance of the five classes of brushless synchronous ac motor drives," in *Sixth International Conference on Electrical Machines and Drives (Conf. Publ. No.376). IEE*, Oxford, U.K., September 8-10 1993, pp. 127–132.

[10] W.L. Soong and T.J.E. Miller, "Field-weakening performance of brushless synchronous ac motor drives," *IEE Proc.-Electr.Power Appl.*, vol. 141, no. 6, pp. 331–340, November 1994.

[11] S.R. Macminn and T.M. Jahns, "Control techniques for improved high-speed performance of interior pm synchronous motor drives," *IEEE Transactions on Industry Applications*, vol. 27, no. 5, pp. 997–1004, September 1986.

[12] S. Morimoto, Y. Takeda, and T. Hirasa, "Current phase control methods for permanent magnet synchronous motors," *IEEE Transactions on Power Electronics*, vol. 5, no. 2, pp. 133–139, April 1990.

[13] S. Morimoto, M. Sanada, and Y. Takeda, "Effects and compensation of magnetic saturation in flux-wweakening controlled permanent magnet synchronous motor drives," *IEEE Transactions on Industry Applications*, vol. 30, no. 6, pp. 1632–1637, November 1994.

[14] J.Svensson, *Grid Connected Voltage Source Converter – Control Principles and Wind Energy Applications*, Ph.D. thesis, School of Electrical and Computer Engineering, Chalmers University of Technology, Göteborg, Sweden, 1998, Technical Report No.331.

[15] M. Lindgren, *Modeling and Control of Voltage Source Converters Connected to the Grid*, Ph.D. thesis, School of Electrical and Computer Engineering, Chalmers University of Technology, Göteborg, Sweden, 1998, Technical Report No.351.

[16] J. Lindström, J. Luomi, and J. Hellsing, "Permanent-magnet motor for a hybrid electric vehicle," in *NORPIE/98, IEEE Nordic Workshop on Power and Industrial Electronics Proceedings*, Espoo, Finland, August 26-27 1998, pp. 200–205.

[17] IEC Publication 34-2A, "Methods for determining losses and efficiency of rotating electric machinery from tests (excluding machines for traction vehicles), measurement of losses by the calorimetric method," Tech. Rep., 1974.

[18] A. Arkkio, "Finite element analysis of cage induction motors fed by static frequency converters," *IEEE Transactions on Magnetics*, vol. 26, no. 2, pp. 551–554, March 1990.

[19] A. Arkkio and A. Niemenmaa, "Estimation of losses in cage induction motors using finite element techniques," in *Proceedings of the International Conference on Electrical Machines*, Manchester, U.K, September 15-17 1992, vol. 2, pp. 317–321.

[20] P. Vas, K.-E. Hallenius, and J.E. Brown, "Cross-saturation in smooth-air-gap electrical machines (ac machines)," *IEEE Transactions on Energy Conversion*, vol. 1, no. 1, pp. 103–112, March 1986.

A Current Minimization

An expression for maximum torque per ampere in the constant torque region is obtained by using the armature current vector, $\underline{i}_a$, shown in Fig. 26. The d-axis and q-axis current components can be expressed as

$$i_d = i_a \sin(\gamma) \tag{13}$$

and

$$i_q = i_a \cos(\gamma) \tag{14}$$

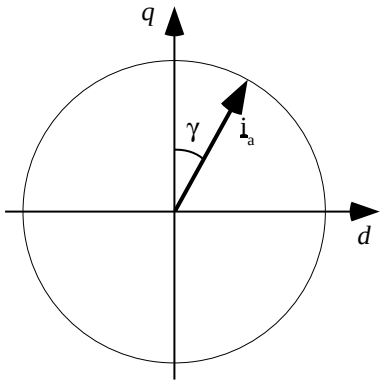

Figure 26: The armature current vector

where i_a is the magnitude of the current vector $\underline{i}_a$. An approach to the minimization of the current, i_a, is achieved by finding the maximum torque for a fixed current magnitude. The problem is to identify the position of the current vector that yields the optimum relation between i_d and i_q. The electrodynamic torque is

$$T_e = \frac{3}{2} p i_a \left(\psi_m cos(\gamma) + (L_d - L_q) \frac{1}{2} \sin(2\gamma) \right) \tag{15}$$

and the derivative of the torque with respect to the position is

$$\frac{\partial T_e}{\partial \gamma} = \frac{3}{2} p i_a \left(-\psi_m sin(\gamma) + \Big(L_q - L_d \Big) \Big(1 - 2\sin^2(\gamma) \Big) \right) \tag{16}$$

Solving for the torque maximum, given a specified current and substitution of Equations (13) and (14), gives the relation between the d -axis and q-axis currents for the minimum armature current magnitude

$$i_d = \frac{\psi_m}{2(L_d - L_q)} \pm \sqrt{\frac{\psi_m^2}{4(L_d - L_q)} - i_q^2} \tag{17}$$

B Current control

A general PI-controller

The general expression for the output from an analogue PI-controller is

$$c(t) = K_p \left(\epsilon(t) + \frac{1}{T_i} \int_0^t \epsilon(\tau) d\tau \right) \tag{18}$$

Where $c(t)$ is the output signal from the PI-controller and $\epsilon(t)$ is the input control error. In a sampled system with a constant sample interval, h, the output from the PI-controller can be written as

$$c(k) = K_p \left(\epsilon(k) + \frac{1}{T_i} \sum_{n=0}^{k} \epsilon(n) h \right) \tag{19}$$

An alternative approach is to differentiate the integral part, I, in Equation (18), using a difference approximation for the time-derivative

$$\frac{I(k) - I(k-1)}{h} = \frac{K_p}{T_i} \epsilon(k) \tag{20}$$

which can be rearranged to

$$I(k) = \frac{K_p}{T_i} \epsilon(k) h + I(k-1) \tag{21}$$

The dead-beat gain P-controller

A dead-beat current controller for the PMSM is derived from the voltage equations in the dq-reference frame

$$u_d = R_s i_d + L_d \frac{di_d}{dt} - \omega L_q i_q \tag{22}$$

and

$$u_q = R_s i_q + L_q \frac{di_q}{dt} + \omega L_q i_q + \omega \Psi_m \tag{23}$$

The voltage-time area between samples k and $k+1$ is derived from integration of Equations (22) and (23)

$$\begin{aligned}\int_{kh}^{(k+1)h} u_d dt = &\int_{kh}^{(k+1)h} R_s i_d dt + \int_{i_d(kh)}^{i_d((k+1)h)} L_d di_d - \\ &- \int_{kh}^{(k+1)h} \omega L_q i_q dt\end{aligned} \tag{24}$$

$$\begin{aligned}\int_{kh}^{(k+1)h} u_q dt = &\int_{kh}^{(k+1)h} R_s i_q dt + \int_{i_q(kh)}^{i_q((k+1)h)} L_q di_q + \\ &+ \int_{kh}^{(k+1)h} \omega L_d i_d dt + \int_{kh}^{(k+1)h} \omega \psi_m dt\end{aligned} \tag{25}$$

The left-hand sides in Equations (24) and (25) are the voltage-time areas between samples k and $k+1$. Rewriting yields

$$\begin{aligned}y_d(k,k+1) = &hR_s\bar{i_d}(k,k+1) + L_d\Big(i_d(k+1) - i_d(k)\Big) - \\ &- L_q h\bar{\omega}(k,k+1)\bar{i_q}(k,k+1)\end{aligned} \tag{26}$$

$$\begin{aligned}y_q(k,k+1) = &hR_s\bar{i_q}(k,k+1) + L_q\Big(i_q(k+1) - i_q(k)\Big) + \\ &+ L_d h\bar{\omega}(k,k+1)\bar{i_d}(k,k+1) + h\bar{\omega}(k,k+1)\psi_m\end{aligned} \tag{27}$$

where $\bar{i}(k,k+1)$ and $\bar{\omega}(k,k+1)$ denotes the average current and rotor angular frequency between samples k and $k+1$, respectively. The left-hand sides in Equations (26) and (27) are the desired voltage-time areas in the d-direction and q-direction at sample k. If the average current is approximated by

$$\bar{i}(k,k+1) = \frac{i(k+1) + i(k)}{2} \tag{28}$$

and if the rotor angular frequency is assumed to be constant in the sample interval $(k,k+1)$, the equations can be simplified to

$$\begin{aligned}y_d^*(k) = &h\frac{R_s}{2}\Big(i_d(k+1) + i_d(k)\Big) + L_d\Big(i_d(k+1) - i_d(k)\Big) - \\ &- h\frac{L_q}{2}\omega(k)\Big(i_q(k+1) + i_q(k)\Big)\end{aligned} \tag{29}$$

$$y_q^*(k) = h\frac{R_s}{2}\Big(i_q(k+1) + i_q(k)\Big) + L_q\Big(i_q(k+1) - i_q(k)\Big) + \\ + h\frac{L_d}{2}\omega(k)\Big(i_d(k+1) + i_d(k)\Big) + h\omega(k)\psi_m \tag{30}$$

Dead-beat response of the current is achieved if the desired current at sample k is achieved one sample later, that is $i(k+1) = i(k)^*$, which is inserted into Equations (29) and (30). Division by h gives the expression for the desired voltage reference values at sample k for a current P-controller with dead-beat gain and feed-forward compensation in the sampled system.

$$u_d^*(k) = \left(\frac{R_s}{2} + \frac{L_d}{h}\right)\left(i_d^*(k) - i_d(k)\right) + R_s i_d(k) - \\ - \frac{L_q}{2}\omega(k)\Big(i_q^*(k) + i_q(k)\Big) \tag{31}$$

$$u_q^*(k) = \left(\frac{R_s}{2} + \frac{L_q}{h}\right)\left(i_q^*(k) - i_q(k)\right) + R_s i_q(k) + \\ + \frac{L_q}{2}\omega(k)\Big(i_d^*(k) + i_d(k)\Big) + \omega(k)\psi_m \tag{32}$$

The dead-beat gains in the d- and q-directions are, thus

$$K_{pd} = \frac{R_s}{2} + \frac{L_d}{h} \tag{33}$$

$$K_{pq} = \frac{R_s}{2} + \frac{L_q}{h} \tag{34}$$

C Loss Measurement

The Calorimetric Method

The power dissipated to a cooling medium flowing at a volumetric flow rate q_v is described by

$$P_d = \rho(\theta) c_p(\theta) q_v \Delta\theta \tag{35}$$

where $\rho(\theta)$ is the density of the coolant, $c_p(\theta)$ is the specific heat capacity of the coolant at temperature θ, and $\Delta\theta = \theta_{out} - \theta_{in}$ is the temperature rise of the coolant.

If the temperature rise is small, a good approximation of the coolant properties is to assign the density and specific heat capacity at the average temperature, $\overline{\theta}$, between the inlet and the outlet. The maximum relative error in the measurement of losses dissipated to the coolant according to Equation (35) is described by

$$\left|\frac{\Delta P_d}{P_d}\right| \leq \left|\frac{\Delta\rho(\overline{\theta})}{\rho(\overline{\theta})}\right| + \left|\frac{\Delta c_p(\overline{\theta})}{c_p(\overline{\theta})}\right| + \left|\frac{\Delta q_v}{q_v}\right| + \left|\frac{\Delta(\Delta\theta)}{\Delta\theta}\right| \tag{36}$$

An estimation of the accuracy of the loss measurement was made by including the heat leakage, P_l, and evaluate the sum of the internal motor losses, P_i, as described by

$$P_i = P_d + P_l \tag{37}$$

The maximum absolute error of the internal losses is

$$\left|\Delta P_i\right| \leq \left|\Delta P_d\right| + \left|\Delta P_l\right| \tag{38}$$

The maximum relative error in the estimate of the total losses is, thus, described by

$$\left|\frac{\Delta P_i}{P_i}\right| \leq \frac{\left|\Delta P_d\right| + \left|\Delta P_l\right|}{\left|P_d + P_l\right|} \tag{39}$$

The Input-Output Method

The traditional method of obtaining the total losses of a system, like an electrical machine, is based on measurements of the input power and the output power. Despite the potential to measure accurately with modern, highly sofisticated equipment, the outcome can be insufficient.

There is an inherent problem with applying the input-output method to a test object with a high efficiency which can be enlightened by a study of the expression for the total losses

$$P_{tl} = P_{in} - P_{out} \tag{40}$$

where P_{in} is the input power, P_{out} is the output power and P_{tl} is the total losses. By introducing the system efficiency, η, Equation (40) can be written as

$$P_{tl} = \frac{P_{out}}{\eta} - P_{in}\eta \tag{41}$$

Since η is less than 1, the maximum relative error of the total losses, according to Equation (41), can be written as

$$\left|\frac{\Delta P_{tl}}{P_{tl}}\right| < \frac{1}{1-\eta}\left(\left|\frac{\Delta P_{out}}{P_{out}}\right| + \left|\frac{\Delta P_{in}}{P_{in}}\right|\right) \tag{42}$$

Consequently, with an assumed relative error of 1% in both the input power and output power measurements and a system efficiency of 95 %, the relative error of the loss measurement is 40 %, which should be compared with the accuracy achieved with the calorimetric method.